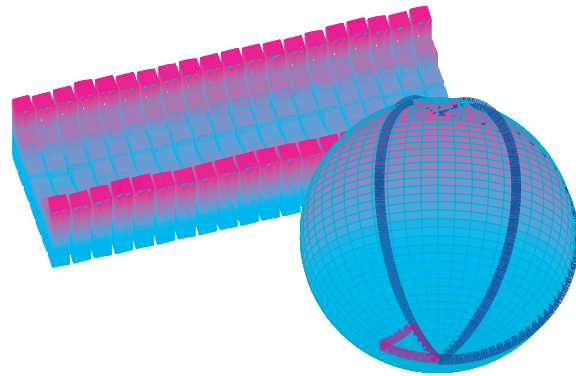

Neutral Atom Quantum Computing with Rydberg Blockade



Line Hjortshøj Pedersen

Lundbeck Foundation Theoretical Center for Quantum System Research
Department of Physics and Astronomy
University of Aarhus
Denmark

PhD Thesis
July 2008

This thesis is submitted to the Faculty of Science at the University of Aarhus, Denmark, in order to fulfill the requirements for obtaining the PhD degree in Physics. The studies have been carried out under the supervision of Professor Klaus Mølmer in the Lundbeck Foundation Theoretical Center for Quantum System Research at the Department of Physics and Astronomy.

Contents

Preface	v
List of publications	vii
1 Introduction	1
1.1 Introduction to quantum computation	1
1.2 Outline	5
2 Fidelity of quantum operations	7
2.1 The average fidelity measure	8
2.2 The fidelity distribution	15
2.3 Summary	22
3 Introduction to neutral atom quantum computing	25
3.1 The qubit basis states	26
3.2 Initialization	26
3.3 Read out	27
3.4 Single-qubit gates	28
3.5 Two-qubit gates	38
3.6 Experimental progress	46
4 Decoherence-free subspaces	51
4.1 Information storage in a DFS	51
4.2 Information processing in the DFS	52
4.3 Assessment of the DFS gates	57
4.4 Summary	63
5 Error correction in ensemble registers	65
5.1 Ensemble register encoding	66
5.2 Error correction for collectively encoded qubits	71
5.3 Summary	77
6 Few qubit atom-light interfaces with collective encoding	79
6.1 Superradiance	79

6.2	Directionality of single-photon emission	80
6.3	Time dependence of single-photon emission	81
6.4	Single-photon emission from a mesoscopic sample	85
6.5	Atom-light interfaces for scalable quantum networks	90
6.6	Summary	93
7	Summary and outlook	95
7.1	Dansk resumé	96
	Appendices	97
A	Evolution of the lambda system	99
B	The corrected Rabi frequency	103
C	The Green's function perturbation method	105
D	Quantum Monte Carlo approach	109
	Bibliography	111

Preface

This thesis presents the research I have done during my PhD studies at the Department of Physics and Astronomy, University of Aarhus. The research was carried out during the period August 1st 2004 - July 31st 2008 under the supervision of Professor Klaus Mølmer in the Lundbeck Foundation Theoretical Center for Quantum System Research (LTC).

Acknowledgments

First of all, I would like to thank my supervisor Klaus Mølmer. It has been a true privilege to work under the guidance of a supervisor who is always willing to share his extensive enthusiasm for and insight into his field.

Secondly, I have been privileged to enjoy a close collaboration with Etienne Brion during his time as a post doc at the LTC.

I would also like to acknowledge Niels Martin Møller for his collaboration and numerous mathematical discussions throughout the years.

In addition, I would like to thank the group of Mark Saffman and Thad G. Walker at the University of Wisconsin, USA, for their close collaboration.

For their hospitality during my visit in the first half year of 2007, I would like to thank the group of Chitra Rangan and the graduate students at the Department of Physics at the University of Windsor, Canada.

For proofreading this thesis, I would like to acknowledge Katharine Challis, Nicolai G. Nygaard, Ditte Møller, and Anders S. Mouritzen.

Finally, my warmest thanks goes to my friends and colleagues at the University of Aarhus for making the eight years I have spent here thoroughly enjoyable. Additionally, I am grateful to my family for their love and support.

Line Hjortshøj Pedersen
July, 2008

List of publications

- I. **Line Hjortshøj Pedersen**, Niels Martin Møller and Klaus Mølmer.
Fidelity of quantum operations.
Phys. Lett. A **367**, 47 (2007).
- II. Etienne Brion, **Line Hjortshøj Pedersen** and Klaus Mølmer.
Adiabatic elimination in a lambda system.
J. Phys. A **40**, 1033 (2007).
- III. Etienne Brion, **Line Hjortshøj Pedersen** and Klaus Mølmer.
Implementing a neutral atom Rydberg blockade gate without populating the Rydberg state.
J. Phys. B **40**, S159 (2007).
- IV. Etienne Brion, **Line Hjortshøj Pedersen**, Klaus Mølmer, Sucismita Chutia and Mark Saffman.
Universal quantum computation in a neutral-atom decoherence-free subspace.
Phys. Rev. A **75**, 032328 (2007).
- V. Etienne Brion, **Line Hjortshøj Pedersen**, Mark Saffman and Klaus Mølmer.
Error correction in ensemble registers for quantum repeaters and quantum computers.
Phys. Rev. Lett. **100**, 110506 (2008).
- VI. **Line Hjortshøj Pedersen** and Chitra Rangan.
Controllability and universal three-qubit quantum computation with trapped-electron states.
Quant. Inf. Proc. **7**, 33 (2008).
- VII. **Line Hjortshøj Pedersen**, Niels Martin Møller and Klaus Mølmer.
The distribution of quantum fidelities.
arXiv:0807.4843 (2008). Accepted for publication in Phys. Lett. A.
- VIII. **Line Hjortshøj Pedersen** and Klaus Mølmer.
Few qubit atom-light interfaces with collective encoding.
arXiv:0807.3610 (2008).

CHAPTER 1

Introduction

Since the sixties, the power of computers has increased dramatically thanks to a continuous miniaturization of electronic components. However, this progression cannot last for ever. Indeed, we approach the limit where the classical rules which govern our macroscopic world and our classical computers must be replaced by quantum laws. New computers, based on these fundamental laws, are thus bound to arise.

In the 1980's the first ideas emerged for exploiting the computational capabilities of quantum systems [1,2]. Subsequently, the discovery of quantum algorithms outperforming their classical counterparts [3,4] spurred great interest in the field of quantum computation. With techniques for quantum error correction [5,6] and the identification of various physical systems suitable for quantum computation, the practical realization of a quantum computer primarily seems to be a matter of time.

In this chapter, we briefly introduce the key concepts of quantum computation. For comprehensive reviews of the field, we refer the reader to [7,8]. Based on our introduction, we outline the contents of the thesis.

1.1 Introduction to quantum computation

1.1.1 Qubits

In a classical computer a *binary digit* is represented by the *bit*, the fundamental unit of information, which either takes the value 0 or 1.

The quantum analogue of a classical bit, the quantum bit or *qubit*, is a two-level system. In contrast to its classical counterpart, due to the laws of quantum mechanics, a qubit can exist in superposition states, such as $|\psi\rangle = c_0 |0\rangle + c_1 |1\rangle$, where the coefficients are complex numbers obeying the normalization condition $|c_0|^2 + |c_1|^2 = 1$. With access to N qubits, a quantum register can be prepared in a superposition of 2^N basis states, which can be processed in parallel by a quantum computer. Referred to as quantum

parallelism, this offers a dramatic increase in computational power.

1.1.2 Quantum gates

Quantum gates are linear, unitary transformations acting on a set of qubits. In the same way as a classical computer, algorithms for a quantum computer can be constructed from gates acting on either one or two qubits. In particular, it can be shown that a set of gates exists such that any unitary operation can be approximated to arbitrary accuracy solely by combining elements from this set. Such a set is called universal and could for instance consist of a single-qubit Hadamard gate (H), a single-qubit $\pi/8$ gate (T) and a two-qubit controlled-NOT gate (CNOT) [7]. In the basis $\{|0\rangle, |1\rangle\}$ the single-qubit gates read:

$$H = \frac{1}{\sqrt{2}} \begin{pmatrix} 1 & 1 \\ 1 & -1 \end{pmatrix}, \quad T = \begin{pmatrix} 1 & 0 \\ 0 & e^{i\pi/4} \end{pmatrix},$$

whereas the two-qubit gate is written in the basis $\{|00\rangle, |01\rangle, |10\rangle, |11\rangle\}$:

$$\text{CNOT} = \begin{pmatrix} 1 & 0 & 0 & 0 \\ 0 & 1 & 0 & 0 \\ 0 & 0 & 0 & 1 \\ 0 & 0 & 1 & 0 \end{pmatrix}.$$

1.1.3 Quantum algorithms

Contrary to the classical case, performing a measurement is problematic in quantum mechanics, as it leads to the collapse of the state of the system and hence a loss of information. Thus, measuring the state of a qubit collapses the state onto either $|0\rangle$ or $|1\rangle$ with probability $|c_0|^2$ and $|c_1|^2$, respectively. Accordingly, the coefficients c_0, c_1 cannot be determined. Yet, by designing algorithms in a very clever way, a measurement on the final state will output the desired outcome with a high probability.

Currently, there exist three quantum algorithms that outperform any known classical algorithm: Grover's search algorithm allows one to find a particular element in an unsorted database with a quadratic increase in speed [3]. Even more impressive is Shor's factoring algorithm, which provides an exponential speedup compared to the best classical algorithms [4]. Finally, the Deutsch-Jozsa algorithm renders it possible to determine in a single function call whether a binary function is constant (e.g., always outputs 0) or balanced (half the function values are 0, the other half 1) [9].

1.1.4 The physical implementation of a quantum computer

As of yet, the road to the experimental realization of a large scale quantum computer is still filled with obstacles. A great hurdle is the phenomenon

of decoherence, which arises from the interaction of a qubit with its environment. Thus, if the physical system implementing our qubits is not well isolated, the environment will, so to say, continually “measure” the state of the system. Since quantum computation relies on the undisturbed evolution of quantum coherences, decoherence poses a major problem.

Encoding qubits in a system which is efficiently isolated from the environment, by way of example photons, limits the problem of decoherence. However, if qubits only interact weakly with their surroundings, it is difficult to obtain the strong coupling between qubits necessary for two-qubit gates. Accordingly, it is a tradeoff between achieving a strong interaction between qubits and a weak coupling to the environment.

Besides choosing a well isolated system, decoherence can be circumvented by redundantly encoding a single logical qubit in several physical qubits. This allows for quantum error correction [5,6], the existence of which ensures that quantum noise does not pose a fundamental barrier to the practical realization of a quantum computer. Thus, the threshold theorem states that *provided the noise in individual quantum gates is below a certain constant threshold it is possible to efficiently perform an arbitrarily large quantum computation* [7]. Hence, if gate error rates are below a certain threshold, errors can be corrected faster than they occur. The value of this threshold depends on the quantum computing system in question.

At present there is no consensus about which physical system is best suited for building a large scale quantum computer, although various proposals for the experimental implementation of a quantum computer have been put forward in very different fields such as those of cold trapped ions [10] or atoms [11,12], NMR [13,14], linear optics [15], quantum dots [16], and super conducting devices [17]. A comparison of the approaches is facilitated by the so-called DiVincenzo criteria, which is a set of minimum requirements any quantum computing proposal must fulfill [18]:

1. The quantum computer must be a scalable physical system with well characterized qubits.
2. It must be possible to initialize the system to a given known quantum state.
3. The qubit coherence time must be longer than the gate operation time.
4. It must be possible to implement a universal set of quantum gates.
5. It must be possible to read out the results of the computation.

In addition to examples of qubit identification and mechanisms for coupling qubits, Fig. 1.1 provides an assessment of the ability to meet the DiVincenzo criteria for some of the most successful physical implementations of

	Qubit	Coupling	DiVincenzo criteria				
			Scalable physical system	Initialization	Long coherence time	Universal set of gates	Read out
Trapped ions	Electronic or hyperfine states	Collective vibrational mode		✓	✓	✓	✓
Neutral atoms	Hyperfine states	Dipole-dipole interaction		✓	✓		
NMR	Nuclear spins of atoms in a molecule	Chemical bonds			✓	✓	
Linear optics	Polarization of a single photon	Beam splitters and measurements			✓		
Quantum dots	Electron or nuclear spin	Spin-spin coupling		✓			✓
Super conducting	Quantized flux or charge	Currents and/or magnetic fields		✓			✓

 Demonstrated experimentally
  Theory proposals available
  No proposals available

Figure 1.1. The current status of the central physical implementations of a quantum computer.

quantum computation. For a more detailed discussion of the various proposals, we refer the reader to the quantum computation roadmap [19].

1.1.5 Quantum networks

The implementation of a quantum computer solely relies on the compliance of the above requirements. However, for the achievement of distributed quantum computation and long distance quantum communication, DiVincenzo has put forward two additional requirements [18]:

6. It must be possible to interconvert stationary and flying qubits.
7. It must be possible to faithfully transmit flying qubits between specified locations.

Thus, to transmit quantum information from one location to another, it must be encoded in qubits which can move. Such qubits, termed ‘flying’, may be encoded in (the polarization or the spatial wave function of) photons. In order to store the information safely, the states of the flying qubits must be transferred to ‘stationary’ qubits, for instance atomic ensembles.

Fulfillment of the above two criteria opens up the possibility of distributed quantum computation. A quantum network can be established by (optically) connecting several quantum registers, thus allowing for scalable quantum computation in a hybrid approach.

However, transmitting quantum information, for instance in the form of photons, over noisy quantum channels is a very difficult task due to an exponential decrease in signal quality and communication rate with the distance.

In principle, the use of redundant encoding (for error correcting codes) suffices for protecting information against noise. Unfortunately, the requirements for quantum error correction on measurements, local operations and channel noise are difficult to meet.

An alternative approach is the exchange of information by quantum teleportation. Transferring the state of a qubit to another by means of teleportation is feasible, if entanglement between the two endpoints of the communication channel can be established. So-called quantum repeater protocols [20,21] are designed to perform the latter task.

The basic idea of a quantum repeater is to divide the communication channel into smaller segments and by connecting entangled short-distance pairs, establishing entanglement between the endpoints of the channel. Because of imperfect operations, the fidelity decreases in each connection step. Fortunately, entanglement purification protocols exist to circumvent this limitation by producing a high fidelity entangled state from a collection of low fidelity states. To this end, a quantum memory capable of storing information safely is required.

For a recent review of quantum networks, we refer the reader to [22].

1.2 Outline

In this thesis, we study a specific physical implementation of quantum computation, namely a quantum computer based on neutral atoms. Neutral atom quantum computing (NAQC) benefits from the fact that qubits couple only weakly to the environment in that the atoms are uncharged. In addition, techniques for cooling and trapping atoms are well developed. Consequently, NAQC allows for high levels of coherence and control.

There are several ways to construct a quantum computer based on neutral atoms. In this thesis we consider only one of these, namely neutral atom quantum computing with Rydberg blockade. The central idea of this proposal is to couple qubits, encoded in the ground hyperfine states, by an electric-dipole interaction via conditional excitation to a Rydberg state [23]. This scheme provides for fast gates which are potentially insensitive to motional heating. A collective version of the gate has been proposed in [24].

Before embarking on our research on various aspects of NAQC with Rydberg blockade, we present our work on the fidelity of quantum operations in **chapter 2**.

In **chapter 3** we introduce NAQC with Rydberg blockade. When relevant, we take as our starting point the proposal of Saffman and Walker [25]. This setting holds promise for coherence times of order seconds and gate operation times of order microseconds.

As discussed previously, quantum information can be protected from decoherence effects by making use of quantum error correction schemes. An alternative approach consists in encoding information in subspaces which

are immune to errors. In **chapter 4** we identify such a decoherence-free subspace and construct gates which allow the system to remain in this subspace during gate operations.

In **chapter 5** we turn to the issue of scalability. We show that by encoding information in the collective population of different internal states rather than storing individual qubits in individual atoms, the requirement of individual addressing can be circumvented. Since standard error correction techniques do not apply to this encoding scheme, we devise a method for efficient error identification and correction in these registers.

In **chapter 6**, for the purpose of constructing efficient atom-light interfaces for quantum networks, we propose to build few-qubit quantum registers based on the collective encoding scheme in small atomic ensembles.

Finally, in **chapter 7**, we summarize the main ideas and results of the thesis.

Fidelity of quantum operations

In quantum information theory one requires a measure of the fidelity of quantum operations, such as quantum computing gates, quantum state storage and retrieval, transmission, and teleportation. The fidelity characterizes the agreement between the actual and desired outcomes of an operation, and in general it depends on the initial state on which the operation is applied. Since the operation may be applied to any arbitrary state, it is natural to average the fidelity over all pure initial states, chosen uniformly throughout the system Hilbert space. Derivations have been given in the literature for the average fidelity of qubit [26] and qudit operations [27], as well as for their evaluation as a sum over a properly chosen discrete set of states [28,29]. The latter approach is particularly relevant in connection with quantum process tomography [7], which provides a procedure for determining the quantum operation acting on a system from experimental observations.

In this chapter, we first present and analyze a simple expression for the average fidelity in the case where the quantum operation is known, e.g., from a solution of the Schrödinger or master equation of the system. We focus on the calculation of the fidelity with which the known actual operation resembles the desired operation on the quantum system. This part of the chapter, namely chapter 2.1, is based on our paper [I].

In chapter 2.2, based on our paper [VII], we expand our knowledge of the fidelity of a given operation by studying the distribution of the single-state fidelity. In particular, we derive an explicit formula for the variance of the fidelity distribution for unitary operators and unitary operators projected onto smaller quantum systems. Furthermore, we find an explicit expression for the fidelity distribution in the case of a two by two unitarily diagonalizable matrix.

2.1 The average fidelity measure

To obtain an explicit formula for the average fidelity of a quantum operation on a finite-dimensional quantum system, we first present a relation for uniformly averaged matrix elements of a general linear operator. Subsequently, we derive corollaries that yield the fidelity of quantum operations in a number of different cases.

Theorem 1. *For any linear operator M acting on an n -dimensional complex Hilbert space, the uniform average of $|\langle\psi|M|\psi\rangle|^2$ over state vectors $|\psi\rangle$ on the unit sphere S^{2n-1} in \mathbb{C}^n is given by*

$$\begin{aligned} & \int_{S^{2n-1}} |\langle\psi|M|\psi\rangle|^2 dV && (L) \\ & = \frac{1}{n(n+1)} [\text{Tr}(MM^\dagger) + |\text{Tr}(M)|^2], && (R) \end{aligned} \quad (2.1)$$

where dV is the normalized measure on the sphere.

Proof. Recent detailed proofs of this theorem are given in [30,31], and it is also readily verified using a recent result for the averages of general polynomials of state vector amplitudes over the unit sphere [32]. Since both of these proofs draw on elaborate mathematical results, we present an alternative, more straightforward derivation.

We first show that (2.1) is valid if M is Hermitian. A Hermitian matrix M can be diagonalized such that $UMU^{-1} = \Lambda$, where Λ is a diagonal matrix with elements $\lambda_1, \dots, \lambda_n \in \mathbb{R}$ and $U \in U(n)$. Note that the left- and right-hand sides of (2.1), denoted by L and R , obey the conjugation invariance: $L(UMU^{-1}) = L(M)$, $R(UMU^{-1}) = R(M)$ for any $U \in U(n)$. This follows for the left-hand side L by a change of variables $\psi \mapsto U\psi$, and for R it is simply a property of the trace. Thus, it suffices to show that $L = R$ for a real, diagonal matrix Λ .

The left-hand side $L(\Lambda)$ is a homogeneous polynomial of degree two in the real variables $\lambda_1, \dots, \lambda_n$. Unitary invariance implies that $L(\Lambda)$ is invariant under the exchange¹ of any two λ_i and λ_j , which is only possible if L is of the form:

$$L = a\text{Tr}(\Lambda^2) + b\text{Tr}(\Lambda)^2, \quad (2.2)$$

where a and b are constants that may depend on n . We find that $a = b = 1/n(n+1)$ from the two equations obtained by inserting two convenient matrices into (2.2) and the left-hand side of (2.1). Thus, insertion of the identity matrix yields the equation

$$a \cdot n + b \cdot n^2 = 1$$

¹This is easily seen by choosing the unitary matrix such that it swaps the relevant rows in Λ .

and insertion of the matrix for which the only non-zero element is $\Lambda_{1,1}$ implies that

$$a + b = \int_{S^{2n-1}} |c_0|^4 dV = \frac{2}{n(n+1)},$$

where $|\psi\rangle = \sum c_j |j\rangle$ and the last equality follows by evaluation of the integral². Thus, we have shown that $L(\Lambda) = R(\Lambda)$ and Theorem 1 applies for any Hermitian matrix M .

We also have that $L(A) = R(A)$, where A denotes an anti-Hermitian matrix (i.e., $A^\dagger = -A$), cf. that

$$L(A) = L(iA) = R(iA) = R(A).$$

The general matrix $M = (M + M^\dagger)/2 + (M - M^\dagger)/2 = S + A$ is decomposed as a sum of a Hermitian and an anti-Hermitian matrix, respectively, and the explicit results

$$\begin{aligned} L(S + A) &= \int_{S^{2n-1}} |\langle \psi | S | \psi \rangle + \langle \psi | A | \psi \rangle|^2 dV \\ &= \int_{S^{2n-1}} |\langle \psi | S | \psi \rangle|^2 + |\langle \psi | A | \psi \rangle|^2 + \\ &\quad \langle \psi | S | \psi \rangle \cdot \underbrace{(\langle \psi | A^\dagger | \psi \rangle + \langle \psi | A | \psi \rangle)}_0 dV \\ &= L(S) + L(A) \end{aligned}$$

and

$$\begin{aligned} R(S + A) &= \frac{1}{n(n+1)} \{ \text{Tr}((S + A)(S - A)) + \\ &\quad (\text{Tr}(S) + \text{Tr}(A))(\text{Tr}(S) - \text{Tr}(A)) \} \\ &= R(S) + R(A) \end{aligned}$$

prove the theorem. \square

The first application of the theorem has been in noise estimation and quantum process tomography [33]. Here, we apply Theorem 1 to compute the average fidelity explicitly in certain cases where the actual operation is known and fully characterized.

²The integral is evaluated by a proper parametrization of the c_j 's, e.g., $c_0 = x_1 + ix_2, \dots$, and $c_{n-1} = x_{2n-1} + ix_{2n}$, where $x(\theta_1, \dots, \theta_{2n-1}) = [\sin \theta_1 \cdots \sin \theta_{2n-2} \cos \theta_{2n-1}, \sin \theta_1 \cdots \sin \theta_{2n-2} \sin \theta_{2n-1}, \sin \theta_1 \cdots \sin \theta_{2n-3} \cos \theta_{2n-2}, \sin \theta_1 \cdots \sin \theta_{2n-4} \cos \theta_{2n-3}, \dots, \cos \theta_1], \theta_1, \dots, \theta_{2n-2} \in [0, \pi],$ and $\theta_{2n-1} \in [0, 2\pi]$. Note that the square root of the Jacobian determinant equals $\sin^{2n-2} \theta_1 \sin^{2n-3} \theta_2 \cdots \sin \theta_{2n-2}$.

2.1.1 Average fidelity of a unitary transformation

We first calculate the average fidelity of a process where our, possibly controllable, physical interactions yield a unitary evolution U , whereas we intend to perform the unitary operation U_0 on the system. For transmission, storage, and retrieval, U_0 is the identity, and for quantum computing U_0 is the desired quantum gate.

According to Theorem 1, the squared overlap between the actual outcome $U|\psi\rangle$ and the desired final state $U_0|\psi\rangle$ averages to

$$\begin{aligned} F &= \int_{S^{2n-1}} |\langle \psi | M | \psi \rangle|^2 dV \\ &= \frac{1}{n(n+1)} [\text{Tr}(MM^\dagger) + |\text{Tr}(M)|^2], \end{aligned} \quad (2.3)$$

with $M = U_0^\dagger U$. Since M is unitary, $\text{Tr}(MM^\dagger) = n$. If M multiplies all states by a single phase factor, $|\text{Tr}(M)|^2 = n^2$ and the fidelity is unity. A general unitary matrix has eigenvalues of the form $\exp(i\phi_j)$, and $|\text{Tr}(M)| < n$ if these phases differ.

It is easily demonstrated that, as stated in [28], for qubits, (2.3) corresponds to a simple average over any six pure states forming a regular octahedron on the Bloch sphere. In particular, the six axial pure states $|0\rangle, |1\rangle, (|0\rangle + |1\rangle)/\sqrt{2}, (|0\rangle - |1\rangle)/\sqrt{2}, (|0\rangle + i|1\rangle)/\sqrt{2},$ and $(|0\rangle - i|1\rangle)/\sqrt{2}$. The minimum set of states is any four pure states forming a regular tetrahedron on the Bloch sphere, for instance the states $|1\rangle, \sqrt{2/3}|0\rangle + e^{-i\pi/2}\sqrt{1/3}|1\rangle, \sqrt{2/3}|0\rangle + e^{i\pi/6}\sqrt{1/3}|1\rangle,$ and $\sqrt{2/3}|0\rangle + e^{i5\pi/6}\sqrt{1/3}|1\rangle$. In the general case of a qudit, the minimum set is given by any set of states fulfilling $|\langle \psi_i | \psi_j \rangle|^2 = 1/(n+1)$ for $i \neq j$ [29].

2.1.2 Subspace averaged fidelity of a unitary transformation

In a number of quantum information scenarios, auxiliary quantum levels are used to mediate the desired operations. For example, qubits may be encoded in ground state atomic levels coupled by Raman transitions via optically excited states. Two-qubit interactions may involve state-selective excitation to states with large dipole moments and strong long-range interaction, as will be discussed in chapter 3.5. In these protocols, the auxiliary levels of the quantum system are unpopulated before the process, and, ideally, they are also unpopulated after the process. But, if the fidelity is evaluated by identifying $M = U_0^\dagger U$ on the complete system Hilbert space, as described above, this may give far too pessimistic results.

Consider, for example, an atomic qubit which is, with certainty, initially and finally in the ground hyperfine states, and no population has leaked to the excited atomic states during the Raman process. If the average in (2.3) is made over the full system Hilbert space, phases acquired by amplitudes on

the excited states cause a reduction in the fidelity, even if the final state is the correct one for all input qubit states. Consequently, we should only average the fidelity over the relevant input states. Since the final state, ideally, is also in the qubit subspace, we consider the matrix $(PU_0^\dagger P)(PUP)$, where P is the projection operator on the relevant, quantum information carrying subspace S and U_0 represents the desired unitary evolution of the relevant subspace. In matrix notation, we thus address the square $n_{rel} \times n_{rel}$ submatrix of the full matrix M , and employ Theorem 1 for this matrix:

$$\begin{aligned}
F &= \int_{S^{2n-1}} |\langle \psi | PU_0^\dagger PUP | \psi \rangle|^2 dV \\
&= \int_{S^{2n_{rel}-1}} |\langle \psi | M_{rel} | \psi \rangle|^2 dV \\
&= \frac{1}{n_{rel}(n_{rel} + 1)} [\text{Tr}(M_{rel} M_{rel}^\dagger) + |\text{Tr}(M_{rel})|^2],
\end{aligned} \tag{2.4}$$

where $M_{rel} = U_0^\dagger PUP$. Note that if population leaks to the auxiliary levels, M_{rel} is not unitary, and hence both terms of (2.4) have nontrivial values.

If a measurement assures that the final state does not populate the complement to S , it is meaningful to define the average *conditional* fidelity F_c . If we only accept the final state if it is in S , the squared overlap between the conditional, renormalized state $\frac{PUP|\psi\rangle}{\|PUP|\psi\rangle\|}$ and the ideal state $U_0P|\psi\rangle$ must be weighted with the acceptance probability $\|PUP|\psi\rangle\|^2$ and renormalized by the integrated acceptance probability over the input Hilbert space $\int \|PUP|\psi\rangle\|^2 dV$. Hence, we obtain the average conditional fidelity³

$$\begin{aligned}
F_c &= \int |\langle \psi | PU_0^\dagger \frac{PUP}{\|PUP|\psi\rangle\|} | \psi \rangle|^2 \cdot \frac{\|PUP|\psi\rangle\|^2}{\int \|PUP|\psi\rangle\|^2 dV} dV \\
&= \frac{\int |\langle \psi | PU_0^\dagger PUP | \psi \rangle|^2 dV}{\int \langle \psi | PU^\dagger PUP | \psi \rangle dV} \\
&= \frac{1}{n_{rel} + 1} \cdot \frac{\text{Tr}(U_0^\dagger PUPU^\dagger PU_0) + |\text{Tr}(U_0^\dagger PUP)|^2}{\text{Tr}(U^\dagger PUP)},
\end{aligned}$$

where the numerator is evaluated using Theorem 1 and the denominator follows from $\int \langle \psi | M | \psi \rangle dV = \text{Tr}(M)/n$.

The design of composite pulses (see chapter 3.4.4), or smooth control theory pulses, to implement gates with good robustness against variations in atomic parameters, is significantly facilitated with our simple fidelity expression (2.4). Thus, we have made extensive use of it in the numerical simulations presented in the subsequent chapter 4.

³This expression replaces the erroneous formula in [I].

2.1.3 Average fidelity of a general quantum operation

In a number of quantum information scenarios, ancillary quantum systems are used to mediate the desired operations: quantum memory protocols in a very explicit manner involve an extra quantum system, quantum teleportation requires an extra entangled pair of systems, and in quantum computing with trapped ions, a motional degree of freedom is used to couple the particles. The ancillary systems are ideally disentangled from the qubits before and after the process, but in general they act as an environment and cause decoherence of the quantum system of interest. This forces us to generalize the formalism even further and take into account the general theory of quantum operations, according to which density matrices are transformed by completely positive maps. According to the Kraus representation theorem, any completely positive trace-preserving map \mathcal{G} admits the representation

$$\mathcal{G}(\rho) = \sum_k G_k \rho G_k^\dagger, \quad (2.5)$$

where $\sum_k G_k^\dagger G_k = I_n$ is the $n \times n$ identity matrix [7]. If there is only one G_k , (2.5) must be unitary and we return to the case discussed in chapter 2.1.1. The more general expression allows interactions with an ancilla system followed by a partial trace over that system. It entails the effects of dissipative coupling to the surroundings and of measurements on the system, in which case the G_k may represent the associated projection operators and possible conditioned feedback operations applied to the system. It is a powerful feature of Theorem 1 that it is easily extended to allow computation of the average fidelity for protocols, which apply or which are subject to these more general operations.

If the pure input state $\rho = |\psi\rangle\langle\psi|$ is mapped to the output state $\mathcal{G}(\rho)$ the mean fidelity with which our operation yields a unitary transformation U_0 is

$$\begin{aligned} F &= \int_{S^{2n-1}} \langle\psi|U_0^\dagger \mathcal{G}(|\psi\rangle\langle\psi|)U_0|\psi\rangle dV \\ &= \sum_k \int_{S^{2n-1}} |\langle\psi|M_k|\psi\rangle|^2 dV \\ &= \frac{1}{n(n+1)} \left\{ \text{Tr} \left(\sum_k M_k^\dagger M_k \right) + \sum_k |\text{Tr}(M_k)|^2 \right\}, \end{aligned} \quad (2.6)$$

where $M_k = U_0^\dagger G_k$, and $\{G_k\}$ are the Kraus operators for the map \mathcal{G} .

The Kraus representation is not unique as the map \mathcal{G} may be represented by an alternative set of operators $\{G'_k\}$, where $G'_k = \sum_j V_{kj} G_j$ and V is a unitary transformation among the Kraus operators⁴. We notice, however,

⁴Note that if the set $\{G'_k\}$ contains more elements than $\{G_k\}$, some zero operators are added to the set $\{G'_k\}$ such that the two sets have the same cardinality.

that the first term in (2.6) is the identity, which is unchanged, and, since

$$\begin{aligned}
\sum_k |\text{Tr}(M_k)|^2 &= \sum_k \text{Tr}(M_k^\dagger) \text{Tr}(M_k) \\
&= \sum_{ij} \text{Tr}(M_j'^{\dagger}) \text{Tr}(M_i') \sum_k V_{jk}^\dagger V_{ki} \\
&= \sum_j \text{Tr}(M_j'^{\dagger}) \text{Tr}(M_j') \\
&= \sum_k |\text{Tr}(M_k')|^2,
\end{aligned}$$

the fidelity is invariant under the transformation.

Equation (2.6) enables the calculation of the average fidelity of any quantum operation, as soon as it has been put in the Kraus form. If a system, for example, undergoes dissipation, we can take this into account together with other imperfections, and from the general solution of the associated Lindblad master equation we can determine the average fidelity of our quantum state operation. By the procedure outlined in [7], the general propagator for the master equation can be systematically put in the Kraus operator form. We also note the recent work [34], that explicitly provides a Kraus form solution of the Lindblad master equation.

Applications of the general fidelity formula

To illustrate the use of the general fidelity formula (2.6), we apply it to the depolarizing channel that leaves a qubit state unchanged with probability p and transforms it into a random state $I_2/2$ with probability $1 - p$. This may occur as a consequence of a continuous perturbation with a rate γ ($p = \exp(-\gamma t)$), or it may represent the outcome of a teleportation process [26, 27] where the channel is not occupying an ideal maximally entangled two-qubit state $|\Psi\rangle$, but the mixed state $\rho_{Ent} = p|\Psi\rangle\langle\Psi| + ((1 - p)/4)I_4$. The transformation of our qubit is represented by the action of four Kraus operators, $M_0 = (\sqrt{3p + 1}/2)I_2$, $M_\chi = (\sqrt{1 - p}/2)\sigma_\chi$, where σ_χ with $\chi = x, y, z$ are the Pauli matrices. The mean fidelity of state preservation under the depolarizing channel, or for the teleportation of a qubit by the mixed state, follows readily from (2.6) and is

$$F_{depolarized} = \frac{1}{6}(2 + (3p + 1)) = \frac{1 + p}{2},$$

as expected.

Another example is atomic decay from an upper to a lower qubit level with rate Γ , where the Kraus map is given by two operators,

$$M_0 = \begin{pmatrix} 1 & 0 \\ 0 & \exp(-\Gamma t/2) \end{pmatrix} \quad \text{and} \quad M_1 = \begin{pmatrix} 0 & \sqrt{1 - \exp(-\Gamma t)} \\ 0 & 0 \end{pmatrix}.$$

In an analysis using Monte-Carlo Wave Functions [35] these operators represent the no-jump and the jump evolution, respectively, weighted by the corresponding time-dependent probability factors. The fidelity (2.6) is readily evaluated with the result:

$$F_{decay} = \frac{1}{6}(3 + \exp(-\Gamma t) + 2 \exp(-\Gamma t/2)).$$

It is straightforward to apply our equations (2.3), (2.4), and (2.6). This is a great advantage, particularly for higher dimensional systems, where the explicit integration over the space of initial states becomes cumbersome, and where even the algebraic expressions in [27,28] become involved.

2.1.4 Average fidelity of general operations on composite quantum systems

Our formalism can be used to determine the fidelity of more complex operations. For example, a K -qubit or K -qudit quantum register, such as error correcting codes [36,37], if K is not too large.

Let us consider a simple example, where each qubit or qudit is subject to the same operation, which may be either unitary or a Kraus form operation. This scenario is relevant for the teleportation of a full quantum register by sequential or parallel teleportation of every individual bit, or simply for the storage of a quantum register suffering from independent decoherence mechanisms on every bit. If the Kraus operators for a single qudit are denoted M_k , the Kraus operators for K qudits are tensor product combinations of the M_k 's of the form $\mathcal{M}_{\vec{k}} = \otimes_i^K M_{k_i}$, with $\vec{k} = (k_1, k_2, \dots, k_K)$. It follows from (2.6) that the average over the n^K dimensional Hilbert space is

$$\begin{aligned} F_{n^K} &= \frac{1}{n^K + 1} + \frac{1}{n^K(n^K + 1)} \sum_{\vec{k}} |\text{Tr}(\mathcal{M}_{\vec{k}})|^2 \\ &= \frac{1}{n^K + 1} + \frac{1}{n^K(n^K + 1)} \left(\sum_k |\text{Tr}(M_k)|^2 \right)^K, \end{aligned}$$

where we have used that $\text{Tr} \left(\otimes_i^K M_{k_i} \right) = \prod_i^K \text{Tr}(M_{k_i})$. Interestingly, using (2.6), we can express the sum $\sum_k |\text{Tr}(M_k)|^2$ in terms of the single qudit fidelity F_n . Hence, we obtain the relation between the K -qudit and the single-qudit transformation fidelities:

$$F_{n^K} = \frac{1}{n^K + 1} \left(1 + ((n + 1)F_n - 1)^K \right). \quad (2.7)$$

We note that if $F_n = 1$, also $F_{n^K} = 1$, and due to (2.6), $F_n \geq 1/(n + 1)$ for any map. This consistently implies that $F_{n^K} \geq 1/(n^K + 1)$. Contrary to what

one might expect, the fidelity for K independent qudits is not just F_n^K , but it is given by the more complicated expression (2.7). This is due to the fact that the K th power of the one qudit fidelity formula only describes how fast qubit *product states* decay on average, it does not average over initial entangled states of the qudits in the register. Equation (2.7) implies that for $F_n = 1 - \epsilon$, where $\epsilon \ll 1$, $F_{n^K} \sim 1 - n^K(n+1)/n(n^K+1) \cdot K\epsilon$, which is smaller than $F_n^K \sim 1 - K\epsilon$. For the special case of many qubits, $n = 2$ and $K \gg 1$, and we have the result $F_{n^K} \sim F_n^{3K/2}$.

The result (2.7) and the limiting values described above are valid for any operation applied to the individual qudits, it only assumes that they are all subject to the same individual dynamics. For few qudit systems, one may generalize these results to the case of different operations on the individual components, if, for example, part of the qubits in a quantum register are transferred to an interaction region by teleportation.

2.2 The fidelity distribution

Apart from the mean fidelity, it may be interesting to know the probability distribution for the single-state fidelity f (that is, the integrand in (2.1), $|\langle \psi | M | \psi \rangle|^2$). Thus, one may pose the question whether f is peaked around the average fidelity F or if it displays a broader distribution.

Unfortunately, obtaining an explicit expression for the fidelity probability distribution is a difficult problem, as witnessed by the probability for f for a Hermitian matrix M , studied originally by von Neumann [38]. We, however, derive a formula for the special case of a two by two unitary diagonalizable matrix in chapter 2.2.2 and study the general case numerically in chapter 2.2.3. Furthermore, we obtain an explicit formula for the variance of the fidelity distribution for a unitary operator and a unitary operator projected onto a smaller quantum system, as presented in chapter 2.2.1.

2.2.1 The variance

To obtain an explicit formula for the variance of the fidelity distribution for a unitary operator, we shall derive a relation for the uniform average of f^2 , i.e., $|\langle \psi | M | \psi \rangle|^4$, where M is any linear operator. However, let us first consider the case where M is a Hermitian operator.

Lemma 1. *For any Hermitian operator S acting on an n -dimensional complex Hilbert space, the uniform average of $|\langle \psi | S | \psi \rangle|^4$ over state vectors $|\psi\rangle$ on the unit sphere S^{2n-1} in \mathbb{C}^n is given by*

$$\int_{S^{2n-1}} |\langle \psi | S | \psi \rangle|^4 dV = \frac{1}{n(n+1)(n+2)(n+3)} \times \\ [6\text{Tr}(S^4) + 8\text{Tr}(S^3)\text{Tr}(S) + 3\text{Tr}(S^2)^2 + 6\text{Tr}(S^2)\text{Tr}(S)^2 + \text{Tr}(S)^4], \quad (2.8)$$

where dV is the normalized measure on the sphere.

Proof. The proof of Lemma 1 is very much along the lines of the proof of Theorem 1. As before, we note the conjugation invariance of (2.8), which allows us to prove this equation simply by demonstrating that it holds for a real, diagonal matrix Λ . Letting L denote the left-hand side of (2.8), we observe that $L(\Lambda)$ is a homogeneous polynomial of degree 4 in the real variables $\lambda_1, \dots, \lambda_n$, which is invariant under the exchange of any two λ_i and λ_j . It is easy to demonstrate that the set

$$\left\{ \text{Tr}(\Lambda^4), \text{Tr}(\Lambda^3)\text{Tr}(\Lambda), \text{Tr}(\Lambda^2)^2, \text{Tr}(\Lambda^2)\text{Tr}(\Lambda)^2, \text{Tr}(\Lambda)^4 \right\}$$

spans $L(\Lambda)$, and by choosing five appropriate matrices and evaluating the integrals

$$\begin{aligned} \int_{S^{2n-1}} |c_i|^8 dV &= \frac{24}{n(n+1)(n+2)(n+3)} \\ \int_{S^{2n-1}} |c_i|^4 |c_j|^4 dV &= \frac{4}{n(n+1)(n+2)(n+3)} \\ \int_{S^{2n-1}} |c_i|^6 |c_j|^2 dV &= \frac{6}{n(n+1)(n+2)(n+3)} \\ \int_{S^{2n-1}} |c_i|^4 |c_j|^2 |c_k|^2 dV &= \frac{2}{n(n+1)(n+2)(n+3)} \\ \int_{S^{2n-1}} |c_i|^2 |c_j|^2 |c_k|^2 |c_l|^2 dV &= \frac{1}{n(n+1)(n+2)(n+3)}, \end{aligned} \quad (2.9)$$

for i, j, k, l pairwise different, we finally obtain (2.8) by solving a linear system of equations. \square

Note that (2.8) also holds for an anti-Hermitian matrix A , since $L(A) = L(iA) = R(iA) = R(A)$, where L and R denote the left- and right-hand sides of (2.8), respectively.

Having obtained the uniform average of $|\langle \psi | M | \psi \rangle|^4$, where M is Hermitian, let us derive a relation for the case where M is any linear operator.

Theorem 2. For any linear operator M acting on an n -dimensional complex Hilbert space, the uniform average of $|\langle \psi | M | \psi \rangle|^4$ over state vectors $|\psi\rangle$ on the unit sphere S^{2n-1} in \mathbb{C}^n is given by

$$\begin{aligned} \int_{S^{2n-1}} |\langle \psi | M | \psi \rangle|^4 dV &= \\ &= \frac{1}{n(n+1)(n+2)(n+3)} [4\text{Tr}(M^2 M^{\dagger 2}) + 2\text{Tr}(M M^{\dagger} M M^{\dagger}) \\ &+ 4\text{Tr}(M)\text{Tr}(M M^{\dagger 2}) + 4\text{Tr}(M^{\dagger})\text{Tr}(M^2 M^{\dagger}) + \text{Tr}(M^2)\text{Tr}(M^{\dagger 2}) \\ &+ 2\text{Tr}(M M^{\dagger})^2 + \text{Tr}(M^2)\text{Tr}(M^{\dagger})^2 + \text{Tr}(M)^2\text{Tr}(M^{\dagger 2}) \\ &+ 4\text{Tr}(M)\text{Tr}(M^{\dagger})\text{Tr}(M M^{\dagger}) + \text{Tr}(M)^2\text{Tr}(M^{\dagger})^2], \end{aligned} \quad (2.10)$$

where dV is the normalized measure on the sphere.

Proof. Decomposing the general matrix M as a sum of a Hermitian and an anti-Hermitian matrix, denoted by S and A , respectively, we note that

$$\int_{S^{2n-1}} |\langle \psi | M | \psi \rangle|^4 dV = \int_{S^{2n-1}} |\langle \psi | S | \psi \rangle|^4 + |\langle \psi | A | \psi \rangle|^4 + 2|\langle \psi | S | \psi \rangle|^2 |\langle \psi | A | \psi \rangle|^2 dV. \quad (2.11)$$

The first two terms on the right-hand side of (2.11) are readily evaluated using Lemma 1 and the explicit expressions $S = (M + M^\dagger)/2$ and $A = (M - M^\dagger)/2$. To calculate the third term, we observe that

$$\int_{S^{2n-1}} |\langle \psi | S | \psi \rangle|^2 |\langle \psi | A | \psi \rangle|^2 dV = \int_{S^{2n-1}} |\langle \psi | \Lambda | \psi \rangle|^2 |\langle \psi | \tilde{A} | \psi \rangle|^2 dV, \quad (2.12)$$

where $\Lambda = USU^{-1}$ is a diagonal matrix with elements $\lambda_1, \dots, \lambda_n \in \mathbb{R}$, and $\tilde{A} = UAU^{-1}$ is an anti-Hermitian matrix, which is not necessarily diagonal. Writing $|\psi\rangle = \sum c_j |j\rangle$ and employing the unitary invariance of the integral (2.12) (in particular when considering the transformation $c_j \rightarrow \exp(i\theta_j)c_j$), it follows that

$$\begin{aligned} & \int_{S^{2n-1}} |\langle \psi | \Lambda | \psi \rangle|^2 |\langle \psi | \tilde{A} | \psi \rangle|^2 dV = \\ & \int_{S^{2n-1}} \sum_{\alpha, \beta, i, j, k, l} |c_\alpha|^2 |c_\beta|^2 c_i^* c_l^* c_j c_k \lambda_\alpha \lambda_\beta \tilde{A}_{ij} \tilde{A}_{kl}^* (\delta_{ij} \delta_{kl} + \delta_{ik} \delta_{jl} - \delta_{ij} \delta_{kl} \delta_{il}) dV = \\ & \frac{1}{n(n+1)(n+2)(n+3)} \left\{ 24 \sum_i \lambda_i^2 |\tilde{A}_{ii}|^2 + \sum'_{i \neq j \neq k \neq l} \lambda_k \lambda_l (\tilde{A}_{ii} \tilde{A}_{jj}^* + |\tilde{A}_{ij}|^2) + \right. \\ & 4 \sum'_{i \neq j} \left[(\lambda_j^2 + 3\lambda_i \lambda_j) |\tilde{A}_{ii}|^2 + (3\lambda_i^2 + 2\lambda_i \lambda_j) (\tilde{A}_{ii} \tilde{A}_{jj}^* + |\tilde{A}_{ij}|^2) \right] + \\ & \left. 2 \sum'_{i \neq j \neq k} \left[\lambda_i \lambda_j |\tilde{A}_{kk}|^2 + (\lambda_k^2 + 4\lambda_i \lambda_k) (\tilde{A}_{ii} \tilde{A}_{jj}^* + |\tilde{A}_{ij}|^2) \right] \right\}, \end{aligned} \quad (2.13)$$

where the last sign of equality follows upon insertion of (2.9). The notation \sum' indicates that the indices are pairwise different. After a lengthy, but straightforward calculation, (2.13) can be rewritten in terms of traces of products of powers of Λ and \tilde{A} . Invoking trace invariance, we can replace Λ and \tilde{A} with S and A , respectively, and insert the explicit expressions for S and A in terms of M . Collecting terms in (2.11), we finally obtain (2.10). \square

Combining Theorems 1 and 2, we obtain the variance of the fidelity distribution for a unitary transformation using

$$\sigma^2 = \int_{S^{2n-1}} |\langle \psi | M | \psi \rangle|^4 dV - \left(\int_{S^{2n-1}} |\langle \psi | M | \psi \rangle|^2 dV \right)^2,$$

with $M = U_0^\dagger U$, where U_0 and U are the desired and actual evolution operators of the system, respectively. As in chapter 2.1.2, this result is easily extended to the case where the average is solely performed over a subset of input states by simply replacing n with n_{rel} , and M with $M_{rel} = U_0^\dagger P U P$, where P is the projection operator on the relevant subspace and U_0 represents the desired dynamics for the relevant subspace. However, Theorem 2 is, regrettably, not easily extendable to accommodate the case of a general quantum operation.

2.2.2 The fidelity distribution for a two by two normal matrix

In this chapter, we obtain an explicit expression for the fidelity distribution for a two by two unitarily diagonalizable matrix, i.e., a normal matrix. Consider first the following theorem:

Theorem 3. *If M is a normal 2×2 matrix with eigenvalues λ_0, λ_1 arranged such that $|\lambda_0| \leq |\lambda_1|$, then for $\lambda_0 \neq \lambda_1$ the probability distribution for $f = |\langle \psi | M | \psi \rangle|^2$ is given by*

$$P_f = \frac{1}{2|\lambda_0 - \lambda_1|} \frac{1}{\sqrt{f - f_0}}, \quad |\lambda_0|^2 \leq f \leq |\lambda_1|^2, \quad (2.14)$$

unless $\text{Re}(\lambda_1/\lambda_0) \leq 1$ ($|\lambda_0 - \frac{1}{2}\lambda_1| \geq \frac{1}{2}|\lambda_1|$), in which case it is given by

$$P_f = \begin{cases} \frac{1}{|\lambda_0 - \lambda_1|} \frac{1}{\sqrt{f - f_0}}, & f_0 \leq f \leq |\lambda_0|^2, \\ \frac{1}{2|\lambda_0 - \lambda_1|} \frac{1}{\sqrt{f - f_0}}, & |\lambda_0|^2 \leq f \leq |\lambda_1|^2, \end{cases} \quad (2.15)$$

where $f_0 = \text{Im}(\lambda_0 \lambda_1^*)^2 / |\lambda_0 - \lambda_1|^2$.

Proof. If $M = U \Lambda U^{-1}$, such that Λ is diagonal with eigenvalues λ_0, λ_1 arranged according to $|\lambda_0| \leq |\lambda_1|$, and $U \in U(2)$, the single-state fidelity $f = |\langle \psi | M | \psi \rangle|^2$ reduces to $|\langle \psi | \Lambda | \psi \rangle|^2 = |c_0|^4 |\lambda_0|^2 + |c_1|^4 |\lambda_1|^2 + |c_0|^2 |c_1|^2 (\lambda_0 \lambda_1^* + \lambda_0^* \lambda_1)$, where $|\psi\rangle = c_0 |0\rangle + c_1 |1\rangle$ is written in the basis of the eigenstates of M . Employing the parametrization $c_0 = e^{i\chi} \cos(\theta/2)$ and $c_1 = e^{i(\chi+\phi)} \sin(\theta/2)$, where $\phi \in [0, 2\pi]$ and $\theta, \chi \in [0, \pi]$, we have $f = |\lambda_0|^2 f_\lambda$, where

$$f_\lambda = \cos^4 \frac{\theta}{2} + \sin^4 \frac{\theta}{2} |\lambda|^2 + \cos^2 \frac{\theta}{2} \sin^2 \frac{\theta}{2} (\lambda + \lambda^*), \quad (2.16)$$

and $\lambda = \lambda_1/\lambda_0$. The probability of obtaining a θ smaller than a given t is

$$\begin{aligned}
 \int_{-\infty}^t P_\theta(\theta) d\theta &= V(\{(\chi, \theta, \phi) | \theta < t\}) / V(S^3) \\
 &= \frac{1}{2\pi^2} \int_{\{(\chi, \theta, \phi) | \theta < t\}} dV \\
 &= \frac{1}{2\pi^2} \int_{\{(\chi, \theta, \phi) | \theta < t\}} \frac{1}{2} \sin \theta d\chi d\theta d\phi \\
 &= \int_0^t \frac{1}{2} \sin \theta d\theta,
 \end{aligned} \tag{2.17}$$

where for the fourth step we used that the square root of the Jacobian determinant equals $\sin \theta/2$, and we exploited the invariance of χ, ϕ to integrate out these parameters. Differentiating (2.17) with respect to t , we conclude that

$$P_\theta = \frac{1}{2} \sin \theta, \quad \theta \in [0, \pi]. \tag{2.18}$$

If $f_\lambda(\theta)$ is monotone, we have that

$$P_{f_\lambda} = \left| \frac{d\theta}{df_\lambda} \right| P_\theta. \tag{2.19}$$

Otherwise, we have to add contributions from those intervals where it is monotone. Since

$$\frac{df_\lambda}{d\theta} = \frac{1}{2} \sin \theta (|\lambda|^2 - 1 - |1 - \lambda|^2 \cos \theta), \tag{2.20}$$

it follows that $df_\lambda/d\theta$ is zero only at the endpoints, i.e., at $\theta = 0, \pi$, and at $\theta_c = \arccos((|\lambda|^2 - 1)/|1 - \lambda|^2)$, see Fig. 2.1. As $|\cos \theta_c| \leq 1$, the requirement $\operatorname{Re}(\lambda) \leq 1$ (and $\lambda \neq 1$) arise if θ_c is to be defined.

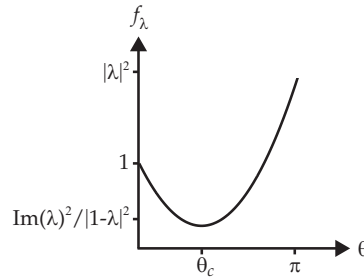


Figure 2.1. f_λ as a function of θ for the case where θ_c is defined.

For cases where θ_c is not defined, f_λ is monotone on the interval $\theta \in [0, \pi]$ with range $[1, |\lambda|^2]$, since it follows from the assumption $|\lambda_0| \leq |\lambda_1|$ that

$|\lambda| \geq 1$. Combining (2.18), (2.19), and (2.20) we obtain

$$P_{f_\lambda} = \left| |\lambda|^2 - 1 - |1 - \lambda|^2 \cos \theta \right|^{-1}, \quad (2.21)$$

where, from (2.16),

$$\cos \theta = \frac{|\lambda|^2 - 1 \pm 2\sqrt{f_\lambda |1 - \lambda|^2 - \text{Im}(\lambda)^2}}{|1 - \lambda|^2}. \quad (2.22)$$

Since it is assumed that θ_c is not defined it follows that f is monotone. Consequently, only one solution is applicable, and either the plus or the minus sign must be chosen in (2.22). In that, $f_{\lambda, \min} = 1$ is larger than the term $\text{Im}(\lambda)^2/|1 - \lambda|^2$, which corresponds to the minimum value of f_λ to ensure that the term under the square root in (2.22) is positive, it follows that the right-hand side is defined for all f_λ in the domain. Inserting (2.22) into (2.21) gives

$$P_{f_\lambda} = 1 / \left(2\sqrt{f_\lambda |1 - \lambda|^2 - \text{Im}(\lambda)^2} \right), \quad 1 \leq f_\lambda \leq |\lambda|^2, \quad (2.23)$$

regardless of the sign chosen in (2.22). Thus, for the case where θ_c is undefined, we finally obtain (2.14) by exploiting

$$P_f = \left| \frac{df_\lambda}{df} \right| P_{f_\lambda} = P_{f_\lambda} / |\lambda_0|^2. \quad (2.24)$$

If θ_c is defined we must consider the intervals $[0, \theta_c]$ and $[\theta_c, \pi]$ separately and, by inverting f_λ in the relevant branch in Fig. 2.1, subsequently add their contributions to P_{f_λ} . For $[0, \theta_c]$ only the plus solution of (2.22) is valid and we find that f_λ must fulfill $\text{Im}(\lambda)^2/|1 - \lambda|^2 \leq f_\lambda \leq 1$, whereas for $[\theta_c, \pi]$ the minus solution holds and we find $\text{Im}(\lambda)^2/|1 - \lambda|^2 \leq f_\lambda \leq |\lambda|^2$. In both cases, inserting (2.21) gives (2.23) and, adding the distributions obtained for the two intervals, we finally obtain (2.15) by making use of (2.24). \square

In principle, Theorems 1 and 2 can be demonstrated in the special case of M being a normal 2×2 matrix from Theorem 3 using $\langle f \rangle = \int_{f_{\min}}^{f_{\max}} P_f f df$ and $\langle f^2 \rangle = \int_{f_{\min}}^{f_{\max}} P_f f^2 df$, respectively.

Setting $M = U_0^\dagger U$, where U_0 and U are the desired and actual evolution operators of the system, respectively, we immediately obtain the fidelity distribution from Theorem 3. In this case, M has eigenvalues $e^{i\phi_0}, e^{i\phi_1}$. If $\phi_0 \neq \phi_1$, (2.15) is relevant and we obtain

$$P_f = \frac{1}{2 \sin\left(\frac{\phi_1 - \phi_0}{2}\right) \sqrt{f - \cos^2\left(\frac{\phi_1 - \phi_0}{2}\right)}},$$

for $\cos^2((\phi_1 - \phi_0)/2) \leq f \leq 1$. The obtained minimum fidelity is a special case of the minimum fidelity formula for any unitary operator, which was derived in [39]:

$$f_{min} = \begin{cases} \cos^2(\Delta\phi_{max}/2) & \text{if } \Delta\phi_{max} \geq \pi, \\ 0 & \text{otherwise,} \end{cases}$$

where $\Delta\phi_{max} = \max(\{\phi_j - \phi_{j-1}\}_{j=1,\dots,n-1} \cup \{2\pi + \phi_0 - \phi_{n-1}\})$, when the eigenvalues of $M = U_0^\dagger U$ are ordered such that $0 \leq \phi_0 \leq \dots \leq \phi_{n-1} \leq 2\pi$.

For the case considered in chapter 2.1.2, where $M = U_0^\dagger PUP$, M is not necessarily normal and in general Theorem 3 is therefore not applicable. However, in some cases it can be employed. By way of example, consider the method described in [40] for utilizing dark states to perform arbitrary qubit rotations. Here, rotations between qubit states $|0\rangle$ and $|1\rangle$ are achieved by simultaneously coupling the states resonantly to an excited state $|e\rangle$ with complex Rabi frequencies $\Omega_{R0}(t)e^{-i\phi_0}$ and $\Omega_{R1}(t)e^{-i\phi_1}$, respectively. For $\Omega_{R0}(t) = \Omega_{R1}(t)$, a new orthonormal basis is chosen, such that $|\bar{0}\rangle = (|0\rangle - e^{-i\phi}|1\rangle)/\sqrt{2}$ and $|\bar{1}\rangle = (|0\rangle + e^{-i\phi}|1\rangle)/\sqrt{2}$. Now, if the relative phase of the fields fulfills $\phi_1 - \phi_0 = \phi$, only $|\bar{1}\rangle$ couples to $|e\rangle$ (and vice versa if $\phi_1 - \phi_0 = \phi + \pi$). Applying two π pulses, the second with a shift of $\pi + \theta$ on both ϕ_0 and ϕ_1 , ideally implements $U_0 = \begin{pmatrix} 1 & 0 \\ 0 & e^{i\theta} \end{pmatrix}$ in the basis $\{|\bar{0}\rangle, |\bar{1}\rangle\}$. However, if the rotations between $|\bar{1}\rangle$ and $|e\rangle$ are imperfect, we obtain $U = \begin{pmatrix} 1 & 0 & 0 \\ 0 & \alpha & \gamma \\ 0 & \gamma^* & \beta \end{pmatrix}$ in the basis $\{|\bar{0}\rangle, |\bar{1}\rangle, |e\rangle\}$, implying that $PUP = \begin{pmatrix} 1 & 0 \\ 0 & \alpha \end{pmatrix}$ in the basis $\{|\bar{0}\rangle, |\bar{1}\rangle\}$. It follows that M is normal and the fidelity distribution is immediately obtained from Theorem 3.

2.2.3 The numerical fidelity distribution

In order to construct the fidelity distribution for any operator, we make use of numerical simulations. To effectively generate random points on a hypersphere of arbitrary dimension, we use the method of [41]. This invokes creating n Gaussian random variables $\tilde{x}_1, \tilde{x}_2, \dots, \tilde{x}_n$, from which uniformly distributed vectors x are obtained over the surface S^{n-1} using

$$x = \frac{1}{\sqrt{\tilde{x}_1^2 + \tilde{x}_2^2 + \dots + \tilde{x}_n^2}} \begin{pmatrix} \tilde{x}_1 \\ \tilde{x}_2 \\ \vdots \\ \tilde{x}_n \end{pmatrix}.$$

Employing the parametrization $|\psi\rangle = \sum_j c_j |j\rangle$, where $c_j = x_{2j+1} + ix_{2j+2}$, the distribution of f can be found.

As a check of our theoretical fidelity distribution, we observe from Fig. 2.2 that (2.15) is consistent with our numerical findings. The vertical bars indi-

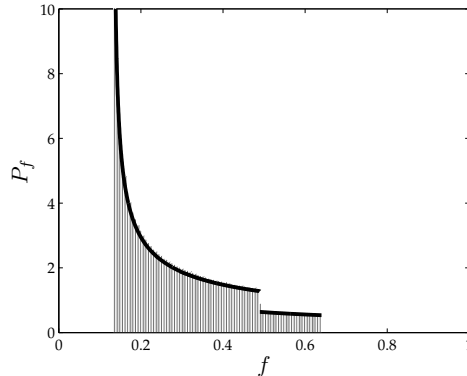


Figure 2.2. Theoretical (line) and numerical (histogram) fidelity distribution for a matrix with eigenvalues $\lambda_0 = 0.7 \cdot e^{i\pi/8}$ and $\lambda_1 = 0.8 \cdot e^{i4\pi/5}$. From (2.1) and (2.10) it follows that $\langle f \rangle = 0.279$ and $\langle f^2 \rangle = 0.096$, respectively. The minimum fidelity is $f_{\min} = f_0 = 0.133$ from (2.15).

cate the histogram obtained by choosing states on the Bloch sphere at random, as described above, and binning their individual fidelities. In addition, we observe that our theoretical predictions for the uniform averages of f and f^2 coincide with the numerical results.

2.3 Summary

We have presented a derivation, and shown various applications, of a simple and compact expression for the average fidelity of a general quantum operation. Alternative expressions, involving discrete sums over a large number of initial states, have been discussed previously in the literature with emphasis on quantum process tomography. To our knowledge, the expression involving only simple combinations of the trace of the relevant Kraus operators has not been used in direct fidelity calculations.

Our simple expression is a good starting point for further analysis, e.g., for the achievements of error correcting codes [36], decoherence-free subspaces [42, 43], and protection of quantum information by dynamical decoupling [44]. Our expression can also be handled and generalized analytically, as illustrated by our study of a K -qudit register, which provides insight into the scaling of errors. This may have applications in quantum error correction, the capacity of quantum channels, and the way that, e.g., communication with quantum repeaters [21] and entanglement distillation should optimally be carried out.

We apply an average over pure states, but we note that it is possible, and also very interesting, to define fidelities for mixed initial states, and to

perform averages over mixed states [45]. Since mixed states can be synthesized as the partial trace of pure states on a larger system, we imagine that the accomplishments of operations on mixed states can also be addressed with our formalism. The ability to restrict averages to subspaces may enable generalization of our formalism to deal with non-uniform averages, assuming nontrivial prior probability distributions on the Hilbert space. Also, in infinite-dimensional Hilbert spaces we may use our formulas, omitting the $n(n+1)$ prefactor, to *define* relative fidelity measures for any trace class operators. By means of the regularized traces used for quantum field theory [46], it is even possible to extend such measures canonically to certain non-trace class operators.

Finally, we have studied the fidelity distribution, which we imagine may be interesting in connection with the design of for instance error correcting codes or composite pulses, by obtaining an explicit formula for the variance, which is not applicable for a general quantum operator, but in a number of very interesting quantum information scenarios.

We also derived an expression for the distribution itself, which is applicable in a limited number of cases. It is possible to expand our method to deal with more general operators. Numerical simulations allow us to deal with any operator.

Introduction to neutral atom quantum computing

A distinguishing feature of neutral atom quantum computing is that neutral atoms, being uncharged, are weakly coupled to their environment. This implies very long coherence times, and hence neutral atoms appear to be very good candidates for storing quantum information. The qubit basis states can be identified as, for example, two hyperfine states of the ground level of an alkali metal atom. Easy manipulation of the qubits can be achieved using external fields, such as microwave radiation or laser light, and complete control of the system parameters is then possible.

Unfortunately, it is not straightforward to identify a suitable interaction which couples two neutral atoms. This is in contrast to the case of ions, for which the Coulomb interaction offers strong coupling at the expense of a stronger coupling to the environment. However, for neutral atoms, two-qubit gates can be implemented by employing controllable internal-state dependent interactions between the atoms, such as controlled cold collisions [47], cavity-mediated photon exchange [48], and dipole-dipole interactions between Rydberg atoms [23]. In this thesis, we study solely the latter implementation.

In this chapter, we study a possible way of implementing NAQC in practice: how to trap the atoms, how to choose the qubit basis states (chapter 3.1), how to perform initialization (chapter 3.2) and read out (chapter 3.3), and how to carry out single-qubit gates (chapter 3.4) and two-qubit gates (chapter 3.5). Finally, we provide a brief review of the experimental progress on NAQC (chapter 3.6). The chapter is a review of known results except for chapter 3.4.6, which is our own contribution.

3.1 The qubit basis states

Neutral atoms can be captured in the ‘egg carton’-style potential of a far-off-resonance trap (FORT). This is formed by tightly focusing laser light in a chosen set of locations and using the ground state AC Stark shift to create the position-dependent potential of the individual wells [49]. Single atoms can be loaded into the FORT after precooling in a magneto-optical trap (MOT) [25].

An optimal choice of qubit basis states minimizes the amount of dephasing caused by fluctuations in the trapping and background magnetic fields. The atoms used in experiments by both the group of Saffman and Walker and the group of Grangier are ^{87}Rb with a nuclear spin of $I = 3/2$. To achieve long storage times and low decoherence the following two hyperfine states of the ground level are used [25]:

$$\begin{aligned} |0\rangle &\equiv |F = 1, m_F = 0\rangle, \\ |1\rangle &\equiv |F = 2, m_F = 0\rangle. \end{aligned}$$

The hyperfine splitting for these states is $\omega_{hf}/2\pi \approx 6.83$ GHz in the absence of a magnetic field. This choice of basis gives zero first-order sensitivity to magnetic fields. However, a small magnetic bias field (15 mG is sufficient [25]) must be applied in order to suppress transitions between the Zeeman sublevels.

Qubit decoherence. The various physical mechanisms that limit the coherence of the qubit basis states are carefully studied in [25]. Background gas collisions, photon scattering of FORT light and laser noise induced heating all contribute to decreasing the coherence time of the diagonal density matrix elements (T_1). The qubits are affected equally so no dephasing of the qubit basis states is caused. However, background magnetic and electric fields, limit the coherence time of the off-diagonal matrix elements (T_2). Moreover, intensity noise and atomic motion result in a time-dependent AC Stark shift, which is also responsible for dephasing. The estimates obtained in [25] are $T_1 \sim 12$ s and $T_2 \sim 2$ s.

3.2 Initialization

The system can be initialized by optical pumping to the $|1\rangle$ state. This can be carried out by applying light linearly polarized along the magnetic field which is resonant with the $|S_{1/2}, F = 2\rangle \leftrightarrow |P_{3/2}, F' = 2\rangle$ transition, see Fig. 3.1¹. Since the states with $m_F = 0$ are not coupled by the light (cf. $\Delta F = 0$), all population will eventually end up in the $|S_{1/2}, F = 2, m_F = 0\rangle$ state due

¹Note that the applied magnetic field is so small that the transitions between the Zeeman sublevels are all resonant.

to spontaneous emission. The $|S_{1/2}, F = 2\rangle$ state has a much longer lifetime than the $|P_{3/2}, F' = 2\rangle$ state, but the inevitable population loss to the ground state can be corrected for by applying a repumper beam. The initialization procedure can be performed in approximately $0.1 \mu\text{s}$ [25]. Based on experiments with atomic beams [50], a preparation purity of order 10^{-4} can be expected.

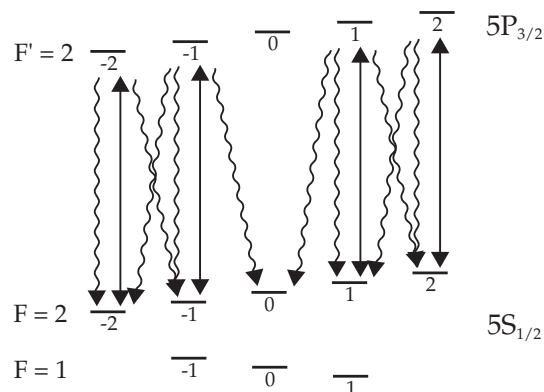


Figure 3.1. The initialization procedure. The solid lines represent lasers driving the $\Delta m_F = 0$ transitions. The wavy lines indicate population loss from the upper states to the lower states by spontaneous emission.

3.3 Read out

The read-out method is based on resonance fluorescence [51]. In [25] it is proposed to perform rapid state selective measurements by applying σ_+ polarized light tuned close to the $|S_{1/2}, F = 2, m_F = 2\rangle \leftrightarrow |P_{3/2}, F' = 3, m_{F'} = 3\rangle$ cycling transition, see Fig. 3.2. If the number of detected photons exceeds a certain cutoff, the qubit is measured to be in state $|1\rangle$. The measurement time must be sufficiently long that the photons emitted spontaneously can be resolved above the noise. In [25] it is estimated that accurate measurements can be performed in less than $100 \mu\text{s}$.

An alternative read-out method is to entangle the qubit with an ensemble using the Rydberg blockade technique (see chapter 3.5.2) as proposed in [52]. Reading out the state of the ensemble is advantageous in that local operations are faster and the emitted light is directional (see chapter 6), which increases the photon detection rate. For experimentally realistic parameters this makes the total read-out process faster, even when accounting for the additional operations necessary to entangle the qubit and the ensemble. It is estimated that by this method it is feasible to achieve a read-out time ten times smaller than that possible via resonance fluorescence [52].

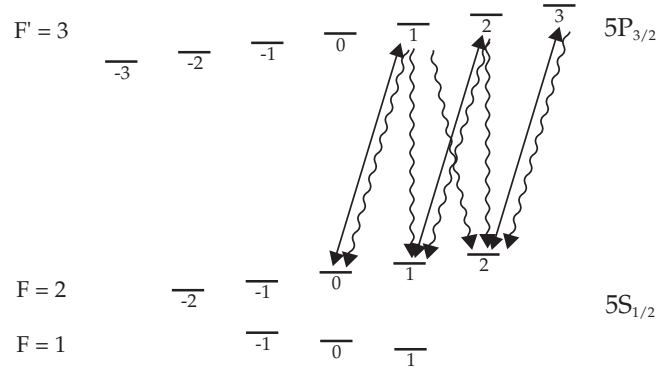


Figure 3.2. The read-out procedure. By applying lasers resonant with the $\Delta m_F = 1$ transitions (solid lines), population initially in $|1\rangle = |F = 2, m_F = 0\rangle$ eventually ends up in the two right-most states. Detection of light emitted by spontaneous emission (wavy lines) from $|F' = 3, m_F = 3\rangle$ to $|F = 2, m_F = 2\rangle$ indicates initial population of $|1\rangle$.

3.4 Single-qubit gates

Next, we study the implementation of single-qubit gates for NAQC. In principle, single-qubit rotations between $|0\rangle$ and $|1\rangle$ can be carried out using a microwave field resonant with ω_{10} . Unfortunately, this setting does not allow direct single-site addressing [25]. Instead, we shall resort to stimulated two-photon Raman transitions. In principle, this allows for rotations between the qubit basis states that are straightforward to implement. However, errors do come into play and we discuss possible ways of dealing with these. In particular, we consider errors arising from atomic motion in the trap.

3.4.1 Two-photon Raman transitions

A two-photon Raman transition involves the simultaneous absorption and stimulated emission of light by an atom, in the configuration illustrated in Fig. 3.3. This level structure is denoted a lambda (Λ) system and consists of a single excited state $|e\rangle$ mediating transitions between two lower states, $|0\rangle$ and $|1\rangle$. Transitions to $|e\rangle$ from each of the lower states are dipole allowed. However, transitions $|0\rangle \leftrightarrow |1\rangle$ are dipole forbidden, implying that $|1\rangle$ is a metastable state with a very long lifetime. If the single-photon detunings are large compared to the Rabi frequencies and the two-photon detuning, the excited state does not acquire population during the transition $|0\rangle \leftrightarrow |1\rangle$. Thus, spontaneous emission from $|e\rangle$ is negligible, as opposed to the case of two single-photon transitions.

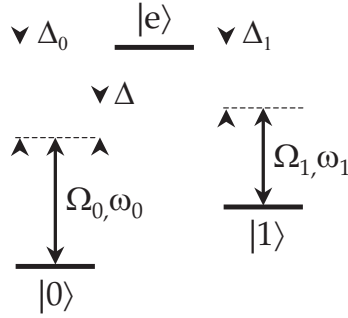


Figure 3.3. The three-level Λ system used for single-qubit rotations. Two lasers with Rabi frequencies $\Omega_j = \mathbf{d}_{ej} \cdot \mathbf{E}_{j,0} e^{i\mathbf{k}_j \cdot \mathbf{r}} / \hbar$ couple the qubit states with an effective Rabi frequency $\Omega_R = \Omega_0 \Omega_1^* / (\Delta_0 + \Delta_1)$. The single-photon detunings are defined by $\Delta_i = \omega_i - \omega_{ei}$ and the two-photon detuning by $\Delta = \Delta_0 - \Delta_1$.

In the semiclassical approximation, valid if the fields are sufficiently strong, the electromagnetic fields are treated as classical vector fields. The interaction Hamiltonian between the two fields and the lambda system is

$$H = -\mathbf{d} \cdot \mathbf{E}, \quad (3.1)$$

where

$$\mathbf{d} = \mathbf{d}_{e0} \sigma_{e0} + \mathbf{d}_{e1} \sigma_{e1} + \text{h.c.},$$

$\sigma_{ij} = |i\rangle\langle j|$, and $\mathbf{E} = \mathbf{E}_0 + \mathbf{E}_1$, where

$$\mathbf{E}_j = \frac{1}{2} \left(\mathbf{E}_{j,0} e^{i(\mathbf{k}_j \cdot \mathbf{r} - \omega_j t)} + \text{c.c.} \right).$$

Applying two standard techniques, the rotating wave approximation and adiabatic elimination², the evolution of the lambda system can be described in the interaction picture basis $\{|0\rangle, |1\rangle\}$ by the operator

$$R(\theta, \phi) = \begin{pmatrix} e^{i\frac{\Delta}{2}t} \left[\cos\left(\frac{\theta}{2}\right) - i\frac{\Delta'}{|\Omega|} \sin\left(\frac{\theta}{2}\right) \right] & -ie^{i\frac{\Delta}{2}t} \frac{|\Omega_R|}{|\Omega|} e^{-i\phi} \sin\left(\frac{\theta}{2}\right) \\ -ie^{-i\frac{\Delta}{2}t} \frac{|\Omega_R|}{|\Omega|} e^{i\phi} \sin\left(\frac{\theta}{2}\right) & e^{-i\frac{\Delta}{2}t} \left[\cos\left(\frac{\theta}{2}\right) + i\frac{\Delta'}{|\Omega|} \sin\left(\frac{\theta}{2}\right) \right] \end{pmatrix}. \quad (3.2)$$

The pulse area is denoted $\theta = |\Omega|t$ and the relative phase of the two lasers is ϕ , such that $\Omega_R = |\Omega_R|e^{i\phi}$. Furthermore, $\Omega = (\text{Re}(\Omega_R), \text{Im}(\Omega_R), \Delta')$ and $\Delta' = \Delta + (|\Omega_0|^2 - |\Omega_1|^2) / 2(\Delta_0 + \Delta_1)$. All other definitions are given in

²Adiabatic elimination of the excited state is possible due to the negligible population of $|e\rangle$. However, ambiguities exist in the standard treatment, which we have dealt with in our paper [III].

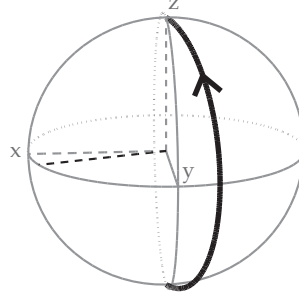


Figure 3.4. Evolution of the Bloch vector (black, solid line) during a $\pi_{\pi/10}$ pulse. The state $|0\rangle$ (south pole) is rotated π degrees around the axis $\hat{\mathbf{n}} = \cos(\pi/10)\hat{\mathbf{x}} + \sin(\pi/10)\hat{\mathbf{y}}$ (black, dashed line) such that it ends up in $|1\rangle$ (north pole).

Fig. 3.3. We refer to Appendix A for details.

Bloch-sphere picture. A useful way to visualize the dynamics of two-level systems is to introduce the Bloch sphere picture. Defining the Bloch vector

$$\mathbf{S} = \begin{pmatrix} 2\text{Re}(c_1^*c_0) \\ 2\text{Im}(c_1^*c_0) \\ |c_1|^2 - |c_0|^2 \end{pmatrix},$$

where $|\psi\rangle = c_0|0\rangle + c_1|1\rangle$, the evolution described by (3.2) corresponds to a clockwise rotation of \mathbf{S} by an angle θ around the axis $\hat{\mathbf{\Omega}}$ on the unit sphere. In particular, for $\Delta = 0$ the rotation axis is $\hat{\mathbf{n}} = \cos(\phi)\hat{\mathbf{x}} + \sin(\phi)\hat{\mathbf{y}}$. Note that henceforth we shall adopt the notation θ_ϕ to denote a pulse with parameters θ and ϕ . An example of a rotation on the Bloch sphere is illustrated in Fig. 3.4.

3.4.2 Constructing single-qubit gates

Any arbitrary unitary operator can be approximated by appropriately combining a small number of so-called universal gates (as mentioned in chapter 1). The standard set of universal gates consists of the Hadamard, phase, controlled-NOT, and $\pi/8$ gates [7]. The phase gate corresponds to two $\pi/8$ gates, so (in addition to the CNOT gate) it suffices to implement the following two single-qubit gates in a physical system

$$T = \begin{pmatrix} 1 & 0 \\ 0 & e^{i\pi/4} \end{pmatrix},$$

$$H = \frac{1}{\sqrt{2}} \begin{pmatrix} 1 & 1 \\ 1 & -1 \end{pmatrix},$$

where T is the $\pi/8$ gate, and H is the Hadamard gate. From (3.2), we see that applying two lasers with numerically equal Rabi frequencies ($|\Omega_0| = |\Omega_1|$) for an amount of time t such that $\theta = |\Omega|t = 2\pi$, and with a detuning fulfilling $\Delta \cdot t = -\frac{\pi}{4}$, T is implemented up to a global phase factor. For the same two lasers, but this time on two-photon resonance ($\Delta = 0$), H is achieved up to a global phase factor by first applying a π_π pulse and subsequently a $\pi/2_{-\pi/2}$ pulse. This corresponds to $R\left(\frac{\pi}{2}, -\frac{\pi}{2}\right) \cdot R(\pi, \pi)$.

In addition to construction of single-qubit gates, single-qubit rotations are used as building blocks for two-qubit gates. We are particularly interested in swapping two states, which can be implemented using a pulse with $\theta = \pi$. To obtain real coefficients we choose $\phi = \frac{\pi}{2}$. The corresponding pulse $\pi_{\pi/2}$ has the rotation matrix $R\left(\pi, \frac{\pi}{2}\right) = \begin{pmatrix} 0 & -1 \\ 1 & 0 \end{pmatrix}$. The minus sign entails that a $2\pi_{\pi/2}$ pulse endows the states with a phase shift of π even though the Bloch vector is returned to the same point on the Bloch sphere.

3.4.3 Implementing single-qubit gates

Single-qubit rotations can be carried out using a stimulated two-photon Raman transition, as demonstrated above. In practice, for ^{87}Rb , the Raman light is tuned close to either the $5P_{1/2}$ or the $5P_{3/2}$ excited state. With a fine structure splitting of 7120 GHz, contributions from the other $5P$ state can be neglected.

A correction to the effective Rabi frequency Ω_R arises from the hyperfine structure of the excited state. The state $5P_{1/2}$ has two hyperfine levels $F = 1$ and $F = 2$, with a splitting of $\Delta_e/2\pi = 817$ MHz. Taking this substructure of $|e\rangle$ into account leads to the following expression for Ω_R [25]:

$$\Omega_R = \frac{2\pi e^2}{\epsilon_0 c \hbar^2} \left(\frac{1}{2} \|rY_1^1\| \frac{1}{2} \right)^2 \frac{I}{9} \frac{\Delta_{01} - \Delta_e/4}{\Delta_{01} (\Delta_{01} - \Delta_e)}. \quad (3.3)$$

We refer to Appendix B for details.

Single-qubit gates based on stimulated Raman transitions can be carried out with a high fidelity. Error sources include spontaneous emission, AC Stark shifts induced by the Raman beams, atomic motion, spatial crosstalk, polarization leakage, laser intensity noise, and laser phase noise. In [25] the authors estimate the combined fidelity error to be of order 10^{-4} . Additionally, with a $5P_{1/2}$ lifetime of 27.7 ns, transitions can be made quite free of decoherence due to spontaneous emission. Thus, with a single-photon detuning of $\Delta_0/2\pi \approx -100$ GHz, the probability of spontaneous emission from the excited state is approximately $9 \cdot 10^{-5}$. Atomic motion and spatial crosstalk will be specifically addressed in chapter 3.4.6, but first we review some of the commonly used error compensation techniques for two-level systems.

3.4.4 Composite pulses

In the Bloch picture off-resonance or pulse length errors result in rotational imperfections. Replacing single with multiple rotations can greatly improve robustness and lead to an almost ideal evolution when small errors are present. Such a composite sequence comprises rectangular pulses, i.e., their amplitude is constant and only their duration and phase are varied. The evolution matrix describing them is (3.2) for an effective two-level system. The two types of errors and examples of pulses correcting for them are discussed in the following.

Composite pulses are used extensively in NMR (see [53] for a detailed review). There are two main classes: type A works for any initial state whereas type B only works for some initial states. In the context of quantum computing, type A pulses are preferable as a given gate should work for all initial states. However, type B pulses can sometimes be applied as building blocks for two-qubit gates. In [54] various pulses suitable for quantum computation are listed. Note that the problem of correcting pulse length and off-resonance errors simultaneously using type A pulses is as yet unresolved.

Pulse length errors

Pulse length errors occur when the duration of the pulse is set incorrectly, or (equivalently) when the field strength deviates from its nominal value, i.e., when $|\Omega'| = \gamma|\Omega|$, where $|\Omega'|$ is the actual value and $|\Omega|$ is the nominal value. The actual rotation angle θ' thus differs from the nominal rotation angle θ as $\theta' = \gamma\theta$.

To deal with these kinds of errors in the particular case of population swapping (i.e., $|0\rangle \leftrightarrow |1\rangle$), one can apply the composite pulse sequence $90_0 180_{90} 90_0$, which ideally implements a π rotation around the \hat{x} axis. As can be seen on Fig. 3.5a, performing a $\frac{\pi}{2}$ rotation around the \hat{x} axis followed by a π rotation around the \hat{y} axis and a $\frac{\pi}{2}$ rotation around the \hat{x} axis compensates for pulse length errors (and to some extent off-resonance errors).

To perform an arbitrary rotation, one can use the type A composite pulse sequence called SCROFULOUS [54]. Assuming a three-pulse sequence, optimal parameters for the angles and phases are determined such that the first-order error term vanishes with the constraint that the composite pulse should be time symmetric (i.e., $\theta_1 = \theta_3$ and $\phi_1 = \phi_3$). The parameters for a rotation θ_0 (i.e., a rotation with θ degrees around the \hat{x} axis) are found to be $\theta_1 = \theta_3 = \arcsin(2 \cos(\theta/2)/\pi)$, $\phi_1 = \phi_3 = \arccos(-\pi \cos(\theta_1)/2\theta_1 \sin(\theta/2))$, and $\theta_2 = \pi$, $\phi_2 = \phi_1 - \arccos(-\pi/2\theta_1)$. A pulse with a different phase angle ϕ is obtained by offsetting all the phase angles by ϕ . A special case is the 180_{315} rotation which is implemented by the sequence $180_{15} 180_{255} 180_{15}$. Figure 3.5b shows that even a 10% error in the Rabi frequency is well com-

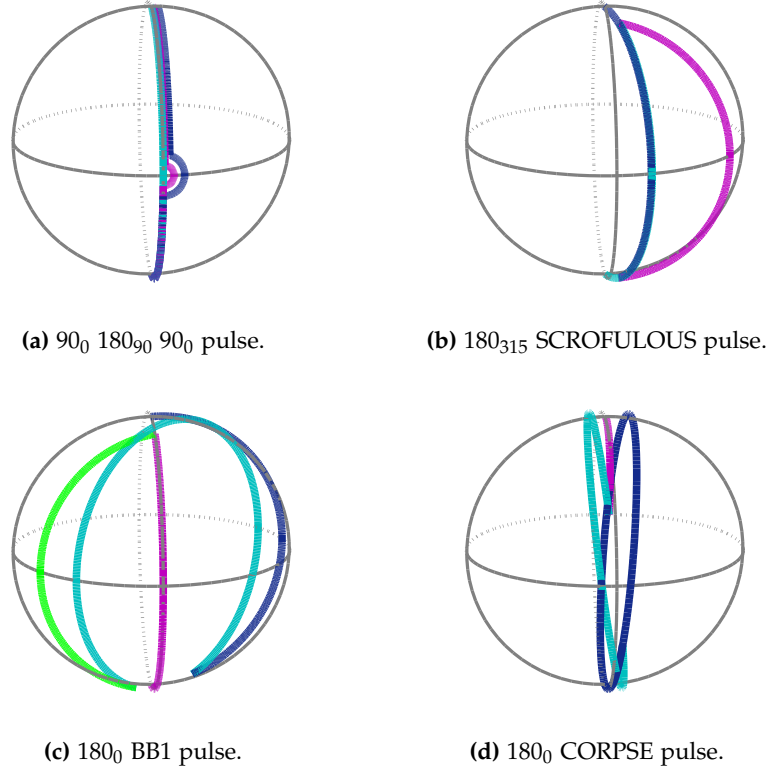


Figure 3.5. The evolution of $|0\rangle$ on the Bloch sphere during various composite pulse sequences. The desired outcome is a rotation from $|0\rangle$ (south pole) to $|1\rangle$ (north pole). The axes are the same as in Fig. 3.4. In (a) we correct for pulse length errors with γ equal to 1 (turquoise), 0.95 (purple), and 0.9 (blue). In (b) we correct for $\gamma = 0.9$ by applying the sequence of pulses 180_{15} (turquoise), 180_{255} (purple), and 180_{15} (blue). In (c) we correct for $\gamma = 0.9$ using first the 180_0 pulse (purple) followed by 180_{ϕ_1} (green), 360_{ϕ_2} (turquoise), and 180_{ϕ_1} (blue), where $\phi_1 = \arccos(-1/4)$ and $\phi_2 = 3\phi_1$. In (d) we correct for an off-resonance error of $\varepsilon = 0.1$ using the sequence 420_0 (blue), 300_{180} (turquoise), and 60_0 (purple).

pensated for.

In the schemes mentioned above, one replaces a single pulse with a sequence of pulses performing the desired rotation and compensating for the errors at the same time. Wimperis [55] introduced type A composite pulses where one first applies a single pulse, ideally achieving the desired evolution, and then follow it by a sequence of pulses partially correcting the errors. Of particular interest is the BB1 pulse (broadband number 1) family.

In this case, one performs a θ_x pulse using the sequence $180_{\phi_1} 360_{\phi_2} 180_{\phi_1} \theta_x$.³ As before, implementing a θ_ϕ pulse requires offsetting all pulse angles by the phase ϕ . Optimal values are $\phi_1 = \arccos(-\theta/720^\circ)$ and $\phi_2 = 3\phi_1$. The pulse sequence for a 180_x pulse is shown in Fig. 3.5c for a 10% error in the Rabi frequency. The BB1 pulse is well suited for correcting pulse length errors over a wide range of γ , hence its name. It performs better and is less sensitive to off-resonance effects than the SCROFULOUS scheme, but is somewhat slower.

Off-resonance errors

A nonzero (two-photon) detuning Δ results in a modification of the rotation angle, which takes the actual value $\theta' = \theta\sqrt{1 + \varepsilon^2}$, where $\varepsilon = \Delta/|\Omega_R|$ and θ is the nominal rotation angle. Furthermore, the rotation axis is tilted as $\hat{\Omega}$ acquires a nonzero z-component.

To deal with off-resonance errors, one may employ the type A composite pulse scheme called CORPSE (compensating for off-resonance with a pulse sequence) scheme [54]. In this case, a θ_x pulse is implemented by a sequence of three pulses applied along the \hat{x} , $-\hat{x}$ and \hat{x} axes, respectively. As usual, a θ_ϕ pulse is implemented by off-setting the phase angles by ϕ . The optimal rotation angles are $\theta_1 = 2\pi + \theta/2 - \arcsin(\sin(\theta/2)/2)$, $\theta_2 = 2\pi - 2\arcsin(\sin(\theta/2)/2)$, and $\theta_3 = \theta/2 - \arcsin(\sin(\theta/2)/2)$. The impressive performance for a 180_x pulse is demonstrated in Fig. 3.5d.

3.4.5 Complex hyperbolic secant pulse

For population swapping one can use a particular pulse of type B called the complex hyperbolic secant pulse. For this pulse, the complex Rabi frequency is

$$\Omega_R(t) = \Omega_{R,0} [\operatorname{sech}(\beta(t - t_0))]^{1+i\mu},$$

where μ is a real constant, $\Omega_{R,0}$ is the maximum Rabi frequency, and β is related to the pulse width. The result is a real hyperbolic secant pulse for which the instantaneous frequency (given by the time derivative of the phase) is swept during the pulse, i.e.,

$$\begin{aligned} |\Omega_R(t)| &= \Omega_{R,0} \operatorname{sech}(\beta(t - t_0)), \\ v(t) &= v_0 - \frac{\mu\beta \tanh(\beta(t - t_0))}{2\pi}. \end{aligned}$$

Hence we have $-\beta\mu < \Delta < \beta\mu$.

An analytic solution to the analogous NMR problem is derived in [56]. Let u, v, w be the three components of the Bloch vector \mathbf{S} . Then, for $\Delta = 0$

³To obtain a time symmetric pulse, the correcting pulse sequence can also be placed in the middle of the θ_x pulse, cf. [54].

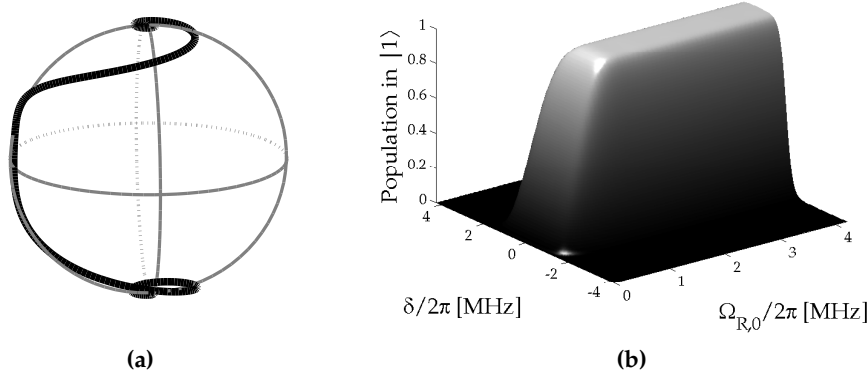


Figure 3.6. (a) The evolution of $|0\rangle$ during the hyperbolic secant pulse for $\Omega_{R,0}/2\pi = 1.4$ MHz and $\delta = 0.05 \Omega_{R,0}$. (b) Final state population as a function of $\Omega_{R,0}$ and δ . Parameters are $\beta/2\pi = 0.45$ MHz, and $\mu = 3$.

and a detuning error δ , the following equations can be derived from (A.2) with the term $-\delta\sigma_{11}$ added:

$$\begin{aligned}\dot{u} - i\dot{v} &= i\Omega_R w + i\delta(u - iv), \\ \dot{w} &= \frac{i}{2}(\Omega_R^*(u - iv) - \Omega_R(u - iv)^*).\end{aligned}$$

By defining $M = u - iv$, $M_z = -w$, and $\Delta w = \delta$, we find these equations to be identical to the NMR Bloch equations in [56]. Thus, for $\Omega_R \geq \mu\beta$, the analytic expression for the final level population difference is

$$\begin{aligned}w &= -\tanh\left(\pi\left(\frac{\delta}{2\beta} + \frac{\mu}{2}\right)\right)\tanh\left(\pi\left(\frac{\delta}{2\beta} - \frac{\mu}{2}\right)\right) \\ &+ \cos\left(\pi\left(\left(\frac{\Omega_R}{\beta}\right)^2 - \mu^2\right)^{1/2}\right)\text{sech}\left(\pi\left(\frac{\delta}{2\beta} + \frac{\mu}{2}\right)\right)\text{sech}\left(\pi\left(\frac{\delta}{2\beta} - \frac{\mu}{2}\right)\right).\end{aligned}\quad (3.4)$$

For $\mu \geq 2$, the second term in (3.4) has negligible influence on the value of w . Hence, if Ω_R exceeds the threshold value $\mu\beta$, w is essentially independent of Ω_R . Moreover, the pulse is narrowband with respect to δ , meaning that, for a small interval in δ , w is almost independent of δ . The performance of the hyperbolic secant pulse is illustrated in Fig. 3.6.

3.4.6 Correcting for atomic motion

After our general discussion of error correcting pulses, we now discuss how these techniques can be applied to the physical system of neutral atoms

trapped in a FORT. That is, in particular we consider single-qubit gate errors due to atomic motion.

The intensity of a laser beam (applied to perform single-qubit rotations) varies with position. Hence, if the motion of an atom in the trap is large on the scale of the waist of the beam, the Rabi frequency will be position dependent. This gives rise to (time-dependent) pulse length errors.

Applying a Raman beam with a larger waist would diminish this error, but would at the same time lead to increased crosstalk between neighboring sites. Increasing the spacing between the traps in order to reduce this crosstalk is not tenable, as this would lessen the interaction between neighboring atoms and decrease the fidelity of the two-qubit operations. Great care must be taken to choose the parameter values that lead to the best compromise.

For our estimates in the following we employ the parameters of [25]. The variation of the Rabi frequency with respect to the atomic position is given by $\Omega_R(r) = \Omega_{R,0} e^{-2r^2/w_0^2}$, which follows from the intensity profile $I(r) = I_0 e^{-2r^2/w_0^2}$ for a Gaussian beam, where $r = \sqrt{x^2 + y^2}$ is the distance from the origin in the plane and $w_0 = 5 \mu\text{m}$ is the waist of the beam. In the FORT, the atoms are at a temperature of $T_a = 50 \mu\text{K}$, and the radial oscillation frequency is $\omega_r/2\pi = 30 \text{ kHz}$. With these values we find that $k_B T_a / \hbar \omega_r = 35$, implying that the system is in the classical regime and Maxwell-Boltzmann statistics can be applied to calculate the average atomic speed. This gives the following estimates: $\langle v_x^2 \rangle = \langle v_y^2 \rangle = \langle v_z^2 \rangle = k_B T_a / m$. From the virial theorem it follows that $\langle x^2 \rangle = \langle y^2 \rangle = w_{f0}^2 T_a / 4T_f = (0.3 \mu\text{m})^2$, where $w_{f0} = 2.5 \mu\text{m}$ is the waist of the FORT beam and $T_f = 1 \text{ mK}$ is the maximum depth of the potential well expressed in temperature units. This yields a variation in Ω_R of order $\Delta\Omega_R \sim 0.01\Omega_R$.

For this variation of Ω_R , and for a spacing of $d = 8 \mu\text{m}$ between neighboring atoms, the Rabi frequency in the center of the adjacent trap is $0.006\Omega_R$. Thus, for the atom in the neighboring trap, a rotation of θ causes an error of $1 - |\langle I\psi | R(\gamma\theta, \phi)\psi \rangle|^2 = 1 - \cos^2(\frac{\gamma\theta}{2})$, where $\gamma = e^{-2d^2/w_0^2}$. For a π pulse, with the values stated above, the error is of order 10^{-4} .

With the radial frequency $\omega_r/2\pi = 30 \text{ kHz}$, it follows that the atoms oscillate radially in the trap with a period of $t_{osc} = 2\pi/\omega_r = 33 \mu\text{s}$. Comparing this with the gate time $t_{gate} = \pi/|\Omega_R| = 0.36 \mu\text{s}$, for a π pulse with a Rabi frequency of $2\pi \cdot 1.4 \text{ MHz}$ (a typical value in the experiments by Saffman and Walker), it follows that an atom hardly moves during gate operation. However, for composite pulses, the extended duration of the gate allows for more movement during the gate. Consequently, for a constant pulse, the Rabi frequency is almost constant during the gate.

In addition to inducing pulse-length errors, atomic motion gives rise to a Doppler shift, which leads to off-resonance errors. From the above estimate for $\langle v_z^2 \rangle$ follows a root-mean-square speed of $v_z = 0.07 \text{ m/s}$, resulting

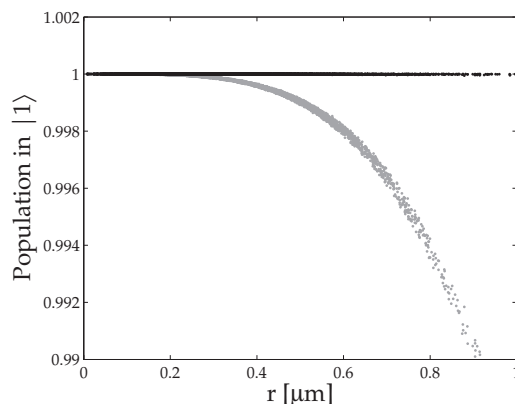


Figure 3.7. Final state population as a function of the initial position of an atom initially in $|0\rangle$ for a 180_0 pulse (gray dots) and a 180_0 BB1 pulse (black dots). Parameters used for the numerical simulation are $\Omega_{R,0}/2\pi = 1.4$ MHz, $\Delta_0^0/2\pi = 40$ GHz, and $\Delta^0 = 0$. Additional parameters are stated in the text.

in a Doppler shift of $\delta\nu/\nu = v_z/c = 2 \cdot 10^{-10}$ as the Raman beams are orthogonal to the plane. If the two Raman beams come from the same direction, the levels $|0\rangle$ and $|1\rangle$ are shifted by nearly the same amount relative to $|e\rangle$ and the two-photon detuning Δ will remain almost unchanged. Letting Δ^0 denote the value without Doppler shift, the detuning is given by $\Delta = \Delta^0 + v_z\omega_{10}/c$, where $\omega_{10}/2\pi = 6.83$ GHz. Thus, the correction to Δ is of order $\delta\Delta_0/2\pi \sim 2$ Hz, which is very small compared to the Rabi frequencies. The off-resonance error arising from the Doppler shift is accordingly expected to be quite small. There is also a small correction to the Rabi frequency from $\Omega_R = \Omega_0\Omega_1^*/(\Delta_0 + \Delta_1)$. The single-photon detunings are shifted approximately 0.1 MHz, which is a small correction to the typical values of 40 GHz.

To summarize, atomic motion leads to both pulse length errors and off-resonance errors. However, from our estimates we expect the latter to be negligible compared to the first. Since the Rabi frequency is almost spatially constant, composite pulse sequences correcting for pulse length errors are expected to significantly reduce the drop in fidelity caused by atomic motion. This is clearly confirmed by our numerical simulations presented in Fig. 3.7, where population transfer from $|0\rangle$ to $|1\rangle$ is carried out using a simple π pulse and a BB1 pulse. The figure depicts the final state population as a function of the initial position of the atom. The atomic motion during the gate operation is taken into account by evolving the position of the atom as a harmonic oscillator in a number of discrete time steps. Initial position and momentum coordinates are generated randomly according to

a Gaussian distribution. As is clear from the figure, the composite pulse sequence effectively compensates for the pulse length errors experienced by atoms away from the center of the trap. Thus, the mean fidelity for our present simulation is increased from 0.9992 to 1.0000 by employing the BB1 composite pulse scheme. However, the disadvantage of composite pulses is the extended gate duration and increased crosstalk originating from a larger pulse area of the composite pulse. In this case, the composite pulse area is five times the area of the simple π pulse.

Inspired by our proposal to rectify errors caused by atomic motion using composite pulses, the group of Saffman and Walker has constructed a composite pulse system for single-qubit rotations between the ground hyperfine states. Work is in progress to demonstrate a full BB1 pulse [57].

3.5 Two-qubit gates

Designing fast two-qubit gates for NAQC is quite tricky. In particular, it is difficult to find a two-atom interaction that is strong (to allow for fast gates), controllable, and that does not entangle the internal and motional degrees of freedom by mechanical forces. However, various proposals for a controllable internal-state dependent interaction have been put forward. For instance, controlled cold collisions [47], cavity-mediated photon exchange [48], and dipole-dipole interactions between atoms excited to their Rydberg states [23]. In this thesis we consider only the latter.

In the following, we shall see how the dipole-dipole interaction of Rydberg atoms can be utilized to implement a completely entangling two-qubit gate. A controlled phase gate is implemented by exciting the atoms to their Rydberg levels state dependently and by means of local operations it can be converted into a CNOT gate (chapter 3.5.2). Alternatively, the Rydberg-Rydberg interaction can be employed to implement a controlled phase gate based on motional effects [58].

3.5.1 The dipole-dipole interaction of Rydberg atoms

Rydberg atoms, neutral atoms with an electron in a state with a large principal quantum number n . These atoms can realize the Bohr model's circular orbits having huge geometric cross sections with radii given by $a_0(Z_{eff})^{-1}n^2$, where a_0 is the Bohr radius and Z_{eff} is the effective atomic number. Rydberg atoms can thus be as big as simple bacteria with radii of order $0.1 \mu\text{m}$. With respect to quantum information processing, Rydberg atoms are of great interest given that they exhibit relatively long lifetimes and large dipole moments resulting in strong dipole-dipole interaction between two Rydberg atoms [59]. The interaction can be enhanced either by applying an electric field or by using nearly degenerate states which are strongly mixed by the

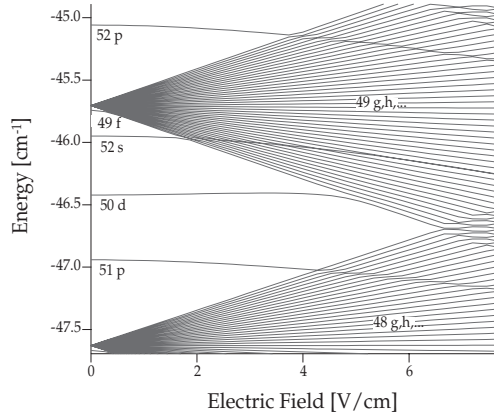


Figure 3.8. Stark map for states near $n = 50$. The figure is reproduced from [60] by courtesy of Mark Saffman.

dipole-dipole interaction. This allows for strong interaction between atoms that are just a few micrometers apart, as described below.

First, we consider Rydberg atoms in the presence of an electric field. An electric field which is large enough to strongly mix states of different angular momenta can enhance the dipole-dipole interaction between Rydberg atoms [25]. As Fig. 3.8 illustrates, for an electric field between 5 and 6 V/cm, the energy of the $50d$ state depends linearly on the field. This implies a field independent dipole moment (given by the slope of the energy, which in this case is $3300 ea_0$ [60]). The dipole-dipole interaction energy is

$$V_{rr} = \frac{1}{4\pi\epsilon_0 r^3} (\boldsymbol{\mu}_1 \cdot \boldsymbol{\mu}_2 - 3(\boldsymbol{\mu}_1 \cdot \hat{\mathbf{r}})(\boldsymbol{\mu}_2 \cdot \hat{\mathbf{r}})), \quad (3.5)$$

and taking $\boldsymbol{\mu}_1 = \boldsymbol{\mu}_2 = \boldsymbol{\mu}$, (3.5) simplifies to

$$V_{rr} = \frac{\mu^2}{4\pi\epsilon_0 r^3} (1 - 3\cos^2\theta),$$

where \mathbf{r} is the radius vector from atom 1 to atom 2, $\boldsymbol{\mu}_k$ is the dipole moment operator of atom k and θ is the angle between the interatomic axis and the electric field. The interaction energy is maximized for $\theta = 0$. Since μ scales as n^2 , the interaction is huge. However, an apparent downside is the directional dependence induced by the electric field.

In the absence of an electric field, the Rydberg-Rydberg interaction can be enhanced using resonances. For example, consider the states $ns + ns$ and $np + (n-1)p$. Since they are nearly degenerate the dipole-dipole interaction can strongly mix these states resulting in new two-atom states significantly shifted in energy. The Hamiltonian is $H = H_0 + V_{rr}$, where H_0 is the single-atom Hamiltonian and V_{rr} is the dipole-dipole interaction energy (3.5)

scaling as $1/r^3$. In [61] it is shown that by diagonalizing H the states split up into three levels with energies E_p , $E_+ = E_p + \hbar\Delta_{rr}$, and $E_- = E_s - \hbar\Delta_{rr}$, where E_s is the energy of the state $ns + ns$, E_p is the energy of $np + (n-1)p$, and

$$\Delta_{rr} = \frac{1}{2} \left(\sqrt{\delta^2 + 48\Gamma_{rr}^2} - \delta \right), \quad (3.6)$$

where $\hbar\delta = E_p - E_s = E((n-1)p) + E(np) - 2E(ns)$, $\hbar\Gamma_{rr} = \mu_{n-1}\mu_n/r^3$, and $\mu_{n'} = \langle n'p, \alpha k | \hat{\mu}_{\alpha k} | ns, k \rangle$, where $\mu_k = (\mu_{xk}, \mu_{yk}, \mu_{zk})$ is the dipole moment operator of atom k . From (3.6) it follows that if the states are resonant, i.e., $\delta = 0$, the energy shift Δ_{rr} scales as $1/r^3$. Alternatively, if δ is much larger than Γ_{rr} , the energy shift scales as $1/r^6$.

In the absence of an electric field, $\delta = -3000$ MHz for $n = 50$. But since the energies are shifted in the presence of an electric field, due to the Stark effect (see Fig. 3.8), it is possible to modify δ by varying the electric field. Unfortunately, as is evident from Fig. 3.8, applying a small field (in the range 0-4 V/cm) can only decrease δ . We could therefore be tempted to make use of other resonances, for instance $nd + nd \leftrightarrow (n+1)p + (n-1)f$, in which case it would indeed be possible to adjust the associated detuning in the desired way. However, Γ_{rr} vanishes for the molecular states of symmetry $^3\Sigma_u^+$ and $^1\Sigma_g^+$ because of the degeneracy of the d levels [60].

In general, it can be demonstrated that the long-range $1/r^3$ interaction produced by resonances $nlj + nlj \leftrightarrow n'l'j' + n''l''j''$ vanishes unless $l' = l'' = l + 1$ [60]. Taking Zeeman degeneracies into account it turns out that, for most choices of Rydberg states, there exist superpositions of Zeeman levels with extremely small van der Waals interactions. Since it can be shown that the figure of merit for the blockade is sensitive primarily to the weakest possible interactions (rather than the mean interaction strength) between the various degenerate Rydberg states, it follows that Zeeman degeneracies can lower the interaction strength considerably [62]. In general, it can be demonstrated that the linear combinations with zero dipole-dipole coupling, the so-called Förster-zero states, always exist if $\min(j', j'') < j$, but are absent for $\min(j', j'') > j$. For $\min(j', j'') = j$, precise zeros are not necessarily present. However, a state with very small dipole-dipole coupling always exists [62].

As an example of attainable interaction strengths, Fig. 3.9 displays the calculated Δ_{rr} as a function of interatomic distance for various principal quantum numbers near the resonance of the two-atom states $ns + ns \leftrightarrow np_{1/2(3/2)} + (n-1)p_{1/2(3/2)}$. The calculation has been carried out for cesium atoms. However, the energy shifts for rubidium do not differ significantly. As appears from the figure, it is possible to achieve an interaction strength close to 1 GHz for $n = 70$ at a separation of $3 \mu\text{m}$ and about 80 MHz at a separation of $5 \mu\text{m}$. The latter is sufficient for one Rydberg excited atom to block the excitation to Rydberg levels of all other atoms in a small sample of

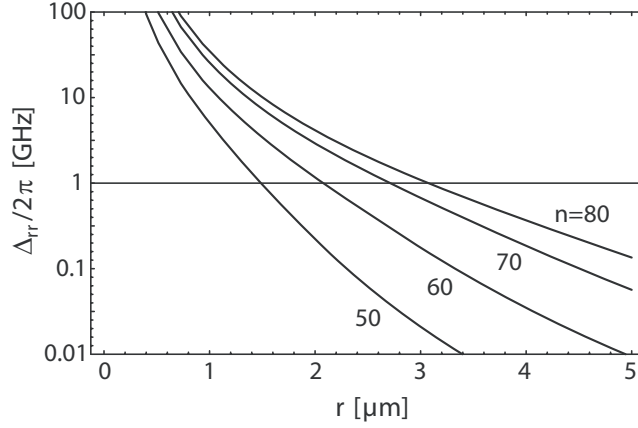


Figure 3.9. Interaction strength as a function of the interatomic distance for Rydberg states in cesium characterized by the principal quantum number n . The figure is reproduced from [63] by courtesy of Mark Saffman.

up to several hundred atoms.⁴

As illustrated in Fig. 3.9, the interaction strongly depends on n [60]. Indeed, μ_n scales as n^2 , so Γ_{rr} scales as n^4 , and δ scales as n^{-3} . For $\Gamma_{rr} \ll \delta$, (3.6) reduces to $\Delta_{rr} = 12\Gamma_{rr}^2/\delta$, which scales as n^{11} . In order to obtain a large energy shift, it is tempting to use states with very large principal numbers. However, to avoid collisions between the electrons of two neighboring Rydberg atoms, n cannot exceed a certain maximum value n_{max} . We can estimate n_{max} by demanding that r exceeds the average radius of the electron orbit, $r_e = \frac{1}{2}a_0(3n^2 - L(L+1))$ [64], by an order of magnitude. This imposes that

$$n_{max} \simeq \sqrt{\frac{2kr}{3a_0} + \frac{L(L+1)}{3}},$$

where k is defined by $r_e \leq kr$. With $r = 8 \mu\text{m}$ and $k = 1/10$, it follows that $n_{max} \approx 100$.

Balancing the ground- and excited-state polarizabilities

In order to couple qubits via the Rydberg-Rydberg interaction, it is necessary to make transitions to the Rydberg levels. However, in a red-detuned FORT, the ground and the Rydberg states have polarizabilities of opposite signs

⁴As we demonstrate later, $n = 70$ is sufficiently low to avoid collisions between electrons of neighboring Rydberg atoms. However, it would not be prudent to choose a much larger n , as more and more states interact and mix when n is increased, making it difficult to control the transition from the hyperfine ground states to the Rydberg states.

meaning that the Rydberg states experience a repulsive potential. This leads to heating and decoherence due to entanglement of the spin and motional states. A possible way to overcome this problem is to use a blue-detuned FORT at a trapping laser wavelength for which the ground- and excited-state polarizabilities are equal (and negative, hereby trapping atoms at intensity minima). This has the beneficial side effect of improving the coherence time for qubit storage (and to some extent the Rydberg state lifetime) [25].

Rydberg state lifetime

The Rydberg state lifetime must be taken into account, because Rydberg states must be populated in order to implement two-qubit logical operations. The radiative lifetime is strongly affected by background blackbody radiation, and in [25] it was estimated for a Rydberg state of ^{87}Rb to be greater than 0.1 ms at room temperature for $n \gtrsim 65$, see Fig. 3.10. This suggests a radiative line width Γ smaller than 10 kHz.

An additional decay mechanism of the Rydberg states is photoionization caused by the intense trapping light of the FORT. The photoionization cross section decreases with n .

In total, it is estimated in [25] that the Rydberg lifetime will exceed 100 μs for $n \gtrsim 80$.

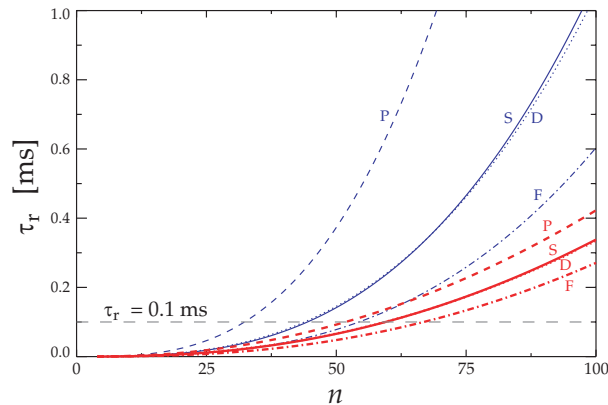


Figure 3.10. Radiative lifetime of the S , P , D and F states of rubidium as a function of the principal quantum number, n , for $T = 0$ K (blue lines) and $T = 300$ K (red lines). The figure is reproduced from [25] by courtesy of Mark Saffman.

3.5.2 The Rydberg phase gate

The underlying principle of the Rydberg phase gate, originally proposed in [23], is the entanglement of two atoms using the strong dipole-dipole in-

interaction of the Rydberg states. In principle, all levels shift when two atoms are brought sufficiently close to interact, but only the Rydberg levels shift significantly.

As will be clear in the following, the gate design depends on the ratio between the Rabi frequency and the interaction strength. Two distinct regimes exist corresponding to two different protocols, i.e., the limits of large Rabi frequency and large interaction. The large interaction strength limit is particularly favorable for gates between neighboring sites. The large Rabi frequency limit works for a longer range, since a small Rydberg-Rydberg interaction suffices for non-nearest neighbors to be coupled.

The Rydberg blockade gate

The protocol for the gate operation in the limit $|\Delta_{rr}| \gg |\Omega_R|$ is the following, cf. Fig. 3.11: (i) excite atom 1 from $|0\rangle \rightarrow |r\rangle$ with a π pulse, (ii) apply a 2π pulse resonant with the transition $|0\rangle \leftrightarrow |r\rangle$ to atom 2, and (iii) deexcite atom 1 from $|r\rangle \rightarrow |0\rangle$ with a π pulse. Note that Fig. 3.11 is a simplification; in reality the rotations between $|0\rangle$ and $|r\rangle$ take place via an intermediate level $|e\rangle$ such that the levels $|0\rangle$ and $|r\rangle$ merely constitute an effective two-level system (see below).

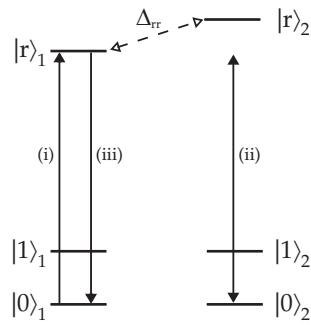


Figure 3.11. The controlled phase gate in the limit $|\Delta_{rr}| \gg |\Omega_R|$. The protocol is described in the text.

As Fig. 3.11 illustrates, if atom 1 is in state $|r\rangle$, the 2π pulse is shifted out of resonance due to the large Rydberg dipole-dipole interaction, whereas if atom 1 is in state $|1\rangle$ during (ii), the pulse applied to atom 2 is resonant. This conditional shift is responsible for the entanglement. As the population in $|r\rangle_1$ ‘blocks’ the excitation to $|r\rangle_2$, we refer to the Rydberg phase gate in this

limit as the Rydberg blockade gate. The gate has the following effect

$$\begin{aligned}
|00\rangle &\xrightarrow{i} -i|r0\rangle \xrightarrow{ii} -ie^{i\tilde{\phi}}|r0\rangle \xrightarrow{iii} -e^{i\tilde{\phi}}|00\rangle, \\
|01\rangle &\rightarrow -i|r1\rangle \rightarrow -i|r1\rangle \rightarrow -|01\rangle, \\
|10\rangle &\rightarrow |10\rangle \rightarrow -|10\rangle \rightarrow -|10\rangle, \\
|11\rangle &\rightarrow |11\rangle \rightarrow |11\rangle \rightarrow |11\rangle.
\end{aligned}$$

The minus signs for $|01\rangle$ and $|10\rangle$ arise from the fact that a resonant 2π pulse results in a phase shift of π . The unwanted phase shift $\tilde{\phi}$ is attributable to $|0\rangle_2$ not being completely off-resonant with $|r\rangle_2$ when $|r\rangle_1$ is occupied. The phase shift can be calculated as follows: when $|r\rangle_1$ is populated, the 2π pulse is detuned with $\Delta = -\Delta_{rr}$. Using an evolution operator similar to (3.2), the effect of a 2π pulse is $|0\rangle_2 \rightarrow e^{i\tilde{\phi}}|0\rangle_2$, where $\tilde{\phi} = \pi\Omega_R/2\Delta_{rr}$ and Ω_R is the Rabi frequency for atom 2. For Rabi frequencies and energy shifts on the order of MHz and 100 MHz, respectively, the phase shift is of order 10^{-2} .

The duration of the gate is $\Delta t = 2\pi/|\Omega_1| + 2\pi/|\Omega_2|$, where Ω_j is the Rabi frequency for atom j . Note that Ω_2 is limited by the above estimate for $\tilde{\phi}$. For Rabi frequencies of order MHz the duration is of order μs .

In addition to the error sources for single-qubit gates, mentioned in chapter 3.4.3, the fidelity for this two-qubit operation is also limited by effects arising from the use of Rydberg states [25]. Firstly, the Doppler shift due to the atomic motion is larger for excitations to Rydberg levels. Secondly, the finite lifetime of the Rydberg states is problematic because the Rydberg states are populated during the gate operation. So even though the lifetime of the Rydberg states is longer than that of the excited state $5P_{1/2}$, used for the single-qubit gates, the spontaneous emission rate is larger for the two-qubit gate, because $5P_{1/2}$ remains almost unpopulated during the single-qubit gates. Speculations about the necessity of populating the Rydberg states for a prolonged period of time have been rendered superfluous in [65], in which it is demonstrated that, for a two-qubit gate to create the one unit of entanglement required for the controlled phase gate, the integrated population of the Rydberg states during the gate operation is bounded below by $\int P_r^{total} > 2/|\Delta_{rr}|$, where P_r^{total} is the total population of the Rydberg states. The amount of spontaneous emission during the gate is then larger than $2\Gamma/|\Delta_{rr}|$, where Γ is the radiative linewidth of the Rydberg state. By way of example, for the values $\Gamma = 10$ kHz and $\Delta_{rr}/2\pi = 100$ MHz, the amount of spontaneous emission exceeds $2 \cdot 10^{-4}$. A third limitation is heating due to the transfer to Rydberg states, as was discussed in chapter 3.5.1. All effects combined, the estimated error is of order 10^{-3} [25].

The phase gate in the limit of large Rabi frequency

In the limit $|\Omega_R| \gg |\Delta_{rr}|$, the gate protocol is the following: (i) excite both atoms from $|0\rangle \rightarrow |r\rangle$ with a π pulse, (ii) wait for a time $\Delta t = \pi/\Delta_{rr}$, and (iii) deexcite both atoms from $|r\rangle \rightarrow |0\rangle$ with a π pulse. Since $|\Omega_R| \gg |\Delta_{rr}|$, the dipole-dipole interaction can be considered a small perturbation and resonant population transfer during (i) and (iii) is feasible. Switching to the interaction picture it is clear that only $|rr\rangle$ picks up a phase, namely π , during (ii). Therefore, all initial states except $|11\rangle$ are endowed with a phase shift of π at the end of the protocol and an entangling phase gate is obtained.

Note that the design of this gate gives rise to extra sources of error in addition to those discussed for the Rydberg blockade gate. The dependence, via Δ_{rr} , of the accumulated phase on the interatomic distance, threatens the reliability of the gate due to the atomic motion in the traps as opposed to the Rydberg blockade gate, which is insensitive to the exact value of the energy shift. Furthermore, for the $|00\rangle$ state the transition to $|rr\rangle$ is imperfect because of the (small) dipole-dipole shift leading to an error of $E \sim (\Delta_{rr}/\Omega_R)^2$ [25]. When populated, the state $|rr\rangle$ is subject to the dipole-dipole force and this leads to heating of the atoms. Accordingly, there is a non-zero probability that the internal and external degrees of freedom are entangled. This is not the case for the Rydberg blockade gate, since the doubly Rydberg-excited state is not populated during the gate, which also implies an additional advance since this allows n to exceed n_{max} . After considering these additional imperfections in the large Rabi frequency limit, it is preferable to instead employ the gate in the limit of large interaction strength whenever possible.

The cascade system

As previously noted the rotation between $|0\rangle$ and $|r\rangle$ takes place via an excited state $|e\rangle$ (see Fig. 3.12). It is possible to eliminate the intermediate level $|e\rangle$ adiabatically along similar lines as in the calculation for the lambda system in chapter 3.4.1. The resulting evolution matrix in the interaction picture is very similar to (3.2), the differences being that the global phase factor is instead $\exp[-i(|\Omega_1|^2 + |\Omega_2|^2)/(4(\Delta_1 - \Delta_2))]$, the Rabi frequency is $\Omega_R = \Omega_1\Omega_2/(\Delta_1 - \Delta_2)$, $\Delta' = \Delta + (|\Omega_1|^2 - |\Omega_2|^2)/2(\Delta_1 - \Delta_2)$ and the two-photon detuning Δ is defined in Fig. 3.12. Note that the Doppler shift due to atomic motion is minimized for counter-propagating beams.

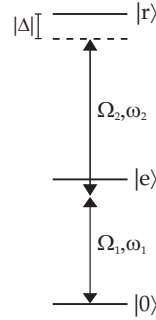


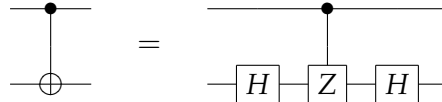
Figure 3.12. The cascade system for population transfer to the Rydberg level. The detuning is $\Delta = \Delta_1 + \Delta_2 = \omega_1 + \omega_2 - \omega_{r0}$.

Implementation of a CNOT gate

Both gate protocols described above result in a controlled phase gate, which up to a global phase factor of -1 is represented by the matrix

$$U = \begin{pmatrix} 1 & 0 & 0 & 0 \\ 0 & 1 & 0 & 0 \\ 0 & 0 & 1 & 0 \\ 0 & 0 & 0 & -1 \end{pmatrix}$$

in the basis $\{|00\rangle, |01\rangle, |10\rangle, |11\rangle\}$ (interaction picture). This is equivalent to a CZ gate, where $Z = \begin{pmatrix} 1 & 0 \\ 0 & -1 \end{pmatrix}$ is the Pauli Z matrix. Atoms 1 and 2 are the control and the target atoms, respectively. The CZ gate can be converted into a CNOT gate by applying single-qubit Hadamard gates to atom 2, as follows:



Thus, if atom 1 (represented by the top line) is in state $|0\rangle$ then $HH = I$ is applied to atom 2 (represented by the bottom line), whereas if atom 1 is in state $|1\rangle$ then $HZH = X$, where $X = \begin{pmatrix} 0 & 1 \\ 1 & 0 \end{pmatrix}$ is the Pauli X matrix, is applied to atom 2.

3.6 Experimental progress

Next, we review the experimental progress on NAQC with Rydberg blockade. The two main experimental groups working in this field are the group in Madison led by Mark Saffman and Thad G. Walker, and the group in Orsay led by Philippe Grangier. Saffman and Walker employ the setup and the gate proposals of this chapter. Grangier makes use of the same choice of

qubit basis states and also performs single-qubit gates using two-photon Raman transitions. However, the trap design differs. At present, Saffman and Walker are closer to demonstrating universal quantum computation. However, the experimental setup of Grangier provides an interesting alternative.

3.6.1 Experiments by Grangier

The experimental progress of the group of Grangier has recently been reviewed in [66]. As in the experiments of Saffman and Walker, the trap is a FORT, but it is much more focused with a size of about $1 \mu\text{m}$. This ensures single-atom trapping based on a collisional blockade effect [67].

In [68] Grangier et al. demonstrate initialization, read out, and manipulation of single qubits. Initialization to $|0\rangle$ by optical pumping is obtained with 85 % efficiency in $200 \mu\text{s}$. State-selective measurements limited solely by quantum projection noise are carried out by using a laser resonant with the $|5S_{1/2}, F = 2, m_F = 2\rangle \leftrightarrow |5P_{3/2}, F' = 3, m_{F'=3}\rangle$ cycling transition. This pushes atoms initially in state $|1\rangle$ out of the trap, and any atoms subsequently observed in the trap were therefore initially in $|0\rangle$. Single-qubit transitions via $5P_{1/2}$ are driven using two tightly focused Raman lasers. The optical dipole trap forms one of the beams, providing a Rabi frequency of $2\pi \cdot 6.7 \text{ MHz}$. The Rabi oscillations are damped due to intensity noise and atomic motion.

Note that the qubit states experience slightly different trapping potentials giving rise to a position dependent transition frequency. Combined with atomic motion in the trap, this leads to a qubit dephasing time of $630 \mu\text{s}$. However, applying the spin-echo technique, a revival of the oscillations after 40 ms is observed, thus improving the coherence time dramatically [68].

At present, Rabi oscillations between a qubit level and a Rydberg level are being attempted. When Rydberg blockade, as described in [61], is actually implemented, the experimental setup is interesting because the group has already demonstrated that any pair of atoms can be brought sufficiently close to interact. This involves transferring atoms between traps and transporting atoms over several tens of micrometers. In addition, due to very strong laser focusing, high Rabi frequencies are expected.

3.6.2 Experiments by Saffman and Walker

At the time of writing, the group of Saffman and Walker has already observed Rydberg blockade between two atoms [69].

In 2005, multiple atom two-photon Rabi flopping between the qubit states via $5P_{3/2}$ was observed at a rate of $2\pi \cdot 1.36 \text{ MHz}$. The cross talk between two neighboring traps was negligible, demonstrating that individual addressing is possible [70]. The measured decoherence time was $870 \mu\text{s}$, thus approximately 5000 times longer than the duration of a $\pi/2$ pulse.

Subsequently, in 2007, Rabi oscillations were observed between the ground

level and the $43D_{5/2}$ Rydberg level, via $5P_{3/2}$ and at a Rabi frequency of $2\pi \cdot 0.5$ MHz with laser line widths of only a few hundred Hz [71]. Rydberg interaction effects were observed in the sense that, when more than one atom was present in a trap, the Rabi oscillations were strongly suppressed. This is compared to the case of Rabi oscillations between ground levels, where high fidelity rotations were observed with as many as 10 atoms in a trap. The observed suppression in the Rydberg case was due to dephasing caused by the existence of linear superpositions of two-atom $43D_{5/2}$ states with small dipole-dipole interactions. This leads to a value of only $2\pi \cdot 0.5$ MHz of the effective blockade shift (see chapter 3.5.1), which is comparable to the Rabi frequency. The conclusion was that the interaction was too weak for an effective blockade, but strong enough to lead to dephasing.

These observations motivated going to a higher Rydberg level to obtain a blockade shift strong enough to block excitation of a second atom located in a neighboring trap, a prerequisite for implementing the Rydberg blockade phase gate. Accordingly, in 2008, coupling to the $79D_{5/2}$ level made possible the Rydberg blockade between two individual atoms [69]. Previous experiments had only been able to demonstrate suppression of excitation due to Rydberg interactions for a macroscopic sample [72–78]. In their experiment Saffman and Walker trapped single neutral atoms separated by $11 \mu\text{m}$, which is large compared to the $1 \mu\text{m}$ characteristic wavelength of the lasers used for internal state manipulation. This choice of Rydberg level and trap separation ensures a regime in which the atomic separation is small enough to induce a strong interaction, yet large enough to ensure individual controllability. Thus, with a waist of the manipulating beams of $10 \mu\text{m}$, it was experimentally demonstrated that crosstalk was limited, while the blockade shift was large enough to lower the probability of double excitation from $80\%^5$ to approximately 30%, clearly demonstrating Rydberg blockade (see Fig. 3.13). A theoretical evaluation of the effective blockade strength predicts a double excitation probability of 7%. However, the observed 30% can be explained partly by the lack of perfect Rydberg excitation of the control atom. Minor improvements in laser addressing are expected to facilitate an atomic separation of $7 \mu\text{m}$, thereby lowering the double excitation probability to about 1% [69].

Combining the Rydberg blockade with single-atom rotations allows for the implementation of a CNOT gate. Improving the fidelity of all operations as well as increasing the qubit decoherence time, are natural next steps. Here, our proposals for the application of composite pulses and encoding

⁵The lack of perfect Rydberg excitation in the case of no applied π pulses is mainly due to Doppler broadening, imperfect optical pumping, and imperfect detection efficiency. However, attempts are currently underway to implement composite pulses in order to improve the fidelity of the Rabi oscillations to the Rydberg levels (note that a composite pulse system for single-qubit rotations between the ground hyperfine states has already been constructed [57]).

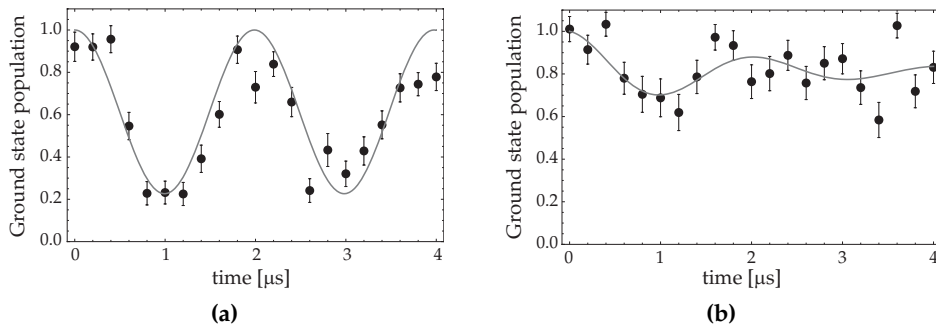


Figure 3.13. Rabi oscillations for the target atom when (a) no π pulses are applied to the control atom, (b) π pulses are applied to the control atom. The figure is reproduced from [69] by courtesy of Mark Saffman.

into decoherence-free subspaces (see chapter 4) will be particularly relevant. Ultimately, to obtain full scalability, the experimental goal is collective encoding (see chapter 5) in, for instance, Holmium atoms, which might lead to a 1000-qubit quantum processor [79].

Decoherence-free subspaces

Decoherence is a major obstacle to reliable quantum computation. Different schemes have been designed to circumvent the effect of quantum errors, such as quantum error correction procedures, in which quantum information is actively protected through the application of encoding and recovery operations. Another approach, considered as ‘passive’, consists of encoding information in subspaces which are immune to errors, the so-called decoherence-free subspaces (DFS’s) [42,80]. The existence of such subspaces relies on symmetry properties of the interaction between the system and its environment. The explicit construction of a DFS has already been achieved for certain collective [43,81], non-collective [82], and arbitrary [83] error processes, and even experimentally implemented in quantum optics [84], trapped-ion [85], neutral-atom [86], and NMR [87] setups. Moreover, universal computation within these DFS’s has been shown to be possible theoretically [88–91].

In this chapter, based on our papers [III] and [IV], we identify a DFS immune to collective dephasing for the NAQC implementation considered in this thesis. We demonstrate a universal set of gates, by means of which computation may be carried out without leaving the DFS. Subsequently, we provide numerical simulations for the fidelity of the gates in the presence of time-dependent phase errors and discuss their performance and practical feasibility.

4.1 Information storage in a DFS

The type of errors we consider in the following are random phase errors which affect different qubits according to the same error Hamiltonian:

$$E(t) = \hbar \begin{pmatrix} \epsilon_0(t) & 0 \\ 0 & \epsilon_1(t) \end{pmatrix}. \quad (4.1)$$

This kind of error model, in our physical setting, describes the effect of external fields that induce uncontrolled and unwanted energy shifts. If no action is taken, the unknown differential phase shift induced by $E(t)$ rapidly leads to a complete loss of coherence of the qubit states.

A simple two-dimensional DFS protecting against collective dephasing can be straightforwardly identified in the Hilbert space of a two-qubit system:

$$\begin{aligned} |0\rangle_{DFS} &= |01\rangle, \\ |1\rangle_{DFS} &= |10\rangle. \end{aligned} \quad (4.2)$$

By choosing (4.2) as the two basis states, the logical qubit is protected against collective phase errors, as $|0\rangle_{DFS}$ and $|1\rangle_{DFS}$ are affected equally by $E(t)$, i.e., both states obtain a phase of $\exp(-i \int_0^t (\epsilon_0(\tau) + \epsilon_1(\tau)) d\tau)$. Consequently, the subspace they span is invariant to errors described by (4.1).

In order to protect a qubit of information initially stored in the state $|\psi\rangle = c_0|0\rangle + c_1|1\rangle$, we thus need to recast it into the form $|\psi\rangle_{DFS} = c_0|0\rangle_{DFS} + c_1|1\rangle_{DFS}$, which can be done simply by adding an auxiliary qubit initially prepared in the state $|1\rangle$ and performing a CNOT gate:

$$|\psi\rangle|1\rangle = c_0|01\rangle + c_1|11\rangle \xrightarrow{\text{CNOT}} c_0|01\rangle + c_1|10\rangle = |\psi\rangle_{DFS}.$$

To read out the encoded information, the CNOT gate is applied again to $|\psi\rangle_{DFS}$, which returns the state to $|\psi\rangle|1\rangle$. Note that an N -logical-qubit memory can be constructed from N protected cells, which requires $2N$ physical qubits.

4.2 Information processing in the DFS

In order to safely process the information stored in the DFS, new gate implementations are needed, since the gates discussed in the previous chapters cause system deviations from the DFS during computations and are vulnerable to errors. In the following, we review two processes which allow the system to remain in the DFS at all times and subsequently demonstrate how combining these leads to protected universal computation.

4.2.1 A DFS phase gate

The first process we consider is a phase gate which leaves the system in the DFS. If a laser, as illustrated in Fig. 4.1, is applied to the first atom for a time $t_p = n2\pi/\Omega_{R,p}$, where $\Omega_{R,p} = \sqrt{|\Omega_p|^2 + \Delta_p^2}$ and n is a positive integer, the state $|10\rangle$ picks up the phase $e^{i\phi}$, where $\phi = n\pi(1 + \Delta_p/\Omega_{R,p})$, while the state $|01\rangle$ is left unchanged. In the DFS basis this transformation is represented, in the interaction picture, by

$$P(\phi) = \begin{pmatrix} 1 & 0 \\ 0 & e^{i\phi} \end{pmatrix}. \quad (4.3)$$

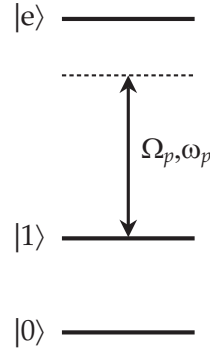


Figure 4.1. Level scheme for the DFS phase gate. A laser with frequency ω_p and Rabi frequency Ω_p is applied to the transition $|1\rangle \leftrightarrow |e\rangle$, where $|e\rangle$ denotes an excited state, with a detuning $\Delta_p = \omega_p - \omega_{e1}$.

By a proper choice of physical parameters, any desired phase can be implemented in this way. Choosing $|\Delta_p| \gg |\Omega_p|$ ensures that the excited state $|e\rangle$ remains essentially unpopulated during the process, and hence the phase gate allows the system to remain in the DFS.

4.2.2 Rotations in the DFS

The second process we consider allows us to perform rotations between the DFS basis states without leaving the DFS. It is not at all straightforward to identify such a process. However, as we shall now demonstrate, exploiting the dipole-dipole interaction of Rydberg states in a fourth-order Raman-like process renders it possible.

Consider two laser fields with Rabi frequencies Ω_0 and Ω_1 , respectively, as defined in Fig. 4.2a. The frequencies ω_0 and ω_1 are slightly detuned from the transitions $|i\rangle \leftrightarrow |r\rangle$, where $i = 0, 1$, and $|r\rangle$ is a Rydberg state of the atom. Applying the two laser fields to a pair of atoms couples the DFS basis states by a four-photon transition. Because of the dipole-dipole interaction of Rydberg atoms (chapter 3.5.1), the energy of the doubly Rydberg-excited state $|rr\rangle$ is shifted with $\hbar\Delta_{rr}$ (with respect to the non-perturbed case). Hence, as for the Rydberg blockade gate, only one atom at a time will be excited to its Rydberg level. Therefore, only the two paths connecting $|0\rangle_{DFS}$ and $|1\rangle_{DFS}$ via singly-Rydberg-excited states contribute to the coupling (see Fig. 4.2b).

Assuming $|\Omega_0|, |\Omega_1| \ll |\Delta|, |\Delta'|, |\Delta - \Delta'|, |\Delta_{rr}|$, one can extract the effective dynamics of the subspace $\{|00\rangle, |01\rangle, |10\rangle, |11\rangle\}$ through a perturbative approach (see Appendix C), which yields the evolution operator, expressed

in the interaction picture,

$$U_{eff}(t, \Omega_0, \Omega_1, \Delta, \Delta', \Delta_{rr}) = e^{-i(\Delta_0 - \Delta')t} \begin{pmatrix} e^{-i(\Delta_{00} - \Delta_0)t} & 0 & 0 & 0 \\ 0 & \cos\left(\frac{\Omega_R t}{2}\right) & i \sin\left(\frac{\Omega_R t}{2}\right) & 0 \\ 0 & i \sin\left(\frac{\Omega_R t}{2}\right) & \cos\left(\frac{\Omega_R t}{2}\right) & 0 \\ 0 & 0 & 0 & e^{-i(\Delta_{11} - \Delta_0)t} \end{pmatrix}, \quad (4.4)$$

where

$$\begin{aligned} \Omega_R &= \frac{|\Omega_0 \Omega_1|^2}{8} \frac{\Delta_{rr} (\Delta' - 2\Delta)}{(\Delta_{rr} + \Delta' - 2\Delta) \Delta^2 (\Delta' - \Delta)^2}, \\ \Delta_0 &= \frac{|\Omega_0|^2}{4\Delta} + \frac{|\Omega_1|^2}{4(\Delta - \Delta')} \\ &\quad - \frac{1}{16} \left(\frac{|\Omega_0|^4}{\Delta^3} + \frac{|\Omega_1|^4}{(\Delta - \Delta')^3} + \frac{|\Omega_0 \Omega_1|^2 (2\Delta_{rr} + \Delta' - 2\Delta) (2\Delta - \Delta')}{(\Delta_{rr} + \Delta' - 2\Delta) \Delta^2 (\Delta' - \Delta)^2} \right), \\ \Delta_{00} &= \frac{|\Omega_0|^2}{2\Delta} \left[1 + \frac{1}{2\Delta} \left(\frac{|\Omega_1|^2}{2\Delta'} - \frac{|\Omega_0|^2 (\Delta_{rr} - \Delta)}{\Delta (\Delta_{rr} - 2\Delta)} \right) \right], \\ \Delta_{11} &= \frac{|\Omega_1|^2}{2(\Delta - \Delta')} \left[1 + \frac{1}{2(\Delta' - \Delta)} \left(\frac{|\Omega_0|^2}{2\Delta'} + \frac{|\Omega_1|^2 (\Delta_{rr} + \Delta' - \Delta)}{(\Delta - \Delta') (\Delta_{rr} + 2\Delta' - 2\Delta)} \right) \right]. \end{aligned} \quad (4.5)$$

Note that if $\Delta_{rr} = 0$ the logical-qubit states are not coupled. This is due to the fact that, if the Rydberg-Rydberg interaction is absent, the paths connecting $|0\rangle_{DFS}$ and $|1\rangle_{DFS}$ via $|rr\rangle$ will interfere destructively with the two paths displayed in Fig. 4.2b leading to a decoupling of the DFS levels.

If the two atoms involved are initially prepared in a DFS state, that is a superposition of $|01\rangle$ and $|10\rangle$, the transformation U_{eff} , with the associated gate

$$R(\theta) \propto \begin{pmatrix} \cos(\theta) & i \sin(\theta) \\ i \sin(\theta) & \cos(\theta) \end{pmatrix}, \quad \theta = \frac{\Omega_R t}{2}, \quad (4.6)$$

allows the system to remain in the DFS at all times. This makes it possible to perform rotations in the DFS, while constantly protecting against phase errors. However, neither this gate nor the phase gate are completely phase-error free, even though they do not make the system leave the DFS during computations. Thus, the detunings Δ , Δ' , and Δ_{rr} are shifted slightly in the presence of phase errors hereby affecting P and U_{eff} . However, for large detunings the effect of reasonably small errors is expected to be insignificant. A claim which we later substantiate with numerical simulations.

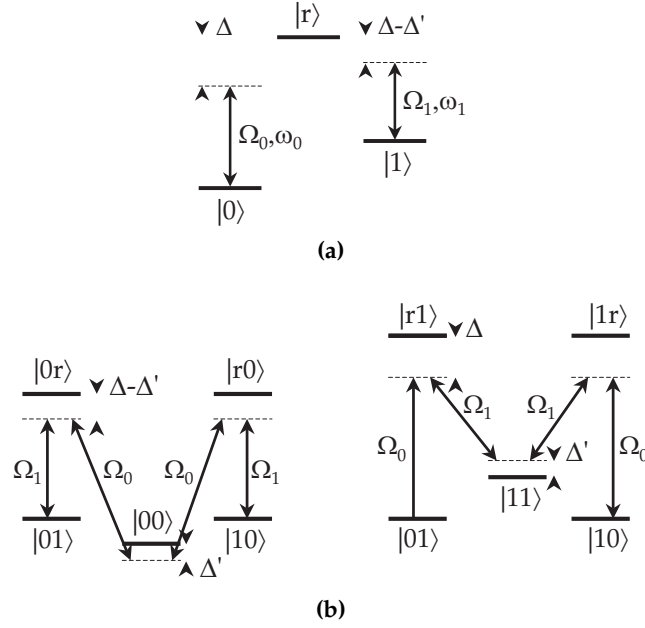


Figure 4.2. (a) Level scheme and laser couplings for one atom. The detunings are denoted $\Delta = \omega_0 - \omega_{r0}$ and $\Delta' = \omega_0 - \omega_1 - \omega_{10}$. The detuning of the laser with frequency ω_1 thus equals $\Delta - \Delta'$. (b) The two M-shaped paths coupling the DFS basis states.

Other than implementing DFS rotations, we note that U_{eff} can endow a non-DFS state, for instance $|00\rangle$, with a phase factor which can be controlled via the Rabi frequencies and detunings. We exploit this fact in the following for the construction of a two-logical-qubit phase gate.

4.2.3 A universal set of DFS gates

Single-logical-qubit gates for the DFS are readily obtained by combining the operators (4.3) and (4.6) according to

$$T_{DFS} \equiv \begin{pmatrix} 1 & 0 \\ 0 & e^{i\pi/4} \end{pmatrix} \propto P\left(\frac{\pi}{4}\right),$$

$$H_{DFS} \equiv \frac{1}{\sqrt{2}} \begin{pmatrix} 1 & 1 \\ 1 & -1 \end{pmatrix} \propto P\left(\frac{3\pi}{2}\right) R\left(\frac{\pi}{4}\right) P\left(\frac{3\pi}{2}\right).$$

Identifying a two-logical-qubit gate is somewhat more complicated. First, consider two logical qubits consisting of the physical qubits (1,2) and (3,4). Information is naturally encoded on the decoherence free (code) subspace \mathcal{C} ,

spanned by

$$\begin{aligned} |00\rangle_{DFS} &\equiv |0101\rangle, \\ |01\rangle_{DFS} &\equiv |0110\rangle, \\ |10\rangle_{DFS} &\equiv |1001\rangle, \\ |11\rangle_{DFS} &\equiv |1010\rangle. \end{aligned}$$

Adding to this four-dimensional DFS the vectors $|\alpha\rangle_{DFS} \equiv |0011\rangle$ and $|\beta\rangle_{DFS} \equiv |1100\rangle$ extends it to a six-dimensional DFS, \mathcal{D} . Since all vectors in \mathcal{D} contain the same number of 0's and 1's they are affected in the same way by phase errors. However, for the states in \mathcal{C} , the logical qubits (1,2) and (3,4) are individually protected, whereas for $|\alpha\rangle_{DFS}$ and $|\beta\rangle_{DFS}$ only the pair of logical qubits is protected from phase errors.

In order to perform a two-qubit gate on the information initially stored in \mathcal{C} , it could be expected that a four-atom process would be involved. However, it turns out that it suffices to apply the transformation U_{eff} to atoms 1 and 3, as suggested in Fig. 4.3:

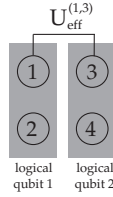


Figure 4.3. The U_{eff} gate acting on atoms 1 and 3.

By (4.4), the states in \mathcal{C} are transformed according to

$$\begin{aligned} |00\rangle_{DFS} &\rightarrow e^{-i(\Delta_{00}-\Delta')t} |00\rangle_{DFS}, \\ |01\rangle_{DFS} &\rightarrow e^{-i(\Delta_0-\Delta')t} (\cos(\Omega_R t/2) |01\rangle_{DFS} + i \sin(\Omega_R t/2) |\beta\rangle_{DFS}), \\ |10\rangle_{DFS} &\rightarrow e^{-i(\Delta_0-\Delta')t} (\cos(\Omega_R t/2) |10\rangle_{DFS} + i \sin(\Omega_R t/2) |\alpha\rangle_{DFS}), \\ |11\rangle_{DFS} &\rightarrow e^{-i(\Delta_{11}-\Delta')t} |11\rangle_{DFS}. \end{aligned}$$

The system evidently leaves the code space \mathcal{C} . However, since it remains in \mathcal{D} at all times, information is protected from phase errors.

If the parameters are adjusted such that

$$t = \frac{4\pi}{\Omega_R}, \quad \frac{\Delta_{00} - \Delta_0}{\Omega_R} = \frac{n}{2}, \quad \frac{\Delta_{11} - \Delta_0}{\Omega_R} = \frac{1}{4} + \frac{m}{2},$$

where n, m are integers, $U_{eff}^{(1,3)}$ implements the transformation

$$\begin{aligned} |00\rangle_{DFS} &\rightarrow e^{-i(\Delta_0 - \Delta')t} |00\rangle_{DFS}, \\ |01\rangle_{DFS} &\rightarrow e^{-i(\Delta_0 - \Delta')t} |01\rangle_{DFS}, \\ |10\rangle_{DFS} &\rightarrow e^{-i(\Delta_0 - \Delta')t} |10\rangle_{DFS}, \\ |11\rangle_{DFS} &\rightarrow -e^{-i(\Delta_0 - \Delta')t} |11\rangle_{DFS}, \end{aligned}$$

corresponding to a controlled phase gate $U_{phase,DFS}$ on the subspace \mathcal{C} . A CNOT gate is then simply obtained from

$$\text{CNOT}_{DFS} = (I \otimes H_{DFS}) \times U_{phase,DFS} \times (I \otimes H_{DFS}),$$

as suggested in Fig. 4.4. This completes our set of protected universal quantum gates.

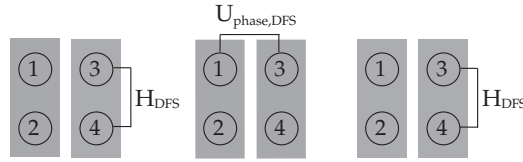


Figure 4.4. Scheme for the CNOT_{DFS} gate.

4.3 Assessment of the DFS gates

As already pointed out, even though the system remains in the DFS during computations, our gate proposals are not completely error-free since the detunings are modified by the error Hamiltonian (4.1). In addition, spontaneous emission from the states $|e\rangle$ and $|r\rangle$ is a limitation to the fidelity. In the following, we provide a numerical estimate of the performance of the presented DFS gates in the presence of random phase errors and spontaneous emission. To obtain a benchmark for the obtained fidelities, we also compare the ‘restricted’ gates to a set of ‘unrestricted’ gates which allow the system to leave the DFS during computations. Finally, we discuss the practical interest and feasibility of our proposal.

4.3.1 Principles of numerical simulations

Prior to presenting the results, we describe our numerical approach. For each of the four atoms in two logical qubits, we include the four states $|0\rangle$, $|1\rangle$, $|e\rangle$ (used for the implementation of the phase gate) and $|r\rangle$. It is advantageous to propagate this large system in time steps dt small enough to

assume H , a 256×256 matrix, constant (in a suitable rotating frame), such that the evolution is simply obtained from

$$|\psi(t + dt)\rangle = \exp\left(\frac{-iHdt}{\hbar}\right) |\psi(t)\rangle.$$

Subsequently, the dynamics is restricted to the logical-two-qubit subspace \mathcal{C} and a transformation to the interaction picture is performed.

Simulation of random phase errors

For our simulations, we assume phase errors on $|1\rangle$, $|e\rangle$ and $|r\rangle$ and model their effect by the single-atom Hamiltonian

$$E(t) = \hbar(\epsilon_1(t) |1\rangle \langle 1| + \epsilon_e(t) |e\rangle \langle e| + \epsilon_r(t) |r\rangle \langle r|).$$

Moreover, we suppose that phase errors can be described by an Ornstein-Uhlenbeck process for which

$$\epsilon(t + dt) = \epsilon(t) - \frac{1}{\tau}\epsilon(t)dt + \sqrt{c}G(t)\sqrt{dt},$$

where τ is the relaxation time, c is the diffusion constant and $G(t)$ is the unit Gaussian variable [92]. The Ornstein-Uhlenbeck process is characterized by the correlation function

$$\langle \epsilon(t)\epsilon(t') \rangle = \frac{\tau c}{2} e^{-|t-t'|/\tau}$$

in steady state, demonstrating that $\epsilon(t)$ and $\epsilon(t')$ will be either highly correlated or effectively uncorrelated depending on the ratio $(t - t')/\tau$.

This Gaussian process admits a stationary probability distribution and it can be shown that for initial condition $\epsilon(t_0) = \epsilon_0$, the mean value decreases as $\langle \epsilon(t) \rangle = \epsilon_0 e^{-(t-t_0)/\tau}$ with a long-term variance $\sigma^2 = \tau c/2$ [92], which leads to the update formula used for the generation of the steady state random phase errors

$$\epsilon(t + \Delta t) = \epsilon(t)e^{-\Delta t/\tau} + \sqrt{\frac{\tau c}{2}}G(t)$$

for small time steps Δt . Note that since we assume the system is in a steady state, the initial value is obtained from $\epsilon(t = 0) = G(t)$.

We assume that the errors for the various levels are correlated, which seems reasonable for the background magnetic field perturbations. Thus, $\epsilon_1(t)$ is generated using the approach described above while $\epsilon_e(t)$ and $\epsilon_r(t)$ are found from $\epsilon_e(t) = \alpha_e \epsilon_1(t)$ and $\epsilon_r(t) = \alpha_r \epsilon_1(t)$.

Spontaneous emission

Spontaneous emission can be taken into account by solving the master equation. Alternatively, the Monte Carlo wave function approach can be employed. Since the latter approach is particularly easy to implement for our physical system, we shall make use of it for our simulations. With this method we can account for spontaneous emission by adding the term

$$-i\hbar\frac{\Gamma_e}{2}|e\rangle\langle e| - i\hbar\frac{\Gamma_r}{2}|r\rangle\langle r|$$

to the single-atom Hamiltonians, assuming that lost population inevitably leads to fidelity loss, see Appendix D. As discussed in chapter 3.5.1, the radiative linewidth of the Rydberg state, Γ_r , is estimated to be smaller than 10 kHz for $n > 65$. Note that for our simulations, we assume that $\Gamma_e = \Gamma_r$.

Fidelity measure

An appropriate fidelity measure for the performance of the gates in the presence of stochastic errors is calculated in the following way. For a $N \times N$ density matrix, ρ , the time evolution is given by $\rho \rightarrow U\rho U^\dagger$. Representing the matrix ρ as a vector $\vec{\rho}$ this can be rewritten such that

$$\vec{\rho} \xrightarrow{U} M\vec{\rho},$$

with M being an $N^2 \times N^2$ matrix. To each instance of $\epsilon_1(t)$ (and correspondingly $\epsilon_e(t)$ and $\epsilon_r(t)$) corresponds a certain M . Denoting by $\vec{\rho}_i$ the vector with 1 on the i th place, such that the only nonzero element in ρ_i is $\rho_{i,(\text{mod}(i,N), \lfloor i/N \rfloor + 1)}$, and by ρ'_i the matrix $\rho'_i = U\rho_i U^\dagger$, M is obtained from

$$M = \begin{pmatrix} \rho'_{1,(1,1)} & \rho'_{2,(1,1)} & \cdots \\ \rho'_{1,(2,1)} & \rho'_{2,(2,1)} & \cdots \\ \vdots & \vdots & \ddots \end{pmatrix}.$$

In order to obtain an average over the various phase error configurations, we can now simply average over the corresponding M 's and subsequently calculate the fidelity from

$$F(|\psi\rangle) = \vec{\rho}_{ideal}^\dagger M_{av} \vec{\rho},$$

where $\rho_{ideal} = U_{ideal}\rho U_{ideal}^\dagger$, M_{av} denotes the average over M , and $\rho = |\psi\rangle\langle\psi|$. In practice, we evaluate F for a large number of pure states $|\psi\rangle$, and in the figures we present the minimum value of F over these input states.

Optimization of parameters

As previously demonstrated, the various universal gates can be obtained by combination of the gates $P(\phi)$ and $U_{eff} = (t, \Omega_0, \Omega_1, \Delta, \Delta', \Delta_{rr})$. Accordingly, it is necessary to perform these gates with high precision.

The expression obtained for $P(\phi)$ is exact. This implies that, in the absence of errors and spontaneous emission, if we adjust the parameters t_p , Ω_p and Δ_p such that

$$\phi = n\pi(1 + \Delta_p / \sqrt{|\Omega_p|^2 + |\Delta_p|^2})$$

is the desired phase factor, we exactly obtain the expected gate $P(\phi)$.

On the contrary, the expression obtained for U_{eff} is only perturbative. This implies that if the physical parameters t , Ω_0 , Ω_1 , Δ , Δ' , and Δ_{rr} are chosen such that the effective parameters of (4.5) take the desired values (either to implement a conditional phase gate or an $R(\theta)$ gate), the exponential of the full Hamiltonian will even in the ideal case differ slightly from the desired gate.

Before dealing with errors and spontaneous emission, we therefore refine the parameters by a numerical search in the neighborhood of our first guess provided by the analytical, perturbative approach.¹ Once we have a faithful gate in the ideal case, we retain the set parameters and include the new terms discussed above in the Hamiltonian in order to run our simulations. However, performing the gate optimization with respect to five parameters (Ω_0 , Ω_1 , Δ , Δ' , and t) is an inherently difficult computational task since the relations in (4.5) are highly nonlinear in the physical detunings and Rabi frequencies. Accordingly, there may well exist other sets of parameters for which the performance of the gates is more impressive.

4.3.2 Performance of the DFS gates

Figure 4.5 shows the results of our numerical simulations. The fidelities of various gates are plotted as a function of $\tau c/2$, which corresponds to the variance of the detuning due to the perturbation.

In Fig. 4.5a spontaneous emission is neglected, while it is taken into account in Fig. 4.5b. As is evident, spontaneous emission severely limits the fidelity. The phase gate, T_{DFS} , is almost unaffected by spontaneous emission, since the excited state remains effectively unpopulated. However, with a gate duration on the order of 10^3 larger than the phase gate duration and smaller detunings to the upper levels, the effect of spontaneous emission is considerable for the controlled phase gate, $U_{phase,DFS}$, and hereby the $CNOT_{DFS}$ gate.

¹Note that for the optimization it is favorable to optimize the mean rather than the worst case fidelity, since our formula of chapter 2 allows for fast computation of the fidelity.

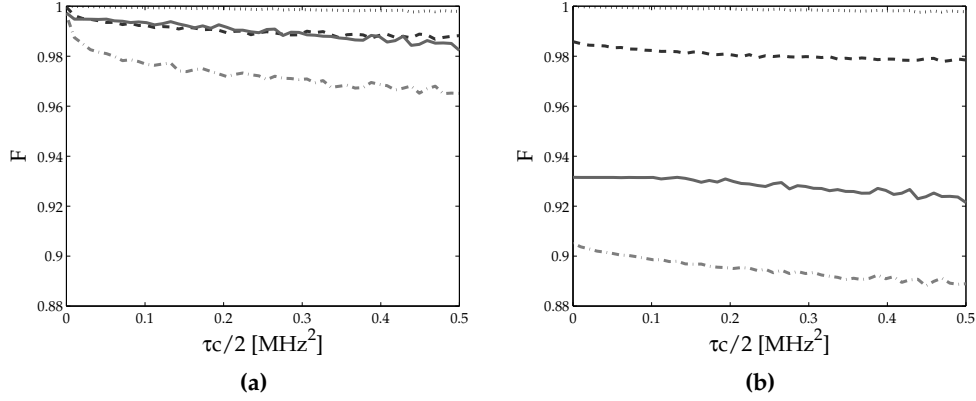


Figure 4.5. Performance of the universal set of DFS gates in the (a) absence and (b) presence of spontaneous emission. The various lines corresponds to T_{DFS} (dotted), H_{DFS} (dashed), $U_{phase,DFS}$ (solid) and $cNOT_{DFS}$ (dash-dotted). Parameters used for our simulations are as follows. P gate: $\Omega_p/2\pi = 5$ MHz, $\Delta_p/2\pi \approx -49.81$ MHz and $t = 1$ μ s for $P(\pi/4)$. $R(\pi/4)$ gate: $\Omega_0/2\pi \approx 3.91$ MHz, $\Omega_1/2\pi \approx 1.97$ MHz, $\Delta/2\pi \approx 60.34$ MHz, $\Delta'/2\pi \approx 30.70$ MHz, $\Delta_{rr}/2\pi = 100$ MHz and $t \approx 120.20$ μ s. $U_{phase,DFS}$ gate: $\Omega_0/2\pi \approx 3.93$ MHz, $\Omega_1/2\pi \approx 1.96$ MHz, $\Delta/2\pi \approx 60.48$ MHz, $\Delta'/2\pi \approx 30.05$ MHz, $\Delta_{rr}/2\pi = 100$ MHz and $t \approx 938.62$ μ s. For the generation of random phase errors the parameters are $\tau = 1$ μ s and $\alpha_e = \alpha_r = 1.5$ and for the inclusion of spontaneous emission $\Gamma_e = \Gamma_r = 5$ kHz.

It is possible to establish a simple criterion on the various physical parameters involved in order to minimize both Rydberg population and the effect of spontaneous emission. Defining $\Omega_s = \sqrt{|\Omega_0\Omega_1|}$ and $\Delta_s = \sqrt{|\Delta_0\Delta_1|} = \sqrt{|\Delta(\Delta - \Delta')|}$, the average Rydberg population is approximately given by $P_r \simeq \frac{1}{2} \frac{\Omega_s^2}{\Omega_s^2 + \Delta_s^2}$, and the average number of photons emitted during the controlled phase gate by $N_{ph} = \Gamma_r \cdot \frac{4\pi}{\Omega_R} \cdot P_r \simeq \frac{4\pi\Gamma_r\Delta_s^3}{\Omega_s^2(\Omega_s^2 + \Delta_s^2)}$, where Γ_r is the radiative linewidth of the Rydberg state. Demanding that $P_r \ll 1$ imposes that

$$\Omega_s/\Delta_s \ll 1, \quad (4.7)$$

and correspondingly, the requirement $N_{ph} \ll 1$ implies that

$$\sqrt{\frac{4\pi\Gamma_r}{\Delta_s}} \ll \frac{\Omega_s}{\Delta_s}. \quad (4.8)$$

For the parameters of Fig. 4.5, $\Omega_s/\Delta_s \approx 0.07$, which is not significantly lower than the right-hand side of (4.7). The left-hand side of (4.8) approximately equals 0.02. Increasing Δ_s in order to decrease Ω_s/Δ_s , increases the left-hand side of (4.8) relative to the right-hand side, and effects of spontaneous emission are thus seemingly unavoidable.

Note that as discussed in chapter 3.5.2 transitions to Rydberg states are implemented by going off-resonantly via an excited state, for instance $|P_{1/2}\rangle$. This worsens the effect of spontaneous emission, as the R and $U_{\text{phase,DFS}}$ gates are accordingly quite slow and the radiative linewidth for the $|P_{1/2}\rangle$ state is quite large ($\Gamma_{5P_{1/2}} = 5.7$ MHz). It is thus necessary to be strongly detuned from the excited level, but since this reduces the coupling to the Rydberg levels, the intensity of the Raman beams should be increased at the same time.

A further source of decoherence for the experimental setup discussed throughout this thesis is the motion of atoms in the traps. As the interatomic distance r varies so does the dipole-dipole interaction, which scales as $1/r^3$. Based on the estimates discussed in chapter 3.4.6, a variation of 20% for the value of Δ_{rr} is expected. We performed a numerical simulation assuming that Δ_{rr} is harmonically varying, which demonstrated a dramatic reduction of the fidelity for realistic parameters. Atomic motion in the traps thus poses a serious limitation for the gates. To improve the performance of the gates, the atoms may be cooled further, Δ_{rr} may be increased or the distance between the traps could be increased, which would, however, reduce Δ_{rr} .

4.3.3 Comparison with unrestricted gates

In order to assess the performance of our universal set of DFS gates, we compare them to a universal set of so-called unrestricted gates, which allow the system to leave the DFS during computations.

If we remove the restriction that the system should remain in the DFS at all times, we can construct DFS gates by making use of the gates presented in chapter 3. Thus

$$\begin{aligned} H_{DFS} &= \text{CNOT}_{1,2} \times (H \otimes I) \times \text{CNOT}_{1,2}, \\ \text{CNOT}_{DFS} &= \text{CNOT}_{1,3} \times \text{CNOT}_{1,4}, \end{aligned}$$

where $\text{CNOT}_{i,j}$ is a CNOT gate for which atom i is the control qubit and atom j the target qubit. The T_{DFS} gate is simply implemented in the same way as for the restricted gates.

In Fig. 4.6 we plot the performance of the unrestricted Hadamard and CNOT gates. As expected, these gates are much more sensitive to phase errors than the restricted gates.

Spontaneous emission from the Rydberg states also severely limits the fidelity for the unrestricted gates, as the controlled-phase gate involves resonant transitions to the Rydberg levels.

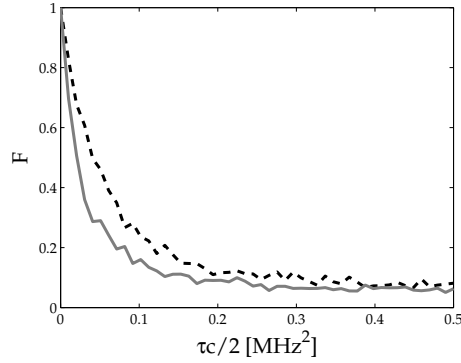


Figure 4.6. Performance for the unrestricted gates. The lines correspond to H_{DFS} (dashed) and $CNOT_{DFS}$ (solid). Parameters: $\Omega/2\pi = 0.5$ MHz, $\Delta_{rr} = 100$ MHz, $\tau = 1$ μ s, $\alpha_e = \alpha_r = 1.5$.

The durations of the gates are, however, smaller than for the restricted gates, which is not surprising since the latter are based on a fourth-order process. Thus, with the parameters for Fig. 4.6 the durations of the gates are 15.5 μ s for the Hadamard and 14 μ s for the CNOT gate.

An additional advantage of the unrestricted gates as opposed to the restricted ones we have suggested is that they are less sensitive to variations in Δ_{rr} and thus to atomic motion.

4.4 Summary

We have identified a set of logical-qubit basis states for a neutral-atom decoherence-free subspace and a corresponding universal set of gates which allow the system to remain in the subspace during computations and thus protect information from phase errors at all times.

Numerical simulations demonstrate that the proposed set of gates is much more robust against phase errors than a set of gates which are unrestricted in the sense that they allow the system to leave the decoherence-free subspace during computations. They are, however, also much more affected by the motion of the atoms in the traps. Therefore, one has to consider what the worst source of decoherence is for a given physical situation and subsequently choose which set of gates to use. Even if the set of restricted gates is assessed to be unfavorable, one should still consider using the logical-qubit basis states for computations as this encoding protects information during storage of the qubits.

As a final remark, we note that the fourth-order process used for the construction of a controlled phase gate between two atoms is in itself an interesting alternative to previous proposals for two-atom gates in that during

the process the Rydberg levels are not substantially populated. We elaborate on this perspective in our paper [III].

Error correction in ensemble registers

The issue of scalability is a major obstacle to the experimental realization of quantum computing. As of yet, demonstrations of small quantum algorithms have been carried out using less than 10 qubits. For instance, controlled entanglement of up to 8 trapped ions has been achieved [93, 94]. In addition, Shor's quantum factoring algorithm has been realized experimentally (to find the prime factors of the number 15) using 7 molecular spins [95].

For the NAQC proposal considered in this thesis, where bits are encoded in different atoms, scalability is in principle achievable in that the number of bits in the quantum register can be increased simply by adding more atoms to the system. In this case, scalability is not limited by any shortage of atoms in laboratory experiments, but by the immense difficulty of preserving and manipulating the quantum state of such a multi-component system.

However, as it was initially proposed in [63], by making use of an alternative encoding scheme some of the obstacles blocking the way to true scalability can be overcome. If information is encoded in the collective population of different internal atomic states, rather than storing individual bits in individual particles, single- and two-qubit gates can be implemented by collective internal state transitions, which renders the requirement of individual addressing superfluous.

For the proposal to be practically useful, however, errors must be correctable. In this chapter, based on our paper [V], we address the errors which may occur and devise methods to repair them. To simplify our error analysis, we first propose an encoding scheme which differs from the one proposed in [63], and which carries the additional advantage of simplifying single-qubit gates.

5.1 Ensemble register encoding

5.1.1 Conventional encoding

Most quantum computing proposals encode N bits of information in N two-level quantum systems, each consisting of the levels $|0\rangle$ and $|1\rangle$ (see Fig. 5.1).

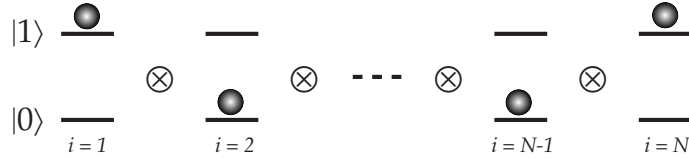


Figure 5.1. Conventional encoding of the N -bit state $|10\dots 01\rangle$ in N two-level systems. Bullets represent occupation numbers of single-particle states. Each two-level system encodes a qubit.

Thus, for NAQC individual qubits are stored in individual atoms. This conventional tensor product state encoding requires individual access to atoms and highly controlled interactions between them for gate implementation.

5.1.2 Collective encoding

In the collective encoding scheme proposed in [63], N qubits are stored in K atoms each of which has $N + 1$ long-lived internal states $|i\rangle$, where $i = 0, \dots, N$ (see Fig. 5.2). The $|0\rangle$ state is considered a reservoir state assumed to be initially occupied by all atoms.

Qubits are associated with the collective population of the different internal states of the particles in the ensemble. The potentially available Hilbert space is of dimension $(N + 1)^K$, but restricting the ensemble to symmetric states (where the symmetry consists in the wave function being invariant under the exchange of any two particle indices) with at most one atom populating each of the excited states, this reduces to 2^N , the dimension of an N -qubit register.

The N -bit logical register state $|a_1 a_2 \dots a_N\rangle$, where $a_i = 0, 1$, is associated with the symmetric state of the ensemble with a_i atoms populating the i th level. Thus, the logical two-qubit state $|01\rangle$ is an entangled state consisting of an equal superposition of all the states with no atoms in the single-particle state $|1\rangle$, one atom in $|2\rangle$, and all other atoms in $|0\rangle$.

5.1.3 An alternative collective encoding scheme

In the alternative encoding scheme which we propose, N qubits are stored in K atoms each of which has $2N + 1$ long-lived internal states denoted by $|s\rangle, |0_i\rangle, |1_i\rangle$, where $i = 1, \dots, N$ (see Fig. 5.3a). We assume that the system can be initially prepared in the reservoir product state $|S\rangle_K = |ss\dots s\rangle$ (the

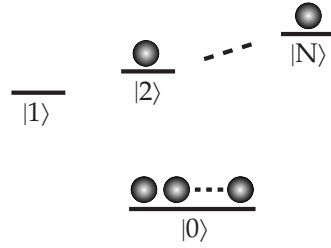


Figure 5.2. Collective encoding of the N -bit state $|01\dots 1\rangle$ in K multilevel atoms.

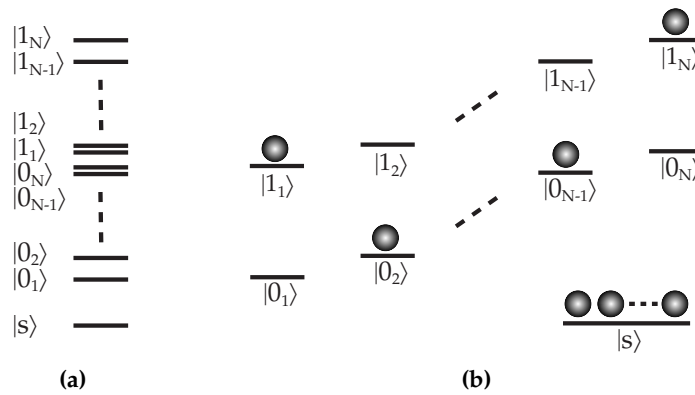


Figure 5.3. Collective encoding in our alternative scheme of N -bit states in K multilevel atoms. (a) An atom with $2N + 1$ internal states. $|s\rangle$ denotes the reservoir state. (b) Rearranging the levels in (a) depicts the encoding of $|10\dots 01\rangle$ in the symmetric states of the ensemble of atoms.

subscript indicates the number of atoms encoding the state), and that the atomic transitions $|0_i\rangle \leftrightarrow |1_i\rangle$ can be driven selectively.

By associating qubits with the collective population of the internal states of the particles, the potentially available Hilbert space is of dimension $(2N + 1)^K$, but by restricting the ensemble to symmetric states with at most one atom populating each of the excited states, this reduces to 2^N .

By way of example, the logical register state $|1_1 0_2 \dots 0_{N-1} 1_N\rangle$ is associated with the entangled state with unit population of the single-particle states $|1_1\rangle, |0_2\rangle, \dots, |0_{N-1}\rangle$, and $|1_N\rangle$, and zero population of all other states except for the reservoir state $|s\rangle$ (see Fig. 5.3b).

To be more specific, in the case of a one-bit register, the logical 0 state, denoted $|0\rangle_K$ (the subscript recalling the symmetric collective character and the number K of atoms contributing to the ensemble state), is encoded in the

following way:

$$|0\rangle_K = \frac{1}{\sqrt{K}}(|0ss\dots s\rangle + |s0s\dots s\rangle + \dots + |ss\dots s0\rangle). \quad (5.1)$$

In principle, only $K = N$ atoms are necessary to encode N qubits. However, as will be demonstrated later, larger ensemble sizes improve our error correction procedure.

5.1.4 Gates for collectively encoded qubits

Gates are performed by collectively addressing the atoms with light fields illuminating the entire ensemble. The Hamiltonians we apply must all leave the system in the symmetric Fock subspace corresponding to a single occupation of each manifold $\{|0_j\rangle, |1_j\rangle\}$, $j = 1, \dots, N$, at least until errors occur. Accordingly, in order for the collective encoding to work, the presence of an excitation blockade mechanism restricting the population of each internal state to either zero or unity is required. For neutral atoms the Rydberg blockade serves this purpose, while for molecules it can be achieved by coupling the ensemble to a Cooper pair box two-level system [96].

Taking advantage of the Rydberg blockade mechanism, an ensemble of atoms can be initialized to the $|0_1 0_2 \dots 0_N\rangle$ state by sequentially transferring unit population to $|0_j\rangle$ from the reservoir state. That is, a symmetric superposition of states with precisely one atom transferred to $|0_j\rangle$ from the initially macroscopically populated state $|s\rangle$ can be obtained by (i) applying to all atoms a π pulse resonant with the $|s\rangle \leftrightarrow |r\rangle$ transition, and (ii) applying to all atoms a π pulse resonant with the $|r\rangle \leftrightarrow |0_j\rangle$ transition. In the limit where the dipole-dipole interaction of the Rydberg states is much larger than the Rabi frequency, the Rydberg blockade prevents double occupancy of the Rydberg states (see chapter 3.5.2), which ensures that (i) leads to a symmetric superposition of states with precisely one atom occupying $|r\rangle$. Thus, the protocol has the following effect:

$$\begin{aligned} |ss\dots s\rangle &\xrightarrow{(i)} \frac{1}{\sqrt{K}}(|rs\dots s\rangle + |sr\dots s\rangle + \dots + |ss\dots r\rangle) \\ &\xrightarrow{(ii)} \frac{1}{\sqrt{K}}(|0_j s\dots s\rangle + |s0_j\dots s\rangle + \dots + |ss\dots 0_j\rangle). \end{aligned}$$

By performing the protocol above for j ranging from 1 to N , we finally obtain the state $|0_1 0_2 \dots 0_N\rangle$.

In our alternative collective encoding scheme, single-qubit rotations are carried out by driving the single-atom transitions $|0_j\rangle \leftrightarrow |1_j\rangle$. Although these rotations may in practice be driven via excited states (in a Raman process), it is potentially faster and easier to implement single-qubit gates than in [63], where single-qubit rotations are instead performed by (i) transferring

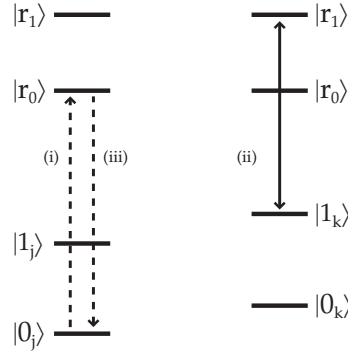


Figure 5.4. A conditional phase gate between qubits j and k is accomplished by (i) a π pulse transfer of the population in $|0_j\rangle$ to $|r_0\rangle$, (ii) a 2π pulse on the transition $|1_k\rangle \leftrightarrow |r_1\rangle$ (with $k \neq j$), and (iii) a π pulse transfer of the population in $|r_0\rangle$ to $|0_j\rangle$. After (i), initial population of $|0_j\rangle$ blocks further transfer of atoms to both $|r_0\rangle$ and $|r_1\rangle$, and the 2π pulse in (ii) yields a conditional phase. All states but $|10\rangle$ are endowed with a phase shift of π .

population from $|j\rangle$ to $|r\rangle$ by a π pulse, and (ii) coupling the states with zero and one atom in $|r\rangle$ for adjustable amounts of time, before (iii) mapping the $|r\rangle$ amplitude back onto $|j\rangle$ with a final π pulse [63].

Two-qubit gates rely on the Rydberg blockade. To this end, we assume the existence of two Rydberg states $|r_0\rangle$ and $|r_1\rangle$ which both block multiple Rydberg excitations. A π pulse, e.g. $|0_j\rangle \rightarrow |r_0\rangle$, is then used to conditionally prevent another qubit with $k \neq j$ from being excited into $|r_0\rangle$ and $|r_1\rangle$, as illustrated in Fig. 5.4. For the encoding scheme in [63], two-qubit gates are implemented through the same mechanism.

We emphasize that a great advantage in using the collective population of levels is that all operations are performed by collective access to the atoms, and the exciting laser pulses only need to be adjusted to the energies and coupling strengths of the atomic states. Hence, individual addressing is not required, as opposed to the case of conventional encoding. This means that all atoms can be trapped in a single site of an optical lattice.

5.1.5 Qubit encoding in the Zeeman sublevels

If the qubits are encoded in the internal Zeeman sublevels of the lower atomic hyperfine levels in alkali-metal atoms with ground hyperfine manifolds $\{F, F + 1\}$, a bias magnetic field along the z axis both makes the system immune to fluctuating orthogonal x and y components of the magnetic field and provides an energy splitting of the qubits states so that they can be unambiguously addressed by resonant laser fields [63].

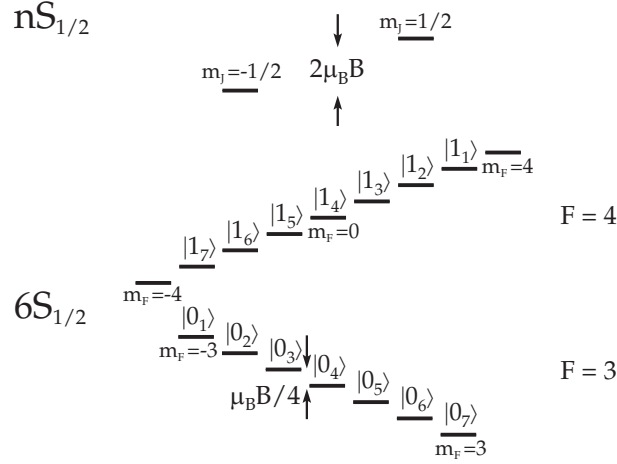


Figure 5.5. The 16 Zeeman ground states of cesium as well as the two fine structure states of a Rydberg level (used for Rydberg blockade). Seven qubits are encoded in the pair of states $|F = 3, m_F\rangle, |F = 4, -m_F\rangle$, where $m_F = 0, \pm 1, \pm 2, \pm 3$. Of the two remaining states $|F = 4, m_F = 4\rangle$ and $|F = 4, m_F = -4\rangle$, one state is available for the reservoir state and one state is not used, since the transitions $|6S_{1/2}, F = 4, m_F = 4\rangle \leftrightarrow |nS_{1/2}, m_J = 1/2\rangle$ and $|6S_{1/2}, F = 4, m_F = -4\rangle \leftrightarrow |nS_{1/2}, m_J = -1/2\rangle$ are degenerate. All other ground to Rydberg transitions are separated by at least $\mu_B B/4\hbar$. Thus, if this quantity is large compared to the two-photon Rabi frequency for transitions to the Rydberg levels, any ground state can be selectively excited. The figure is reproduced from [63] by courtesy of Klaus Mølmer.

Fluctuations of the z component of the field perturb the atomic levels, but in our alternative encoding scheme we can make the system immune to these fluctuations if qubits are associated with the pairs of states $\{|F, m_F\rangle, |F + 1, -m_F\rangle\}$, with $m_F = 0, \pm 1, \pm 2, \dots, \pm F$. The states $|F, m_F\rangle, |F + 1, -m_F\rangle$ experience the same linear Zeeman shift and only small differential quadratic shifts in the presence of magnetic field fluctuations, which therefore only slightly disturb the relative phase of qubit states 0 and 1. Hence, by this specific choice of qubit levels, an automatic decoherence-free subspace encoding is provided which is protected against fluctuations in the external magnetic field acting on all atoms. Experimentally, coherence times exceeding 1 s have been observed for superpositions of such states with $m_F = \pm 1$ in ^{87}Rb [97].

A specific example is provided by cesium. Having a nuclear spin of $I = 7/2$, cesium provides 16 stable Zeeman states in the $F = 3, 4$ hyperfine levels, as illustrated in Fig. 5.5. This allows for encoding of 7 qubits. Admittedly, this number is not impressive. However, considering instead holmium

with 128 hyperfine ground states (more than any other stable atom), collective encoding permits 60 qubits [79].

Additionally, the number of qubits can be increased by placing a small number of samples far enough apart to allow for individual addressing, while close enough to permit strong dipole-dipole interaction of the Rydberg states. In [79] a detailed study of this approach for holmium estimated a limit of 17 samples, yielding a total processor size of $60 \times 17 = 1020$ directly coupled qubits.

5.2 Error correction for collectively encoded qubits

For collective encoding to be practically useful, the errors which may occur must be addressed and methods to repair them devised. Because of interaction with their local environment (background gas collisions and spontaneous emission of radiation), it is physically motivated to assume that particles are affected by independent errors. In the conventional encoding scheme, where qubits are stored in separate particles, this assumption implies that qubits are corrupted independently of each other. Error correction schemes then consist of syndrome measurement and conditional back action, which corrects such errors if they are not too frequent [36].

However, in our collective encoding approach, this physical error model implies that the system may leave the symmetric, computational subspace. Accordingly, error correction techniques, derived under the assumption that errors occur independently on separate qubits, do not apply. But, as we discuss in the following, we have devised methods for efficient error identification and correction.

5.2.1 Atom loss

The first error source we shall consider is atom loss. For the sake of simplicity, we start with the case of a one-bit register prepared in the logical 0 state. Rewriting (5.1) leads to

$$|0\rangle_K = \frac{1}{\sqrt{K}} |0\rangle \otimes |S\rangle_{K-1} + \sqrt{\frac{K-1}{K}} |s\rangle \otimes |0\rangle_{K-1}. \quad (5.2)$$

All atoms are identical, but for simplicity we consider the removal of the first atom, which produces the state

$$|\psi\rangle = \frac{1}{\sqrt{K}} |S\rangle_{K-1} + \sqrt{\frac{K-1}{K}} |0\rangle_{K-1}, \quad (5.3)$$

or a mixed state with equivalent weight factors on the two components. For large K , this state is dominated by the second term, which encodes the

correct register state but with a smaller total number of atoms in the ensemble. Since gates act on this component in the same way as on the state encoded with the original number of atoms, the error due to the atomic loss is therefore only connected with the first component in (5.3), which will be propagated by the subsequent unitary dynamics and introduce a very small probability (i.e., the probability that the loss occurred multiplied by the factor $1/K$) for an erroneous output at the end of the calculation.

The same reasoning can be applied to any qubit superposition state yielding the same result, and a simple calculation shows that in an N -bit register, loss of a single atom introduces an erroneous component with population N/K . For very large K , we may accept the erroneous component in the wave function, or we may identify the error, by carrying out a measurement to find out if one of the subspaces $\{|0_i\rangle, |1_i\rangle\}$ is not populated. By transferring an atom from $|s\rangle$ to that subspace via the Rydberg state, we reestablish a legal, but most likely erroneous, register state. The error can, however, be addressed by suitable error correction techniques, which we shall outline below.

5.2.2 Disturbance of an atom

Atom loss is not the most critical error to affect the ensemble since the resulting state retains the full permutation symmetry, and the computation may go on safely. It is more problematic when an atom is disturbed and remains in the sample, where it continues to interact with the other atoms and corrupts the future quantum gates.

For the sake of simplicity, we examine the case of a single-bit register initially prepared in the single-qubit state,

$$\begin{aligned} \alpha |0\rangle_K + \beta |1\rangle_K &= \frac{1}{\sqrt{K}}(\alpha |0\rangle + \beta |1\rangle) \otimes |S\rangle_{K-1} \\ &+ \sqrt{\frac{K-1}{K}} |s\rangle \otimes (\alpha |0\rangle_{K-1} + \beta |1\rangle_{K-1}). \end{aligned} \quad (5.4)$$

If the first atom is affected by an error, the term in the first line has negligible amplitude compared to the term in the second line if K is large, and it will be neglected in the following. Suppose that the $|s\rangle$ state of the first atom evolves into

$$|\phi\rangle = c_0 |0\rangle + c_1 |1\rangle + c_s |s\rangle + |\phi'\rangle, \quad (5.5)$$

where $|\phi'\rangle$ is orthogonal to $|0\rangle, |1\rangle$, and $|s\rangle$. Accordingly, the resulting erroneous state of the ensemble is on the form

$$\begin{aligned} |\psi_{er}\rangle &= \sqrt{\frac{K-1}{K}} (c_s |s\rangle + |\phi'\rangle) \otimes (\alpha |0\rangle_{K-1} + \beta |1\rangle_{K-1}) \\ &+ \sqrt{\frac{K-1}{K}} (c_0 |0\rangle + c_1 |1\rangle) \otimes (\alpha |0\rangle_{K-1} + \beta |1\rangle_{K-1}). \end{aligned} \quad (5.6)$$

In the first line, the $|\phi'\rangle$ component will never interfere with the computation, and the single atom state $|s\rangle$ couples so weakly to our laser driving fields in comparison with the symmetric states of the remaining atoms that it will only slightly perturb the state of the ensemble.¹ However, the second line in (5.6) shows dangerous double occupancy of register states 0 and 1, which must be suppressed by physical manipulation of the system.

To this end, we apply the following procedure, which is illustrated in Fig. 5.6:

(i) First, we simultaneously apply two laser beams coupling $|0\rangle$ and $|1\rangle$ to two different Rydberg states $|r_0\rangle$ and $|r_1\rangle$ with the same Rabi frequency Ω . We assume that both Rydberg states $|r_0\rangle$ and $|r_1\rangle$ block multiple Rydberg excitations. As a consequence, the states $|x\rangle \otimes |y\rangle_{K-1}$, with $x = s, \phi'$ and $y = 0, 1$, couple to the states $|x\rangle \otimes |r_y\rangle_{K-1}$ with the same coupling strength $\hbar\Omega$, while the states with $x = 0, 1$ and $y = 0, 1$ couple to $(|r_x\rangle \otimes |y\rangle_{K-1} + |x\rangle \otimes |r_y\rangle_{K-1})/\sqrt{2}$ with the coupling strength $\sqrt{2}\hbar\Omega$. Thanks to the second coupling strength being larger by a factor of $\sqrt{2}$, it is possible to design a composite pulse sequence which leaves the first line in (5.6) (and also any non-erroneous state) unchanged, while transforming the second line into

$$\begin{aligned} & \sqrt{\frac{K-1}{2K}} [(c_0|r_0\rangle + c_1|r_1\rangle) \otimes (\alpha|0\rangle_{K-1} + \beta|1\rangle_{K-1}) \\ & + (c_0|0\rangle + c_1|1\rangle) \otimes (\alpha|r_0\rangle_{K-1} + \beta|r_1\rangle_{K-1})]. \end{aligned}$$

To this end, we have designed the composite pulse sequence $\pi_0 2\pi_{\phi'} \pi_0$, where $\phi' = \arccos(\cot^2(\sqrt{2}\pi))$. As usual, the notation θ_ϕ indicates a pulse area $\theta = \Omega t$ and a phase ϕ . As illustrated by Fig. 5.7, this sequence leaves states with coupling strength $\hbar\Omega$ unaffected while implementing σ_y (up to phase factors), σ_y being the Pauli y matrix, for states with coupling strength $\sqrt{2}\hbar\Omega$.

In the design of our composite pulse sequence, we have demanded that the first and the third pulse lead to evolutions of the Bloch vector along the same great circle. This is also the case for some of the simple composite pulses described in chapter 3.4.4. Observing that a sequence of three pulses with pulse areas π , 2π , and π , returns a two-level system with coupling strength $\hbar\Omega$ to the starting point irrespective of the phases, the construction of our sequence reduces to the problem of finding the angle ϕ' of the middle pulse which accomplishes the desired evolution for a two-level system with coupling strength $\sqrt{2}\hbar\Omega$. We note that the same ansatz can be used for some other coupling strengths. For instance the same overall evolution is

¹This robustness against perturbations on individual atoms is crucial for many uses of ensembles [98], and has been crucial in experiments, e.g., on continuous variable quantum storage in atomic ensembles, which already in their initial state may have a significant number of atoms that are not pumped into the symmetric state [99].

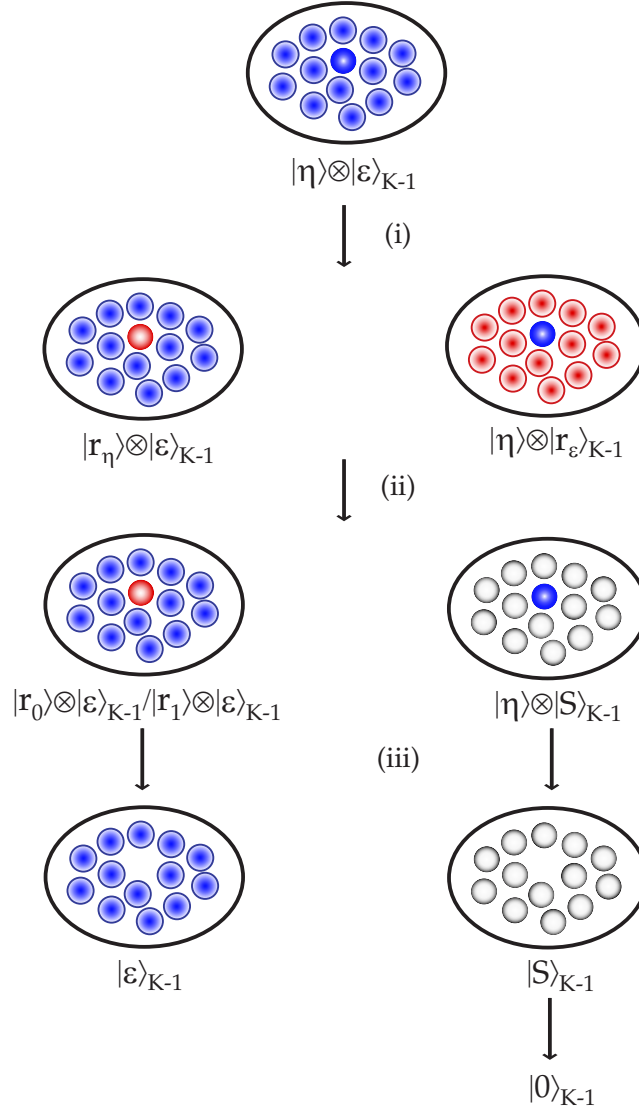


Figure 5.6. Schematic illustration of our procedure to remove single atom occupancy of register states which are already occupied by the ensemble. The second and the third line of the figure depict superposition states. We use the short hand notation $|\eta\rangle = c_0|0\rangle + c_1|1\rangle$, $|r_\eta\rangle = c_0|r_0\rangle + c_1|r_1\rangle$, $|\epsilon\rangle = \alpha|0\rangle_{K-1} + \beta|1\rangle_{K-1}$, and $|r_\epsilon\rangle = \alpha|r_0\rangle_{K-1} + \beta|r_1\rangle_{K-1}$. Our error detection sequence proceeds as follows: (i) $0 \leftrightarrow r_0$ and $1 \leftrightarrow r_1$ resonant composite pulses are applied. (ii) After detection of either $|r_0\rangle$ or $|r_1\rangle$, either an $s \leftrightarrow r_0$ or an $s \leftrightarrow r_1$ resonant pulse is applied. (iii) Depending on the result of the measurement in (ii), either $|r_0\rangle$ or $|r_1\rangle$ is ionized. If an ion signal is observed, the final state is $|\epsilon\rangle_{K-1}$. Otherwise, $|\eta\rangle$ is ionized yielding the state $|S\rangle_{K-1}$, which is subsequently transferred into the final state $|0\rangle_{K-1}$ by an $s \leftrightarrow 0$ resonant pulse.

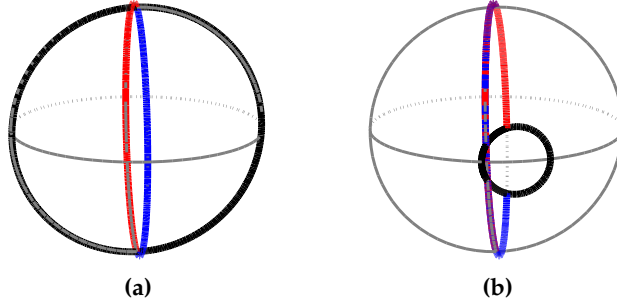


Figure 5.7. The evolution of $|0\rangle$ on the Bloch sphere during the pulse sequence π_0 (red), $2\pi_{\phi'}$ (black), π_0 (blue), where $\phi' = \arccos(\cot^2(\sqrt{2}\pi))$, for two-level systems with coupling strengths (a) $\hbar\Omega$ and (b) $\sqrt{2}\hbar\Omega$. The outcomes are rotations from $|0\rangle$ (south pole) to (a) $|0\rangle$ and (b) $|1\rangle$ (north pole). The axes are the same as in Fig. 3.4.

obtained if, for a coupling strength of $\sqrt{3}\hbar\Omega$, the phase of the second pulse is $\phi' = \arccos(\cot^2(\sqrt{3}\pi))$.

(ii) We can check if an error has occurred by measuring the Rydberg state content in the ensemble, e.g., by means of the blockade of a neighboring read-out ensemble [52]. Such a measurement is projective, and if a Rydberg excitation in $|r_0\rangle$ is detected, we get the unnormalized state

$$c_0 |r_0\rangle \otimes (\alpha |0\rangle_{K-1} + \beta |1\rangle_{K-1}) + \alpha(c_0 |0\rangle + c_1 |1\rangle) \otimes |r_0\rangle_{K-1}.$$

The goal is now to modify this state so that it can be used for further processing. Since the coupling of the symmetrically excited Rydberg state $|r_0\rangle_{K-1}$ to the reservoir state $|S\rangle_{K-1}$ is $\sqrt{K-1}$ times larger than the coupling of the single-atom states $|r_0\rangle$ and $|s\rangle$, a resonant π pulse on the $s \leftrightarrow r_0$ transition can be driven which makes a complete transfer of the collective state $|r_0\rangle$ into $|S\rangle$ and only a $\sim 1/K^{1/2}$ transfer of the single atom component $|r_0\rangle$ into $|s\rangle$. After such a pulse we therefore mainly obtain

$$c_0 |r_0\rangle \otimes (\alpha |0\rangle_{K-1} + \beta |1\rangle_{K-1}) + \alpha(c_0 |0\rangle + c_1 |1\rangle) \otimes |S\rangle_{K-1}.$$

By use of an appropriate composite pulse sequence, this erroneous amplitude transfer can be reduced. For this purpose, we propose to apply three consecutive π pulses with phases 0 , $2\pi/3$, and $4\pi/3$ instead of a single π pulse (see Fig. 5.8), which reduces the amplitude of the erroneous transfer of $|r_0\rangle/|r_1\rangle$ to $|s\rangle$ from $\sim 1/K^{1/2}$ to $\sim 1/K^{3/2}$.

(iii) Subsequently, we apply an ionizing pulse of the Rydberg state $|r_0\rangle$. If an ion is observed, we retain the correct initial qubit state $(\alpha |0\rangle_{K-1} + \beta |1\rangle_{K-1})$ with one atom less in the ensemble. If no ion is detected, we obtain

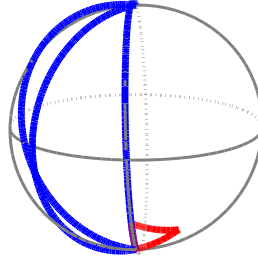


Figure 5.8. The evolution of $|0\rangle$ on the Bloch sphere during the pulse sequence $\pi_0 \pi_{2\pi/3} \pi_{4\pi/3}$ for coupling strengths $\hbar\Omega$ (blue) and $\hbar\Omega/\sqrt{K-1}$ (red). The outcomes are rotations from $|0\rangle$ to $|1\rangle$ and to $|0\rangle$, respectively.

$(c_0 |0\rangle + c_1 |1\rangle) \otimes |S\rangle_{K-1}$. Applying pulses ionizing the states $|0\rangle$ and $|1\rangle$ finally leads to $|S\rangle_{K-1}$. We complete the procedure by applying a resonant pulse $s \leftrightarrow 0$, so that $|S\rangle_{K-1}$ is transferred to $|0\rangle_{K-1}$.

If, during the first Rydberg state measurement, $|r_0\rangle$ is not observed, and if $|r_1\rangle$ is subsequently detected, one can apply similar procedures as above. If neither $|r_0\rangle$ nor $|r_1\rangle$ are detected, the system is projected onto a (sufficiently) non-erroneous component in (5.6) that the ensemble still reliably encodes the desired register state.

By applying the detection/correction procedure described above to a single-qubit register, we either obtain the correct initial state $(\alpha |0\rangle_{K-1} + \beta |1\rangle_{K-1})$ or end up in $|0\rangle_{K-1}$. It should be emphasized that as long as no error or a simple particle loss occur, no error signal is reported by the Rydberg populations, and no atoms are unnecessarily removed from the ensemble. In an N -bit register one merely has to check all the qubit populations successively as described above. At the end, we know whether and where an error has occurred.

If needed, we can repair the state of the erroneous qubit, provided we encode each bit of information in a superposition state $\alpha(|00\rangle_K + |11\rangle_K)/\sqrt{2} + \beta(|01\rangle_K + |10\rangle_K)/\sqrt{2}$, such that two ensemble qubits encode one logical qubit. Going through the above error identification and register restoration scheme, assuming an error has occurred in any of the two register positions, we either recover the same superposition, but with one atom less in the ensemble, or superpositions involving only the first or the second component of our logical qubit basis states, such as $\alpha|00\rangle_{K-1} + \beta|01\rangle_{K-1}$, from which the entire logical qubit basis states can be reconstructed by simple gate operations. This error-correction encoding is simpler than in the usual tensor product encoding because our error identification protocol provides direct information about which qubit has to be repaired.

If p denotes the error probability per atom per gate, the number of gates

n_g must fulfill $pn_g \lesssim 1$ to maintain the correct computational state component against single atom loss, and $(pK)^2n_g \lesssim 1$ to limit the number of simultaneous pairs of errors. A value of $p = 10^{-4}$ is thus compatible with the application of as much as 10^4 quantum gates on a few tens of qubits in an ensemble of around hundred atoms.

We anticipate that other schemes may be derived to correct for errors without ionization of the atoms, but the reduction in size of the symmetric ensemble due to errors seems unavoidable. However, in principle it is possible to transfer the quantum state of our diminished ensemble by the Rydberg blockade mechanism to a nearby independent ensemble of atoms, and such new ensembles can be supplied when needed.

5.3 Summary

We have proposed a novel scheme for encoding multiple bits of quantum information in symmetric collective states of an ensemble of multilevel atoms by making effective use of the single-particle Hilbert space dimension. A specific choice of qubit levels provides an automatic decoherence-free subspace encoding against fluctuations in the external magnetic field acting on all atoms.

Furthermore, we have derived a procedure for the correction of errors of individual atoms, which is successful if the ensemble is sufficiently large. We have designed composite pulse sequences crucial to the procedure, which facilitate operations that single pulses are incapable of accomplishing.

We presented the analysis for the special case of a global Rydberg blockade mechanism, but we anticipate that the scheme presented here for identifying and eliminating systems which have left the symmetric subspace may also apply to other effective interactions as a general restoration mechanism for symmetric states in ensembles of identical particles involved in quantum computing, long-term quantum memories, and in quantum repeaters.

In the next chapter, we shall demonstrate the application of collective encoding to the construction of few-qubit registers in small atomic ensembles suitable for atom-light interfaces in quantum repeaters.

Few qubit atom-light interfaces with collective encoding

So far we have outlined how a quantum processing unit based on neutral atoms may be implemented. However, an important aspect, which we have not touched upon yet, is how to achieve a scalable quantum network. In this chapter, we discuss the implementation of a single-photon source and its application for the construction of a quantum repeater.

Based on our paper [VIII], we suggest to employ small atomic ensembles for atom-light interfacing in a quantum repeater. Samples consisting of a few hundred atoms confined within regions of a few micrometer are large enough to provide efficient cooperative absorption and emission of light, and small enough to ensure strong dipole-dipole interactions when atoms are excited to their Rydberg states. We propose to build collectively encoded few-qubit quantum registers, which can store and transmit quantum information in the form of single photons. By making use of entanglement pumping protocols such registers constitute efficient atom-light interfaces in networks for scalable quantum computing and long distance quantum communication.

6.1 Superradiance

As was originally observed by Dicke [100], a collection of atoms exhibits cooperative spontaneous emission, such that light emitted from the sample, upon initial absorption of a single photon, displays an interference pattern. As a result the phenomena of superradiance (maximal enhancement) and subradiance (maximal suppression) emerge.

In [101] Scully et al. observed that a sample of randomly distributed atoms should re-emit an absorbed photon only in the forward direction (that is, in the same direction as the absorbed photon).

The superradiance phenomenon described above relies on the absorption of a single photon, such that only collective states with one excited atom are populated. However, employing single-photon sources is not necessary. Instead, the Rydberg blockade can be utilized to ensure that the employment of two classical fields to couple the ground state to a Rydberg state via an excited state $|e\rangle$, only leads to transitions to states with a single excited atom. By subsequently transferring the Rydberg population to $|e\rangle$, using a π pulse, spontaneous emission from $|e\rangle$ will be highly directional (because of phase matching) in the form of a single photon [102].

In the following, we present our research on light emitted from an ordered sample of neutral atoms. We will see that, by a proper design of the sample, we can achieve a highly directional single-photon source. In contrast to the discussion in [102], our results are based on a full, numerical treatment of the problem. This enables us to extract precise information about the spatio-temporal field mode coupled to our system.

6.2 Directionality of single-photon emission

Prior to embarking on a full, time-dependent description of the phenomenon of superradiance, we study in a more qualitative manner why a single photon emitted from a collection of atoms is highly directional.

Consider a collection of N atoms having an excited state $|e\rangle$ with an energy $\hbar\omega_0$ above the ground state $|g\rangle$. We assume that the system has absorbed a single photon of frequency $c\mathbf{k}_0$, such that the initial atom + field wave function is given by

$$|\Psi_0\rangle = \frac{1}{\sqrt{N}} \sum_{j=1}^N e^{i\mathbf{k}_0 \cdot \mathbf{r}_j} |e_j\rangle \otimes |0\rangle, \quad (6.1)$$

where $|e_j\rangle$ is the state for which atom j is excited and the other atoms are in the ground state. Such a state might be prepared using the method of [102], in which initialization of $|\Psi_0\rangle$ is performed by first driving the transition $|0\rangle \leftrightarrow |r\rangle$ using two classical fields with frequencies ω_1 and ω_2 , as defined in Fig. 6.1. The Rydberg blockade ensures that a collective state with a single Rydberg excitation is obtained. By subsequently applying a classical field with frequency ω_3 , resonant with the $|r\rangle \leftrightarrow |e\rangle$ transition, $|\Psi_0\rangle$ is obtained with $\mathbf{k}_0 = \mathbf{k}_1 + \mathbf{k}_2 - \mathbf{k}_3$.

By spontaneous emission $|\Psi_0\rangle$ evolves into a superposition of modes, each with all atoms returned to the ground state and a single photon with wavevector \mathbf{k} . The amplitude for emission with wavevector \mathbf{k} is proportional to

$$\langle g, 1_{\mathbf{k}} | (\mathbf{e}_{\mathbf{k}} \cdot \hat{\mathbf{d}}) a_{\mathbf{k}}^\dagger e^{-i\mathbf{k} \cdot \mathbf{r}} |\Psi_0\rangle = \frac{1}{\sqrt{N}} \sum_j^N \langle g | \mathbf{e}_{\mathbf{k}} \cdot \hat{\mathbf{d}} | e_j \rangle e^{i(\mathbf{k}_0 - \mathbf{k}) \cdot \mathbf{r}_j},$$

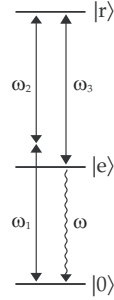


Figure 6.1. Three-level system for generation of a singly-excited collective state. The protocol is described in the text.

where $\mathbf{e}_{\mathbf{k}}$ and $a_{\mathbf{k}}^{\dagger}$ denote the polarization and the creation operator for a photon in mode \mathbf{k} , respectively. This implies that for an isotropic atomic matrix element, the probability of observing an emitted photon with wavevector \mathbf{k} is

$$P(\mathbf{k}) \propto \frac{1}{N} \left| \sum_j^N e^{i(\mathbf{k}_0 - \mathbf{k}) \cdot \mathbf{r}_j} \right|^2.$$

As noted in [102] this represents a highly directional emission because $P(\mathbf{k}) \propto N$ for $\mathbf{k} = \mathbf{k}_0$, whereas for all other directions it is strongly suppressed.

6.3 Time dependence of single-photon emission

The directionality of superradiance originates from phase matching, as demonstrated in the above discussion. However, in addition to the emission being highly directional, superradiance is also characterized by a higher emission rate compared to single-atom single-photon emission.

To study the time dependence of the emission, we provide a full, numerical treatment of the problem. Our method is inspired by the approach in [103], in which cooperative decay from a spherical sample of randomly distributed atoms upon single-photon absorption is studied analytically. For simplicity, effects of photon polarization are neglected, but these may readily be incorporated in a more detailed analysis.

As above, we consider a collection of N atoms initially prepared in Ψ_0 as given by (6.1). The system is subject to the Hamiltonian $H_0 + V$, where

$$H_0 = \sum_{j=1}^N \hbar\omega_0 |e_j\rangle \langle e_j| + \sum_{\mathbf{k}} \hbar c k a_{\mathbf{k}}^{\dagger} a_{\mathbf{k}},$$

$$V_I = \sum_{j=1}^N \sum_{\mathbf{k}} \hbar g_{\mathbf{k}} a_{\mathbf{k}}^{\dagger} |g\rangle \langle e_j| e^{-i\mathbf{k} \cdot \mathbf{r}_j} e^{i(c\mathbf{k} - \omega_0)t} + \text{h.c.},$$

and $g_{\mathbf{k}}$ is the atom-photon coupling constant. We remind the reader that $|e_j\rangle$ denotes the state for which atom j is excited and all other atoms are in the ground state.

The system evolves, by emission of the absorbed photon, into the state

$$|\Psi(t)\rangle = \sum_{j=1}^N \alpha_j e^{-i\omega_0 t} |e_j\rangle \otimes |0\rangle + \sum_{\mathbf{k}} \kappa_{\mathbf{k}} e^{-ickt} |g\rangle \otimes |\mathbf{k}\rangle, \quad (6.2)$$

where α_j , $\kappa_{\mathbf{k}}$ are time-dependent expansion coefficients in the interaction picture. From the Schrödinger equation we obtain

$$i\dot{\alpha}_j = \sum_{\mathbf{k}} g_{\mathbf{k}}^* e^{i\mathbf{k}\cdot\mathbf{r}_j} e^{-i(ck-\omega_0)t} \kappa_{\mathbf{k}}, \quad (6.3)$$

$$i\dot{\kappa}_{\mathbf{k}} = \sum_{j=1}^N g_{\mathbf{k}} e^{-i\mathbf{k}\cdot\mathbf{r}_j} e^{i(ck-\omega_0)t} \alpha_j. \quad (6.4)$$

Integrating (6.4) and substituting $\kappa_{\mathbf{k}}$ back into (6.3) gives

$$\dot{\alpha}_j = - \sum_{j=1}^N \sum_{\mathbf{k}} |g_{\mathbf{k}}|^2 e^{i\mathbf{k}\cdot(\mathbf{r}_j-\mathbf{r}_{j'})} \int_0^t e^{i(ck-\omega_0)(t'-t)} \alpha_{j'}(t') dt'. \quad (6.5)$$

Assuming that α_j varies on a time scale that is long compared to t ,¹ α_j can be taken outside the integral in (6.5) thus leading to

$$\dot{\alpha}_j = - \sum_{j'=1}^N \Gamma_{jj'}(t) \alpha_{j'},$$

where

$$\Gamma_{jj'} = \sum_{\mathbf{k}} |g_{\mathbf{k}}|^2 e^{i\mathbf{k}\cdot(\mathbf{r}_j-\mathbf{r}_{j'})} \left(\frac{\sin((ck-\omega_0)t)}{ck-\omega_0} + i \frac{\cos((ck-\omega_0)t) - 1}{ck-\omega_0} \right). \quad (6.6)$$

The second term in the parenthesis corresponds to a multi-atom ‘‘Lamb-shift’’, which is expected to be at least an order of magnitude smaller than the first term. Following [103], we apply the Wigner-Weisskopf approximation and discard the second term entirely. In that case, (6.6) reduces to

$$\Gamma_{jj'}(t) \approx \int \frac{d\Omega_{\mathbf{n}}}{4\pi} \pi(|g_{\mathbf{k}}|^2 \rho(ck)) |_{\mathbf{k}=\mathbf{n}k_0} e^{ik_0 \mathbf{n}\cdot(\mathbf{r}_j-\mathbf{r}_{j'})} \Theta(ct - |\mathbf{n}\cdot(\mathbf{r}_j-\mathbf{r}_{j'})|) \quad (6.7)$$

¹More precisely, we assume that $|g_{\mathbf{k}}|^2$ is roughly constant in a broad energy interval $\hbar\Delta$, where $\Delta^{-1} \ll t \ll \tau$. The parameter τ is the characteristic time scale for the variation of α_j , and is of order $1/N\gamma_1$, where γ_1 is the single-atom decay rate.

where we have chosen $t \gg \omega_0^{-1}$, and the following approximations have been employed: $\sin((\omega_0 - ck)t)/(\omega_0 - ck) \approx \pi\delta(\omega_0 - ck)$ and $\mathbf{k} \approx \mathbf{n}(k_0 + \delta k)$, where $\delta k \ll k_0$ and \mathbf{n} is the unit vector in the \mathbf{k} direction. The density of photon modes is $\rho(ck) = Vk^2/2\pi^2c$ and $\Theta(x)$ is the Heavyside step function. In the following, we assume that $|g_{\mathbf{k}}|$ is spherically symmetric.

If ct is much smaller than the mean interparticle distance, it follows from (6.7) that the decay matrix $\Gamma_{jj'}$ is diagonal with identical elements

$$\gamma_1 = \int \frac{d\Omega_{\mathbf{n}}}{4\pi} \pi |g_{\mathbf{k}}|^2 \rho(ck)|_{\mathbf{k}=\mathbf{n}k_0},$$

corresponding to the single-atom decay rate. We conclude that cooperativity is not initially present. However, this changes as t increases. When ct is much larger than the sample length, (6.7) reduces to

$$\Gamma_{jj'}(t) = \gamma_1 \frac{\sin(k_0|\mathbf{r}_j - \mathbf{r}_{j'}|)}{k_0|\mathbf{r}_j - \mathbf{r}_{j'}|},$$

and thus

$$\dot{\alpha}_j = -\gamma_1 \sum_{j'=1}^N \frac{\sin(k_0|\mathbf{r}_j - \mathbf{r}_{j'}|)}{k_0|\mathbf{r}_j - \mathbf{r}_{j'}|} \alpha_{j'}. \quad (6.8)$$

Introducing $\beta_j = e^{-ik_0\mathbf{r}_j} \alpha_j$ we obtain

$$\dot{\beta}_j = -\gamma_1 \sum_{j'=1}^N F(\mathbf{r}_j - \mathbf{r}_{j'}) \beta_{j'}, \quad (6.9)$$

where

$$F(\mathbf{r}_j - \mathbf{r}_{j'}) = \frac{\sin(k_0|\mathbf{r}_j - \mathbf{r}_{j'}|)}{k_0|\mathbf{r}_j - \mathbf{r}_{j'}|} e^{-ik_0\cdot(\mathbf{r}_j - \mathbf{r}_{j'})}.$$

In [103] the authors proceed by finding an approximate, analytic solution of (6.9) for the case of a spherical sample. For our purposes, we compute the numerical solution.

Equation (6.9) is solved formally by diagonalizing the F matrix. The vector β , whose j th element is β_j , is obtained at a given time from

$$\beta(t) = Ve^{-\Lambda t}V^{-1}\beta(t=0), \quad (6.10)$$

where Λ and V contain the eigenvalues and eigenvectors of F , respectively. Thus,

$$\beta_j = \sum_{j'} C_{jj'} e^{-\lambda_{j'} t},$$

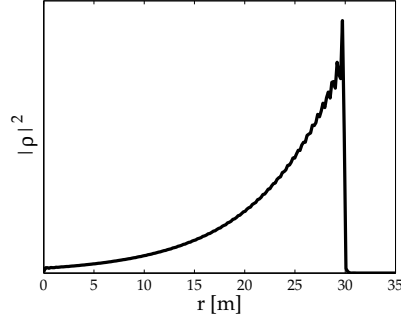


Figure 6.2. Density probability of a single photon emitted from a single atom after $0.1 \mu\text{s}$. Light is emitted uniformly in all directions. At this time, the light first emitted has traveled $ct = 30 \text{ m}$. Parameters are $k_0 = 2\pi/780 \text{ nm} = 8.1 \mu\text{m}^{-1}$ and $\gamma_1 = 19 \mu\text{s}^{-1}$.

where $C_{jj'} = v_j(j) \cdot \langle v_{j'} | \beta(t=0) \rangle$, λ_j denotes the j th eigenvalue, and v_j is the corresponding eigenvector. Note that from (6.1), it follows that $\beta(t=0)_j = 1/\sqrt{N}$. Finally, inserting (6.10) into (6.4) and integrating we find that

$$\kappa_{\mathbf{k}}(t) = ig_{\mathbf{k}} \sum_{jj'} C_{jj'} e^{i(\mathbf{k}_0 - \mathbf{k}) \cdot \mathbf{r}_j} \frac{1 - e^{(ic(k-k_0) - \lambda_{j'})t}}{ic(k-k_0) - \lambda_{j'}}. \quad (6.11)$$

Before we present the results of our simulations, we briefly review the findings of [103]. For a spherical sample of randomly distributed atoms, it was found that to observe superradiance the sample must be mesoscopic with a length equal to the sample size (in the incident photon direction) and a cross section on the order of the wavelength squared. The probability of photon emission first decreases as $\exp(-2\gamma_{col}t)$, where

$$\gamma_{col} = \frac{\gamma_1}{N} \sum_{j=1}^N \sum_{j'=1}^N F(\mathbf{r}_j - \mathbf{r}_{j'}) \quad (6.12)$$

is the collective decay rate of the fully symmetric, superradiant state. For $t \gg \gamma_{col}^{-1}$, photon reabsorption leads to an afterglow with a probability on the order of $(k_0 R_0)^{-2} \exp(-2\gamma_r t)$, where $\gamma_r = \gamma_1 N / 2k_0^4 R_0^4$ and R_0 is the radius of the spherical sample.

Single-photon emission from a single atom. As a special case, consider a sample consisting of only one atom. From (6.8), it follows that $\dot{\alpha} = -\gamma_1 \alpha$, which leads to the non-surprising result that $\alpha = \exp(-\gamma_1 t)$. Employing (6.4) with $g_{\mathbf{k}} = \sqrt{ck/2\hbar\epsilon_0 V} \langle 1 | \mathbf{e} \cdot \mathbf{r} | 0 \rangle$ gives

$$\kappa_k = ig_k \frac{1 - e^{(ic(k-k_0) - \gamma_1)t}}{ic(k - k_0) - \gamma_1}.$$

Thus, κ_k is independent of the orientation of \mathbf{k} and the photon is therefore emitted uniformly in all directions. Performing the Fourier transform of $\kappa_k e^{-ickt}$, cf. (6.2), we obtain the probability density of the emitted light as shown in Fig. 6.2.

6.4 Single-photon emission from a mesoscopic sample

For our numerical simulations we have studied a cubic lattice with an elongated sample of $7 \times 7 \times 20$ atoms (trapped in a three-dimensional optical lattice [49]), depicted in Fig. 6.3. With a lattice spacing of $0.37 \mu\text{m}$, the maximum distance between any two atoms is $8.3 \mu\text{m}$, which ensures atom-atom interactions strong enough for achieving Rydberg blockade.

We consider ^{87}Rb atoms. Selecting the excited state to be $5P_{1/2}$, with a spontaneous emission rate of $\gamma_1 = 19 \mu\text{s}^{-1}$, we obtain the total excited state population $\sum_j |\alpha_j|^2$ shown in Fig. 6.4 by solving (6.9). As the figure demonstrates, initially the excited state population evolves according to $\exp(-2\gamma_{col}t)$, where γ_{col} is given by (6.12). At first sight, γ_{col} might be expected to scale as N times γ_1 , cf. (6.12), but, for our sample γ_{col} is merely 5.7 times larger than the single-atom emission rate. Estimates for the effect of the finite size and the shape of the sample are discussed in [104]. For a macroscopic collection of atoms arranged in a circular cylinder of length $20\lambda/2$ and cross-sectional area $49(\lambda/2)^2$, a reduction of 100 is expected. Thus, we anticipate the collective emission rate to be of order $10\gamma_1$ rather than $980\gamma_1$. This result is confirmed by our numerical calculations.

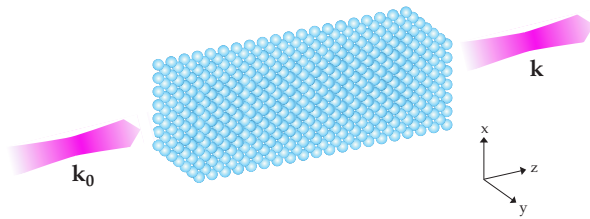


Figure 6.3. The sample considered in our numerical studies consists of $7 \times 7 \times 20$ ^{87}Rb atoms. To maximize the superradiance effect, \mathbf{k}_0 must be parallel to the long side of the sample. The emitted photon is primarily emitted in the direction of \mathbf{k}_0 . Parameters used for our simulations are $k_0 = 2\pi/780 \text{ nm} = 8.1 \mu\text{m}^{-1}$ and $k_0/k_l = 19/20$, giving a lattice spacing of $d = 0.37 \mu\text{m}$.

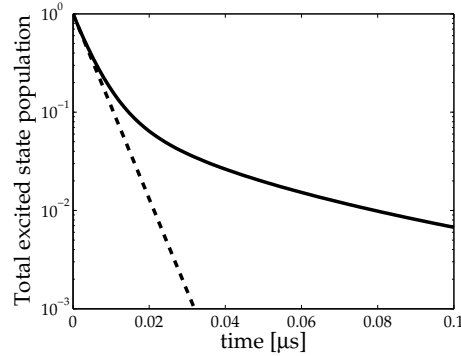


Figure 6.4. Total population of the excited state, that is $\sum_j |\alpha_j|^2$ (solid), for $7 \times 7 \times 20$ atoms. As appears from the figure (note the logarithmic scale), the population decreases as $\exp(-2\gamma_{col}t)$ (dashed) for $t < \gamma_{col}^{-1} = 1/(108 \mu\text{s}^{-1}) \approx 0.01 \mu\text{s}$. Assuming the excited state is $5P_{1/2}$, we have used $\gamma_1 = 19 \mu\text{s}^{-1}$. The initial spontaneous emission rate is thus 5.7 times larger for the sample than for a single atom.

At later times, the symmetry of the atomic excited state population in the sample is broken, explaining the longer survival of a few percent of collective excitation in the system. This process is illustrated in Fig. 6.5 in which the excited state population is displayed for the four top layers of the sample. Due to symmetry in the directions perpendicular to \mathbf{k}_0 , for instance the first and the last layers are identical. We see that even though the sample is uniformly excited initially, the excited state population falls off non-uniformly perpendicular to \mathbf{k}_0 . In particular, we note that the atoms away from the center retain excitation for a prolonged period of time, whereas atoms around the core decay much faster.

At a particular point in time, approximately given by γ_{col}^{-1} , photon reabsorption sets in and the decay rate decreases compared to γ_{col} . This process is illustrated in Fig. 6.6, which shows the explicit time dependence of the excited state population for selected atoms. We observe photon reabsorption for the atom with coordinates (4,4,10).

Phase matching in (6.11) ensures that in the superradiant state, the light emission occurs predominantly within a narrow emission cone. Thus, consider first Fig. 6.7, in which the photon probability density, obtained from a Fourier transform of $\kappa_{\mathbf{k}} e^{-i\mathbf{k}\cdot\mathbf{r}} e^{-i\omega t}$, is displayed for emission in the forward direction as well as directions with polar angles of $\pi/15$ and $\pi/12$, relative to the direction specified by \mathbf{k}_0 . As is apparent from the figure, the photon density falls off quickly with the polar angle. Also note that when compared to the case of a single-atom sample displayed in Fig. 6.2, the density is more peaked around ct in accordance with a larger emission rate.

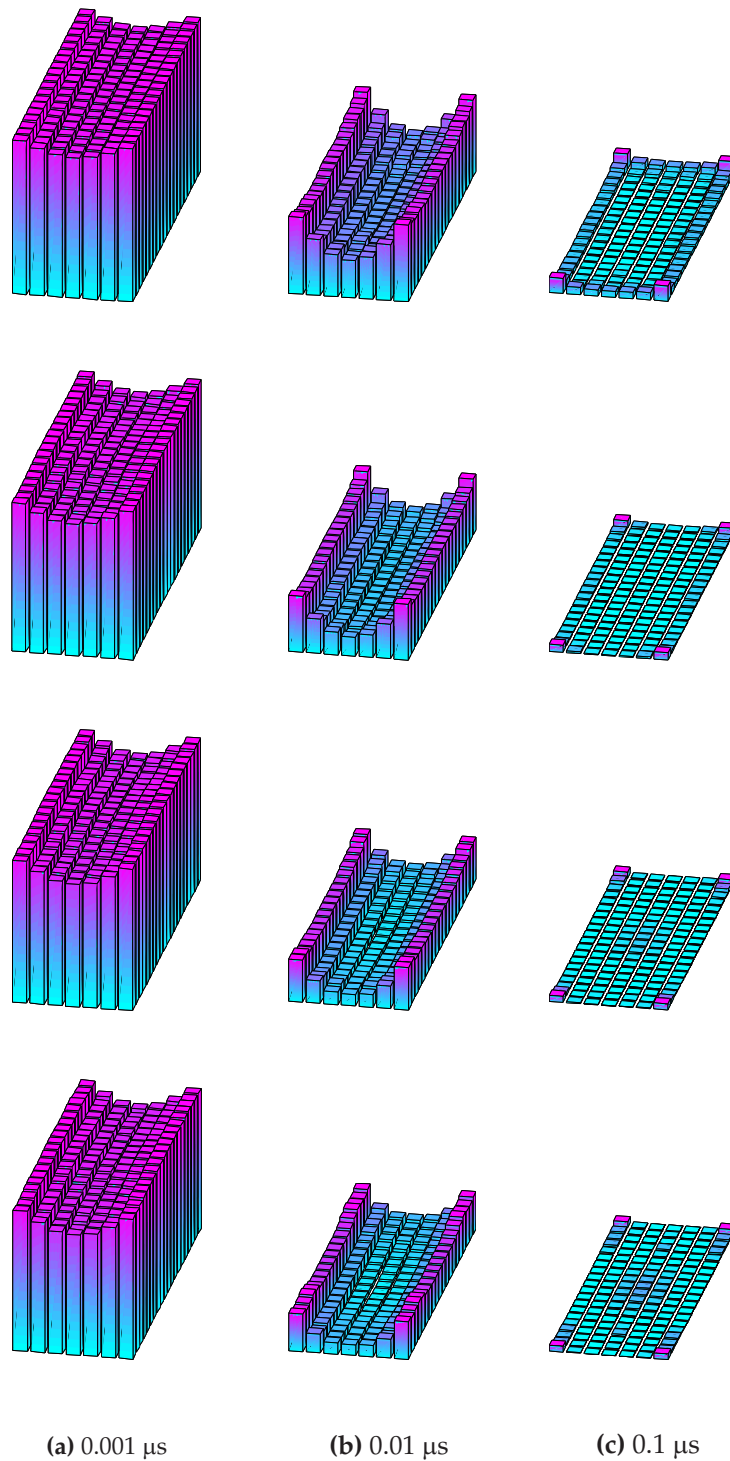


Figure 6.5. Excited state population in the four top layers of a $7 \times 7 \times 20$ sample at various times. Initially, the sample is uniformly excited such that $|\alpha|^2 = 1/N$ for all atoms. (a), (b) The excited state population decreases fastest around the center line until (c), at which point almost all atoms are in their ground states.

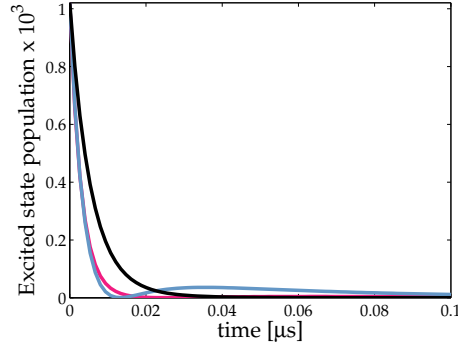


Figure 6.6. Excited state population for selected atoms. The coordinates of the atoms are stated as (n_x, n_y, n_z) , where n_j denotes the atom coordinate in the j th direction. The atom at $(1, 1, 1)$ is in the rearmost corner of the sample. The atoms considered are $(4, 4, 5)$ (pink), $(4, 4, 10)$ (turquoise), and $(1, 4, 10)$ (black).

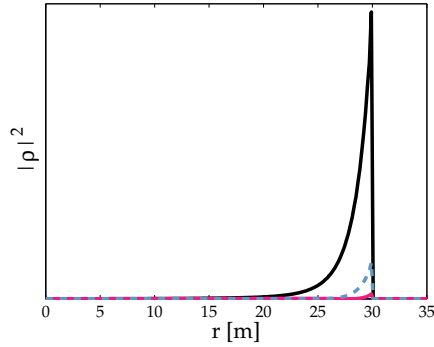


Figure 6.7. Probability density of the emitted photon after $0.1 \mu\text{s}$ in directions with polar angles relative to \mathbf{k}_0 of 0 (black), $\pi/15$ (turquoise) and $\pi/12$ (pink).

Figure 6.8 provides a study of the probability density build-up. The curves represent $P(\theta)$, i.e., the probability density integrated over k and the azimuthal angle ϕ , at various times.

From Fig. 6.9, we find that with more than 95% (90%) probability the photon is emitted in a direction within 0.3 (0.2) radians off the axis of the sample.

Our calculations demonstrate that a mesoscopic sample can provide sufficient superradiance to emit a single photon in a well-defined direction. However, one must consider whether this single-photon source is stable with respect to missing atoms in the sample. After all, the lattice may be imper-

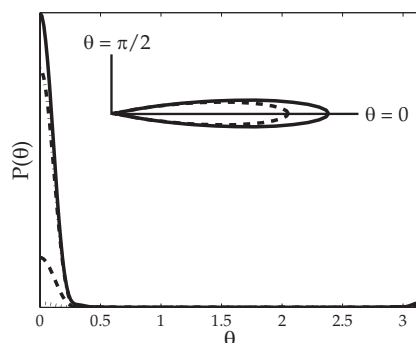


Figure 6.8. Integrated probability density $P(\theta)$ as a function of the polar angle θ , where $P(\theta) = \int_0^{2\pi} \int_{k_0 - \Delta_k/2}^{k_0 + \Delta_k/2} |\kappa(k, \theta, \phi)|^2 k^2 dk d\phi$ and $\Delta_k/k_0 = 3 \cdot 10^{-5}$. The photon density of light emitted in directions with polar angles infinitesimally close to θ is thus $P(\theta) \sin \theta d\theta$. The curves represent $P(\theta)$ after 10^{-10} s (dotted), 10^{-9} s (dashed), 10^{-9} s (dash-dotted), and 10^{-7} s (solid). The insert shows the directional density in a polar plot after 10^{-8} s (dashed) and 10^{-7} s (solid).

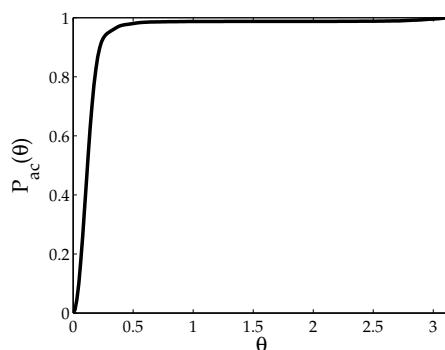


Figure 6.9. Integrated probability density $P_{ac}(\theta)$ as a function of the polar angle θ , where $P_{ac}(\theta) = \int_0^\theta P(\theta) \sin \theta d\theta / \int_0^{2\pi} P(\theta) \sin \theta d\theta$, after $1 \mu\text{s}$.

fectly loaded or atom loss may occur. If the loss of a few atoms causes a significant change in the field mode, unrealistic demands on the ability to trap atoms would have to be met. We have tested this concern by removing up to a few tens of atoms from random locations in our lattice system. We then computed the field mode emitted by the modified structure and determined the overlap of this field mode with the one emitted by the complete sample. These overlaps are very robust and in excess of 99% in all our simulations.

For our simulations we have chosen a simple, cubic lattice. However, other lattice structures could be explored to see whether the directionality of the emitted light could be optimized further. Elongating the sample improves our results. However, demanding that the Rydberg blockade mechanism must apply to any two atoms sets an upper limit to the size of the sample.

6.5 Atom-light interfaces for scalable quantum networks

Following the proposal for quantum repeaters based on a combination of stationary qubits in atomic ensembles and flying qubits in photons [21], significant progress has been obtained [105,106] on the entanglement of collective qubit degrees of freedom in physically separated atomic samples. These experiments involve large atomic gases, and while errors and imperfections may be detected and ‘repeat-until-successful’ strategies may be employed to secure the formation of entangled states [21,107], effective restoration of quantum information by error correction procedures is difficult to achieve in these systems.

The latter problem can be solved by interfacing light with a small quantum processor, allowing single- and two-qubit gates among its qubits. Although recent progress has been made on the free space coupling of a single atom to a focused single-photon field [108,109], light couples more strongly and with a larger degree of directional selectivity to an atomic ensemble. In the following, we discuss the application of our single-photon source for the construction of a quantum repeater.

6.5.1 Entanglement generation

For entanglement generation and communication between two distinct atomic samples, the fields emanating from two synchronously prepared samples can be mixed on a beam splitter. Entanglement of such samples is then heralded by the detector outcome [110]. Below we propose an architecture which provides a high success probability of this detection scheme due to the superradiant emission of light into preferred directions and a resulting good mode matching of the two field modes.

Alternatively, entanglement can be produced deterministically. Thus, as we have shown above, more than 95% of the light from our mesoscopic lattice is emitted within a well confined mode, and time reversal ensures that a field with a spatial dependence which is the complex conjugate of the fields found above will travel in the opposite direction and become extinct by the atomic excitation with a probability exceeding 95%. This offers the possibility of splitting a single photon by a beam splitter and direct it towards two separate ensembles in a deterministic protocol for entanglement generation.

In addition, if reshaping of single photon pulses between the mode emitted and its complex conjugate is possible, a photon wave packet generated in one sample can be absorbed with high fidelity in another sample in a high fidelity quantum information transfer protocol.

6.5.2 Entanglement purification

From our numerical analysis, we have found that a few hundred atoms within a $10\ \mu\text{m}$ wide volume in space have a high coupling fidelity (in excess of 95%) to a single photonic qubit. The dimensions of the sample ensure that the Rydberg blockade mechanism applies to any two atoms. Accordingly, qubits can be encoded collectively in the ensemble of atoms. We shall make use of this fact to obtain efficient entanglement purification.

The entanglement purification protocol suggested in [111] is an example of a nested entanglement pumping protocol [20, 112–114]. By involving auxiliary qubits, measurements and multiple rounds of communication, this protocol can raise a 90% transmission fidelity to arbitrarily high degrees of entanglement between two samples. We refer the reader to [111] for the algorithmic details of the protocol, and turn to the description of our physical implementation of local five-qubit registers needed for the protocol and of their coupling to light.

Figure 6.10a illustrates the five-qubit design proposed in [111]. Five separate physical systems take the role of a communication qubit c , three auxiliary qubits a_i , $i = 1, 2, 3$, for temporary storage and entanglement pumping, and a storage qubit s for the perfected state. In [111] proposed candidates for the five physical qubits are a chain of trapped ions with a single ion residing in an optical cavity, or ^{13}C atoms in the proximity of an optically addressable NV center in diamond.

Figure 6.10b illustrates our proposal for the implementation of the five-qubit register. Instead of identifying qubits with distinct physical systems, we propose to make use of the collective encoding scheme described in chapter 5.1.2, so that qubits are instead associated with the collective population of different internal (Zeeman) states.

In the generic single-atom level scheme in Fig. 6.10b, we identify a reservoir state $|0\rangle$ and five different long-lived internal states playing the same roles as the five physical qubits in Fig. 6.10a. The two Rydberg excited states are needed for initialization and single- and two-qubit operations.

The absorption of a single photon on the $|0\rangle \leftrightarrow |e\rangle$ transition, sketched in the figure, causes a collective excitation on the form (6.1). This must be quickly followed by a resonant transition between the excited state $|e\rangle$ and the long-lived communication state $|c\rangle$. The stationary communication qubit thus acquires the state of the incident traveling qubit with more than 95% probability. From here, the collective Rydberg gates (see chapter 5.1.4) between the communication qubit and the auxiliary and storage qubits are

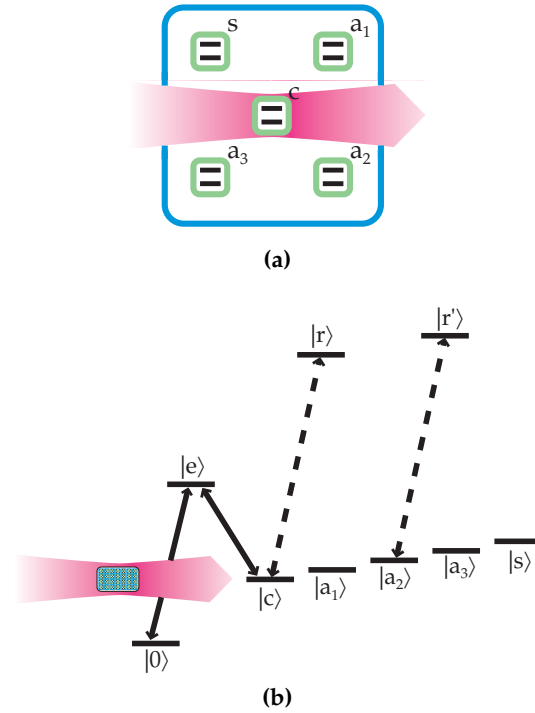


Figure 6.10. (a) A five-qubit register consisting of a communication qubit c , a storage qubit s and three auxiliary qubits $a_{1,2,3}$ [111]. (b) The collective encoding implementation, with a collective internal state transition interacting with the field mode, and long-lived and Rydberg internal states used for encoding and coupling of the five qubits.

used to implement the algorithm proposed in [111].

We note that a general quantum register state is a superposition of five-bit collective states $|a_1 a_2 \dots a_5\rangle$ with zero or unit collective occupancy of the atomic states c, a_1, a_2, a_3, s , and all optical transitions occur on every component of that superposition. The symmetric coupling to a given register state is enhanced by the square root of the number of atoms available for the transition. Since single-qubit gates are carried out using transitions to the reservoir level, the coupling parameter depends on the number of atoms in the register state. However, this number depends on the occupancy of all the qubit levels, and it may attain values ranging from $K - 5$ to K (corresponding to qubits being equal to unity and zero, respectively), where K is the number of atoms contributing to the ensemble state. Accordingly, the coupling parameters for the different collective states in the superposition differ. However, if the number of atoms encoding the collective states is large, the variations in the coupling parameters is small. In addition, the use

of composite pulses can ensure robustness against these small variations.

In the collective encoding scheme, all qubits may interchangeably take the roles of communication, auxiliary and storage qubits, unless polarization and dipole selection rules make it advantageous to fix these roles from the beginning. For instance, to ensure that the decay of the excited state during photon emission leads to population of the reservoir state rather than the qubit encoding states.

We have tested that our architecture is stable with respect to the loss of a few atoms from the sample. This also implies that the read out, needed in the entanglement pumping protocol, can be carried out by state selective ionization of qubit internal states, removing a single atom from the sample for each read out of a '1' result without affecting the symmetric state of the remaining atoms.

A concern is the gradual destruction of the symmetric collective state of the system due to the non-perfect matching with the superradiant mode. Entanglement pumping can correct some errors, but when the absorption fails, we do not only have a qubit error smaller than 5%: the system may actually leave the computational subspace of symmetric states. For a sufficiently large sample, the system is robust against such errors for a limited amount of time and the methods we derived in chapter 5 can be used to counter the errors.

In addition, we suggest to frequently restore the symmetry of the sample by optically pumping the communication qubit content into the reservoir state. Another way to obtain a renewable communication qubit in the sample may be to apply a more elaborate architecture with individually addressable ensembles within the Rydberg blockade radius of each other or with a mixture of two different species, contained within the same volume, and where the Rydberg blockade may also apply between species. One species, used for communication, may then be optically pumped at any time to maintain the symmetry of the system, needed for the interaction with the optical field.

6.6 Summary

We have suggested the use of small atomic ensembles for atom-light interfacing in a quantum repeater. Superradiant emission of light ensures that such atomic samples can be entangled efficiently either in a probabilistic or in a deterministic way.

We have proposed to use collective encoding for the entanglement pumping protocol presented in [111]. We emphasize that the collective encoding scheme both yields an efficient coupling to single photons and alleviates the need for addressing of individual atoms. This architecture offers a promising approach to interfaces of flying and stationary qubits and holds the potential to provide scalable quantum computing and long distance quantum communication.

Summary and outlook

At present, the road to the experimental realization of a quantum computer is still lined with obstacles, and it is an open question which of the proposals for the physical implementation of quantum computation will come to fruition.

A promising candidate is a quantum register based on neutral atoms, which has the advantage of being a well-controlled, isolated system with long qubit coherence times. The interactions required for two-qubit gates are less straightforward than for ions, but coupling qubits by exciting the atoms to their Rydberg states holds promise for fast gates. By a proper choice of Rydberg levels and spacing between atoms, it is possible to achieve a dipole-dipole interaction large enough to ensure that the presence of one Rydberg atom prevents the excitation of all other atoms nearby, a mechanism known as Rydberg blockade.

In this thesis, we have explored the use of Rydberg blockade for circumventing some of the limitations applying to neutral atom quantum computing (NAQC).

As presented in chapter 4, we have addressed the issue of decoherence by identifying a decoherence-free subspace immune to phase errors and demonstrating a universal set of gates which allow the system to remain in this subspace during gate operations, thus protecting information from phase errors at all times. Drawbacks of these gates include much longer gate times and increased sensitivity to atomic motion as compared to a set of gates which allow the system to leave the subspace during computations. In addition, spontaneous emission severely limits the fidelity. However, even if our set of gates is assessed to be unfavorable, it is advantageous for long-term storage to encode information in the decoherence-free subspace.

In chapters 5 and 6, we presented ideas for facilitating scalable NAQC. We have proposed a scheme for encoding information in the collective population of different internal states. This scheme has the great advantage over conventional tensor product encoding that it obviates the need for individual

addressing (which is a difficult requirement to meet). For the proposal to be practically useful, errors must be correctable. However, standard error correction techniques do not apply to this encoding scheme, and, accordingly, we have devised a procedure for efficient error identification and correction. Our proposal makes use of the Rydberg blockade mechanism, but other systems with mechanisms for excitation blockade may also be considered.

Based on the collective encoding scheme, we have proposed to build few-qubit quantum registers in small atomic ensembles. Superradiant emission of light enables these atomic ensembles to be entangled efficiently either in a probabilistic or in a deterministic way. By employing entanglement pumping protocols the registers can perform ideally in networks for scalable quantum computing and long distance quantum communication.

Finally, in chapter 2, we considered an issue not specific to NAQC, namely the fidelity of quantum operations. We have derived an expression for the fidelity distribution applicable to a normal linear state vector transformation in a two-dimensional Hilbert space. More importantly, we derived simple and compact expressions for the average fidelity of a general quantum operation and for the variance of the fidelity of a linear state vector map. This may have applications in quantum error correction, the capacity of quantum channels, and the way that, e.g., communication with quantum repeaters and entanglement distillation should optimally be carried out.

7.1 Dansk resumé

Kvantemekanikkens love, som regerer i den mikroskopiske verden, giver anledning til en række besynderlige fænomener. I 1980'erne opstod de første idéer om at udnytte nogle af kvantemekanikkens særeste egenskaber til at bygge en kvantecomputer, som bl.a. ved at regne på tal med flere samtidige værdier ville kunne løse meget svære matematiske problemer. Den store udfordring for fysikerne er at bygge et kvantemekanisk apparat, der kan bruges som computer. Et teoretisk forslag til en kvantecomputer, der gør brug af atomer, som er fanget i laserstråler, er blevet undersøgt, og metoder er blevet udviklet til robust håndtering af større datamængder og komplicerede beregninger.

Appendices

Evolution of the lambda system

To obtain the evolution operator for the lambda system, we take as our starting point (3.1). We proceed by applying the rotating wave approximation. This is performed by neglecting the fast oscillating terms in the Hamiltonian by noting that the operators

$$\sigma_{e0}^{Hs} = \sigma_{e0}^H e^{-i\omega_0 t} \quad \text{and} \quad \sigma_{e1}^{Hs} = \sigma_{e1}^H e^{-i\omega_1 t}$$

must be slowly varying. Note that σ_{e0}^H and σ_{e1}^H correspond to the operators σ_{e0} and σ_{e1} in the Heisenberg picture. This leads to the Hamiltonian

$$H = \hbar\omega_{10}\sigma_{11} + \hbar\omega_{e0}\sigma_{ee} - \frac{\hbar}{2}(\Omega_0 e^{-i\omega_0 t}\sigma_{e0} + \Omega_1 e^{-i\omega_1 t}\sigma_{e1} + \text{h.c.}),$$

where the Rabi frequencies are defined by

$$\Omega_j = \mathbf{d}_{ej} \cdot \mathbf{E}_{j,0} e^{i\mathbf{k}_j \cdot \mathbf{r}} / \hbar.$$

Switching to an appropriate rotating frame removes the explicit time dependence from the Hamiltonian. In general, transforming a state ket according to $|\psi\rangle \rightarrow |\tilde{\psi}\rangle = e^{i\tilde{\epsilon}t}|\psi\rangle$ corresponds to changing the Hamiltonian according to $H \rightarrow \tilde{H} = e^{i\tilde{\epsilon}t} H e^{-i\tilde{\epsilon}t} - \hbar\tilde{\epsilon}$, which follows immediately from the time-dependent Schrödinger equation. Using

$$\tilde{\epsilon} = \begin{pmatrix} -\frac{\Delta}{2} & 0 & 0 \\ 0 & \frac{\Delta}{2} + \omega_{10} & 0 \\ 0 & 0 & \omega_1 - \frac{\Delta}{2} \end{pmatrix},$$

where $\Delta_0 = \omega_0 - \omega_{e0}$, $\Delta_1 = \omega_1 - \omega_{e1}$, and $\Delta = \Delta_0 - \Delta_1$ are the single- and two-photon detunings, respectively, leads to the Hamiltonian in the rotating frame

$$\tilde{H} = \hbar \begin{pmatrix} \frac{\Delta}{2} & 0 & -\frac{\Omega_0^*}{2} \\ 0 & -\frac{\Delta}{2} & -\frac{\Omega_1^*}{2} \\ -\frac{\Omega_0}{2} & -\frac{\Omega_1}{2} & -\frac{\Delta_0 + \Delta_1}{2} \end{pmatrix}.$$

Setting $|\tilde{\psi}\rangle = \begin{pmatrix} \tilde{c}_0 \\ \tilde{c}_1 \\ \tilde{c}_e \end{pmatrix}$, and applying the Schrödinger equation, the following differential equations for the coefficients are obtained:

$$i\dot{\tilde{c}}_0 = \frac{\Delta}{2}\tilde{c}_0 - \frac{\Omega_0^*}{2}\tilde{c}_e, \quad (\text{A.1a})$$

$$i\dot{\tilde{c}}_1 = -\frac{\Delta}{2}\tilde{c}_1 - \frac{\Omega_1^*}{2}\tilde{c}_e, \quad (\text{A.1b})$$

$$i\dot{\tilde{c}}_e = -\frac{\Omega_0}{2}\tilde{c}_0 - \frac{\Omega_1}{2}\tilde{c}_1 - \frac{\Delta_0 + \Delta_1}{2}\tilde{c}_e. \quad (\text{A.1c})$$

If $|\Delta_0 + \Delta_1| \gg |\Omega_0|, |\Omega_1|, |\Delta|$, the coefficient \tilde{c}_e will be rapidly varying compared to the other coefficients. This permits the so-called adiabatic elimination, which in the literature consists of setting $\dot{\tilde{c}}_e = 0$. This is justified by the fact that \tilde{c}_e averages to zero over a small time interval. Another, perhaps more intuitive, way to perform the adiabatic elimination is to introduce a slowly varying coefficient defined by $\tilde{c}_e^s = \tilde{c}_e \exp[-i(\Delta_0 + \Delta_1)t/2]$ (see our paper [III] for a thorough exposition of the approximation). Inserting this into (A.1c) leads to an equation for \tilde{c}_e^s , which can be integrated readily using the approximation that the first two terms in (A.1c) are slowly varying compared to $\exp[-i(\Delta_0 + \Delta_1)t/2]$. Both approaches give the same result, namely that $\tilde{c}_e = -(\Omega_0\tilde{c}_0 + \Omega_1\tilde{c}_1)/(\Delta_0 + \Delta_1)$ which upon insertion into (A.1a) and (A.1b) yields the following effective Hamiltonian in the basis of $\{|\tilde{0}\rangle, |\tilde{1}\rangle\}$:

$$\tilde{H}_{eff} = \hbar \begin{pmatrix} \frac{\Delta}{2} + \frac{|\Omega_0|^2}{2(\Delta_0 + \Delta_1)} & \frac{\Omega_R^*}{2} \\ \frac{\Omega_R}{2} & -\frac{\Delta}{2} + \frac{|\Omega_1|^2}{2(\Delta_0 + \Delta_1)} \end{pmatrix},$$

where $\Omega_R = \Omega_0\Omega_1^*/(\Delta_0 + \Delta_1)$. Changing the zero point of the energy in this frame according to $|\tilde{\psi}\rangle = \exp[i(|\Omega_0|^2 + |\Omega_1|^2)t/4(\Delta_0 + \Delta_1)]|\tilde{\psi}\rangle$ leads to the Hamiltonian

$$\tilde{\tilde{H}}_{eff} = \hbar \begin{pmatrix} \frac{\Delta'}{2} & \frac{\Omega_R^*}{2} \\ \frac{\Omega_R}{2} & -\frac{\Delta'}{2} \end{pmatrix}, \quad (\text{A.2})$$

where $\Delta' = \Delta + (|\Omega_0|^2 - |\Omega_1|^2)/2(\Delta_0 + \Delta_1)$. Equation (A.2) can be written as a linear combination of Pauli matrices, i.e.,

$$\tilde{\tilde{H}}_{eff} = \frac{\hbar}{2}\mathbf{\Omega} \cdot \boldsymbol{\sigma},$$

where

$$\mathbf{\Omega} = \begin{pmatrix} \text{Re}(\Omega_R) \\ \text{Im}(\Omega_R) \\ \Delta' \end{pmatrix} \quad \text{and} \quad \boldsymbol{\sigma} = \sigma_x \hat{x} + \sigma_y \hat{y} + \sigma_z \hat{z},$$

with $\sigma_x, \sigma_y, \sigma_z$ being the three Pauli matrices. Note that $|\mathbf{\Omega}| = \sqrt{|\Omega_R|^2 + \Delta'^2}$. Since $(\boldsymbol{\sigma} \cdot \hat{\mathbf{n}})^2 = 1$, for any unit vector $\hat{\mathbf{n}}$, it follows that for constant Rabi

frequencies and detunings, the evolution matrix (found by exponentiating $-i\tilde{H}_{eff}t/\hbar$) is simply

$$\tilde{U} = \begin{pmatrix} \cos(\frac{|\Omega|t}{2}) - i\frac{\Delta'}{|\Omega|}\sin(\frac{|\Omega|t}{2}) & -i\frac{\Omega_R^*}{|\Omega|}\sin(\frac{|\Omega|t}{2}) \\ -i\frac{\Omega_R}{|\Omega|}\sin(\frac{|\Omega|t}{2}) & \cos(\frac{|\Omega|t}{2}) + i\frac{\Delta'}{|\Omega|}\sin(\frac{|\Omega|t}{2}) \end{pmatrix}.$$

One last transformation according to

$$|\tilde{\tilde{\psi}}\rangle = e^{-i\frac{|\Omega_0|^2+|\Omega_1|^2}{4(\Delta_0+\Delta_1)}t} \begin{pmatrix} e^{i\frac{\Delta}{2}t} & 0 \\ 0 & e^{-i\frac{\Delta}{2}t} \end{pmatrix} |\tilde{\psi}\rangle$$

leads to the evolution matrix

$$R(\theta, \phi) = \begin{pmatrix} e^{i\frac{\Delta}{2}t} [\cos(\frac{\theta}{2}) - i\frac{\Delta'}{|\Omega|}\sin(\frac{\theta}{2})] & -ie^{i\frac{\Delta}{2}t} \frac{|\Omega_R|}{|\Omega|} e^{-i\phi} \sin(\frac{\theta}{2}) \\ -ie^{-i\frac{\Delta}{2}t} \frac{|\Omega_R|}{|\Omega|} e^{i\phi} \sin(\frac{\theta}{2}) & e^{-i\frac{\Delta}{2}t} [\cos(\frac{\theta}{2}) + i\frac{\Delta'}{|\Omega|}\sin(\frac{\theta}{2})] \end{pmatrix},$$

where we have defined $\theta = |\Omega|t$ and $\Omega_R = |\Omega_R|e^{i\phi}$. A global phase factor of $\exp[-i(|\Omega_0|^2 + |\Omega_1|^2)t/4(\Delta_0 + \Delta_1)]$ is omitted. Summarizing the transformations it is clear that $R(\theta, \phi)$ is the evolution operator in the interaction picture because $|\tilde{\tilde{\psi}}\rangle = \begin{pmatrix} 1 & 0 \\ 0 & e^{i\omega_{10}t} \end{pmatrix} |\tilde{\psi}\rangle$.

APPENDIX B

The corrected Rabi frequency

In this appendix, we derive the formula (3.3) by taking into account the hyperfine structure of the excited level, i.e., the two excited levels shown in Fig. B.1.

The evolution matrix for this system is calculated using the methods employed in Appendix A. The dipole moment operator is now

$$\hat{\mathbf{d}} = \mathbf{d}_{e1,0}\sigma_{e1,0} + \mathbf{d}_{e1,1}\sigma_{e1,1} + \mathbf{d}_{e2,0}\sigma_{e2,0} + \mathbf{d}_{e2,1}\sigma_{e2,1} + \text{h.c.}$$

The dipole moments can be calculated, up to a common factor, using the following formulae [115]:

$$\begin{aligned} \langle \gamma J_1 J_2 J M | T_q^k | \gamma' J'_1 J'_2 J' M' \rangle &= \\ (-1)^{J-M} \left(\gamma J_1 J_2 J \| T^k \| \gamma' J'_1 J'_2 J' \right) \begin{pmatrix} J & k & J' \\ -M & q & M' \end{pmatrix}, \\ (\gamma J_1 J_2 J \| T^k \| \gamma' J'_1 J'_2 J') &= \\ (-1)^{J_1+J_2+J'+k} \left(\gamma J_1 \| T^k \| \gamma' J'_1 \right) \sqrt{(2J+1)(2J'+1)} \begin{Bmatrix} J_1 & J & J_2 \\ J' & J'_1 & k \end{Bmatrix}. \end{aligned} \quad (\text{B.1})$$

Setting $J_1 = J$, $J_2 = I$, $J = F$, and $M = M_F$, it is possible to relate the dipole moments to the reduced matrix element $(J \| T^k \| J')$. For σ_+ polarized light, $T_q^k = T_1^1 = e\sqrt{\frac{8\pi}{3}}rY_1^1$. As $J = J' = \frac{1}{2}$ and $I = \frac{3}{2}$, the dipole moments of interest are

$$\begin{aligned} d_{e1,0} &= \langle \frac{1}{2} \frac{3}{2} 1 1 \| T_1^1 \| \frac{1}{2} \frac{3}{2} 1 0 \rangle = \frac{1}{2\sqrt{6}} \left(\frac{1}{2} \| T_1 \| \frac{1}{2} \right), \\ d_{e2,0} &= \langle \frac{1}{2} \frac{3}{2} 2 1 \| T_1^1 \| \frac{1}{2} \frac{3}{2} 1 0 \rangle = \frac{1}{2\sqrt{2}} \left(\frac{1}{2} \| T_1 \| \frac{1}{2} \right), \\ d_{e1,1} &= \langle \frac{1}{2} \frac{3}{2} 1 1 \| T_1^1 \| \frac{1}{2} \frac{3}{2} 2 0 \rangle = -\frac{1}{2\sqrt{6}} \left(\frac{1}{2} \| T_1 \| \frac{1}{2} \right), \\ d_{e2,1} &= \langle \frac{1}{2} \frac{3}{2} 2 1 \| T_1^1 \| \frac{1}{2} \frac{3}{2} 2 0 \rangle = -\frac{1}{2\sqrt{2}} \left(\frac{1}{2} \| T_1 \| \frac{1}{2} \right), \end{aligned} \quad (\text{B.2})$$

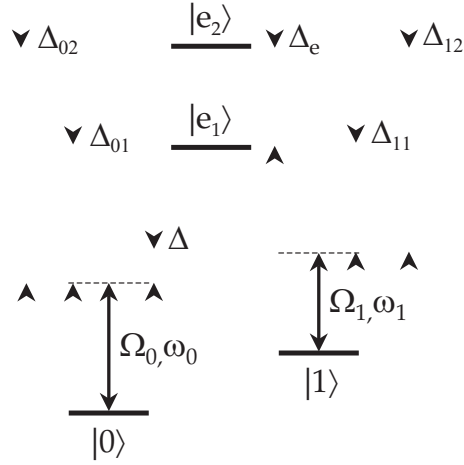


Figure B.1. The lambda system with the two hyperfine states of $5P_{1/2}$. The $F = 1$ and $F = 2$ states are denoted by $|e_1\rangle$ and $|e_2\rangle$, respectively. The detunings are defined by $\Delta_{01} = \omega_0 - \omega_{e1,0}$, $\Delta_{02} = \omega_0 - \omega_{e2,0}$, $\Delta_{11} = \omega_1 - \omega_{e1,1}$, $\Delta_{12} = \omega_1 - \omega_{e2,1}$, $\Delta_e = \omega_{e2,e1} = \Delta_{01} - \Delta_{02} = \Delta_{11} - \Delta_{12}$, and $\Delta = \omega_0 - \omega_1 - \omega_{10} = \Delta_{01} - \Delta_{11} = \Delta_{02} - \Delta_{12}$.

where the 3j- and the 6j-symbols in (B.1) are evaluated in [115]. As implied by (B.2), $|0\rangle$ and $|1\rangle$ only couple to the states $|e_1\rangle$ and $|e_2\rangle$ with $M_F = 1$. Defining $c_{i,j} = d_{i,j} / (\frac{1}{2} \|T_1\| \frac{1}{2})$, the following expression for Ω_R is obtained in the limit $|\Omega_0|, |\Omega_1|, |\Delta| \ll |\Delta_{01}|, |\Delta_{02}|, |\Delta_{11}|, |\Delta_{12}|$:

$$\Omega_R = \Omega_0 \Omega_1^* \left(\frac{c_{e1,0} c_{e1,1}}{\Delta_{01} + \Delta_{11}} + \frac{c_{e2,0} c_{e2,1}}{\Delta_{02} + \Delta_{12}} \right).$$

Equation (3.3) follows upon insertion of (B.2) in the limit $|\Delta| \ll |\Delta_e|$. The intensity of each Raman beam is $I = \frac{1}{2} c \epsilon_0 E_0^2$.

APPENDIX C

The Green's function perturbation method

In this appendix, we explain how the evolution operator (4.4) is obtained from the Green's function perturbation method described in [116, 117].

As our starting point we take the Hamiltonian for an atom subject to two laser fields, as shown in Fig. 4.2a. In the rotating wave approximation,

$$H_{atom} = \hbar\omega_{10}\sigma_{11} + \hbar\omega_{r0}\sigma_{rr} - \frac{\hbar}{2} \sum_{j=0}^1 (\Omega_j e^{-i\omega_j t} \sigma_{rj} + \text{h.c.}).$$

Therefore, including the Rydberg-Rydberg interaction the total Hamiltonian for two atoms subjected to the same two lasers reads

$$H = H_{atom} \otimes I + I \otimes H_{atom} + \hbar\Delta_{rr}\sigma_{rr} \otimes \sigma_{rr}.$$

Switching to the rotating frame defined by the vector transformation

$$|\psi\rangle \rightarrow |\tilde{\psi}\rangle = e^{i(I \otimes \epsilon + \epsilon \otimes I)t} |\psi\rangle,$$

where

$$\epsilon = \begin{pmatrix} 0 & 0 & 0 \\ 0 & \omega_0 - \omega_1 & 0 \\ 0 & 0 & \omega_0 \end{pmatrix},$$

leads to the following Hamiltonian in the basis $\{|00\rangle, |01\rangle, |0r\rangle, |10\rangle, |11\rangle$,

$|1r\rangle, |r0\rangle, |r1\rangle, |rr\rangle\}$:

$$\tilde{H} = \begin{pmatrix} 0 & 0 & -\frac{\Omega_0^*}{2} & 0 & 0 & 0 & -\frac{\Omega_0^*}{2} & 0 & 0 \\ 0 & -\Delta' & -\frac{\Omega_1^*}{2} & 0 & 0 & 0 & 0 & -\frac{\Omega_0^*}{2} & 0 \\ -\frac{\Omega_0}{2} & -\frac{\Omega_1}{2} & -\Delta & 0 & 0 & 0 & 0 & 0 & -\frac{\Omega_0^*}{2} \\ 0 & 0 & 0 & -\Delta' & 0 & -\frac{\Omega_0^*}{2} & -\frac{\Omega_1^*}{2} & 0 & 0 \\ 0 & 0 & 0 & 0 & -2\Delta' & -\frac{\Omega_1^*}{2} & 0 & -\frac{\Omega_1^*}{2} & 0 \\ 0 & 0 & 0 & -\frac{\Omega_0}{2} & -\frac{\Omega_1}{2} & -\Delta-\Delta' & 0 & 0 & -\frac{\Omega_1^*}{2} \\ -\frac{\Omega_0}{2} & 0 & 0 & -\frac{\Omega_1}{2} & 0 & 0 & -\Delta & 0 & -\frac{\Omega_0^*}{2} \\ 0 & -\frac{\Omega_0}{2} & 0 & 0 & -\frac{\Omega_1}{2} & 0 & 0 & -\Delta-\Delta' & -\frac{\Omega_1^*}{2} \\ 0 & 0 & -\frac{\Omega_0}{2} & 0 & 0 & -\frac{\Omega_1}{2} & -\frac{\Omega_0}{2} & -\frac{\Omega_1}{2} & -2\Delta+\Delta_{rr} \end{pmatrix}, \quad (\text{C.1})$$

where $\Delta = \omega_0 - \omega_{r0}$ and $\Delta' = \omega_0 - \omega_1 - \omega_{10}$.

In order to obtain the dynamics in the subspace $\{|00\rangle, |01\rangle, |10\rangle, |11\rangle\}$, we apply the Green's function method. The central idea of this approach is to identify an effective, approximate Hamiltonian from a Green's function projected onto the relevant subspace. Defining $H = H_0 + V$, the starting point is the choice of a relevant subspace \mathcal{E}_0 spanned by the ensemble of nearly resonant eigenvectors of H_0 in which we are interested. We define the orthogonal projectors $P = \sum |\psi_n\rangle\langle\psi_n|$ and $Q = I - P$ onto the subspaces \mathcal{E}_0 and \mathcal{E}_0^\perp , respectively. From the equation defining the Green's function,

$$G(z) = \frac{1}{z - H_0 - V'}$$

where $z = E \pm i\eta$, the following equation for the projection of $G(z)$ onto \mathcal{E}_0 is obtained:

$$PG(z)P = \frac{P}{z - PH_0P - PR(z)P'}, \quad (\text{C.2})$$

where

$$\begin{aligned} R(z) &= V + V \frac{Q}{z - QH_0Q - QVQ} V \\ &= V + V \frac{Q}{z - H_0} V + V \frac{Q}{z - H_0} V \frac{Q}{z - H_0} V + \dots \end{aligned}$$

The last equality follows from a perturbative expansion in powers of V . In (C.2), the term $PH_0P + PR(z)P$ could be interpreted as an effective Hamiltonian governing the dynamics of the states in \mathcal{E}_0 , but its dependence on z forbids us to consider it as a proper Hamiltonian. However, we can perform two approximations enabling us to identify an effective Hamiltonian for the states in \mathcal{E}_0 . First, it is possible to approximate $R(z)$ by a partial summation of the perturbation series. Secondly, the energy dependence of $R(z)$ can often be neglected and one may apply $R(E \pm i\eta) \approx R(E_0 \pm i\eta)$, where E_0 is the

energy around which the states in \mathcal{E}_0 are grouped. Finally, the approximate expression obtained for $PH_0P + PR(z)P$ can be identified with an effective Hamiltonian H_{eff} for the subensemble of states \mathcal{E}_0 .

Applying this method to find an effective Hamiltonian for the subspace $\{|00\rangle, |01\rangle, |10\rangle, |11\rangle\}$ is done in the following way. First we choose H_0 to be the diagonal matrix with elements corresponding to the diagonal of (C.1) and accordingly $V = \tilde{H} - H_0$. Secondly, we identify three subspaces of resonant states: $\{|00\rangle\}$, $\{|01\rangle, |10\rangle\}$ and $\{|11\rangle\}$. For each of the three subspaces we calculate the effective Hamiltonian to fourth order in V [116]:

$$H_{\mathcal{E}_0} = H^{(0)} + H^{(1)} + H^{(2)} + H^{(3)} + H^{(4)},$$

where

$$H^{(0)} = PH_0P,$$

$$H^{(1)} = PVP,$$

$$H^{(2)} = PVG_0VP,$$

$$H^{(3)} = PVG_0VG_0VP - PVG_0^2VP(H^{(0)} + H^{(1)}),$$

$$H^{(4)} = PVG_0VG_0VG_0VP - PVG_0^2VPVG_0VP - PVG_0^2VG_0VP(H^{(0)} + H^{(1)}) \\ - PVG_0VG_0^2VP(H^{(0)} + H^{(1)}) + PVG_0^3VP(H^{(0)} + H^{(1)})^2.$$

The operators P , E_0 , and G_0 all depend on the subspace \mathcal{E}_0 under consideration. In particular,

$$G_0 = \frac{Q}{E_0 - H_0} = \sum_{\phi_i \in \mathcal{E}_0^\perp} |\phi_i\rangle \langle \phi_i| \sum_j \frac{|\phi_j\rangle \langle \phi_j|}{E_0 - H_0(j, j)} \\ = \sum_{\phi_i \in \mathcal{E}_0^\perp} \frac{1}{E_0 - H_0(i, i)} |\phi_i\rangle \langle \phi_i|.$$

Finally, upon addition of the contributions from the three subspaces and a transformation to the interaction picture, we obtain an effective Hamiltonian H_{eff} governing the dynamics of the subspace $\{|00\rangle, |01\rangle, |10\rangle, |11\rangle\}$, which results in the evolution operator (4.4).

APPENDIX D

Quantum Monte Carlo approach

The Monte Carlo wave function approach was originally described in [35] (see [118] for a review). The underlying idea of the scheme is to replace the master equation for the density matrix by a wave function evolution including a stochastic element.

The starting point is the most general form of the master equation:

$$\dot{\rho}_S = -i\hbar [H_S, \rho_S] + \mathcal{L}(\rho_S), \quad (\text{D.1})$$

where the S subscript denotes operators for the system and \mathcal{L} is the Liouvillian

$$\mathcal{L}(\rho_S) = -\frac{1}{2} \sum_k \Gamma_k (c_k^\dagger c_k \rho_S + \rho_S c_k^\dagger c_k - 2c_k \rho_S c_k^\dagger).$$

Inserting $\rho_S = \sum_\alpha p_\alpha |\psi_\alpha\rangle\langle\psi_\alpha|$ into (D.1) gives

$$\dot{\rho}_S = \sum_\alpha p_\alpha \left(\frac{1}{i\hbar} (H_{eff} |\psi_\alpha\rangle\langle\psi_\alpha| - |\psi_\alpha\rangle\langle\psi_\alpha| H_{eff}^\dagger) + \sum_k \Gamma_k c_k |\psi_\alpha\rangle\langle\psi_\alpha| c_k^\dagger \right), \quad (\text{D.2})$$

where $H_{eff} = H - i\hbar \sum_k \Gamma_k c_k^\dagger c_k / 2$. Equation (D.2) suggests that H_{eff} can be interpreted as an effective Hamiltonian determining the evolution of the wave functions according to $i\hbar d|\psi_\alpha\rangle/dt = H_{eff} |\psi_\alpha\rangle$. The last term in (D.2) can be seen as a quantum jump operator which changes $|\psi_\alpha\rangle$ into the state $|\phi_{k,\alpha}\rangle = c_k |\psi_\alpha\rangle$, with some probability. Normalizing the states continually (as H_{eff} is not Hermitian) leads to the following master equation for discrete times:

$$\rho_S(t + \delta t) = \sum_\alpha p_\alpha \left((1 - \delta p_\alpha) |\tilde{\psi}_\alpha(t + \delta t)\rangle\langle\tilde{\psi}_\alpha(t + \delta t)| + \sum_k \delta p_{k,\alpha} |\tilde{\phi}_{k,\alpha}\rangle\langle\tilde{\phi}_{k,\alpha}| \right),$$

where the tilde denotes normalized states, $\delta p_{k,\alpha} = \delta t \Gamma_k \langle\psi_\alpha| c_k^\dagger c_k |\psi_\alpha\rangle$, and $\delta p_\alpha = \sum_k \delta p_{k,\alpha}$.

The Monte Carlo method proceeds by letting $|\tilde{\psi}_\alpha\rangle$ evolve according to H_{eff} with probability $(1 - \delta p_\alpha)$, and making the system jump into another state with probability δp_α (in particular into state $|\tilde{\phi}_{k,\alpha}\rangle$ with probability $\delta p_{k,\alpha}$). The advantage of this approach compared to solving the master equation is clear: only computation of the state vector elements (as opposed to the density matrix elements) is required. However, this approach does not calculate mean values in a deterministic way, but rather simulates the result obtained from solving the master equation. The evolution for a given initial state should thus be repeated a number of times in order to generate a distribution of outcomes. This of course involves an error, but on average the Monte Carlo simulation scheme reproduces the results of the master equation. The Monte Carlo approach raises many interesting fundamental questions (for instance about the effect of continuous monitoring on a system), but in what follows we shall apply the method to the system discussed in chapter 4.

Considering one atom, and assuming that spontaneous emission only occurs from the excited level $|e\rangle$ and the Rydberg level $|r\rangle$, it is further presumed that lost population does not end up in neither $|0\rangle$ nor $|1\rangle$ but in a reservoir level denoted by $|l\rangle$.¹ In this setting $c_e = |l\rangle\langle e|$ and $c_e^\dagger c_e = |e\rangle\langle e|$ and equivalently for $|r\rangle$. Consequently, the effective Hamiltonian is

$$H_{\text{eff}} = H_S - i\hbar\frac{\Gamma_e}{2}|e\rangle\langle e| - i\hbar\frac{\Gamma_r}{2}|r\rangle\langle r|.$$

When using the idea of a reservoir level it is not necessary to perform quantum jumps, as the fate of the population in the reservoir level is irrelevant. Accordingly, we take account of spontaneous emission by simply solving the Schrödinger equation in the same way as is done in the absence of spontaneous emission but with the additional term $-i\hbar\Gamma_e|e\rangle\langle e|/2 - i\hbar\Gamma_r|r\rangle\langle r|/2$ included in the single-atom Hamiltonians. However, one should be very cautious because $|l\rangle$ is not a part of the system and therefore H_{eff} is not norm preserving. In principle the states must be continuously renormalized such that $|\tilde{\psi}(t)\rangle = |\psi(t)\rangle / \|\psi(t)\|$. The fidelity will thus be given by $F = F(\tilde{\psi}) \cdot p(\tilde{\psi})$, where $F(\tilde{\psi}) = |\langle\psi_{\text{ideal}}|\tilde{\psi}\rangle|^2$ and $p(\tilde{\psi}) = \|\psi\|^2$ is the probability of remaining in the $|\tilde{\psi}\rangle$ state. But as $F = |\langle\psi_{\text{ideal}}|\tilde{\psi}\rangle|^2 \cdot \|\psi\|^2 = |\langle\psi_{\text{ideal}}|\psi\rangle|^2 = F(\psi)$ can be calculated simply from $|\psi\rangle$, it is clearly not necessary to renormalize states continuously. It is, however, interesting to determine $p(\tilde{\psi}) = \|\psi\|^2$ to check whether the largest fidelity error is ascribable to $F(\tilde{\psi})$ or $p(\tilde{\psi})$, since an error arising from $F(\tilde{\psi})$ is potentially correctable.

¹In reality, some of the population may end up in $|0\rangle$ or $|1\rangle$ without causing fidelity loss. However, when the reservoir level is introduced, population loss inevitably leads to a fidelity reduction; the fidelity we obtain is therefore a lower bound.

Bibliography

- [1] R. P. Feynman, *Quantum-Mechanical Computers*, Found. Phys. **16**, 507 (1986).
- [2] P. Benioff, *Quantum-Mechanical Hamiltonian Models of Turing-Machines*, J. Stat. Phys. **29**, 515 (1982).
- [3] L. K. Grover, *Quantum mechanics helps in searching for a needle in a haystack*, Phys. Rev. Lett. **79**, 325 (1997).
- [4] P. W. Shor, *Polynomial-time algorithms for prime factorization and discrete logarithms on a quantum computer*, SIAM J. Comput. **26**, 1484 (1997).
- [5] A. M. Steane, *Error correcting codes in quantum theory*, Phys. Rev. Lett. **77**, 793 (1996).
- [6] A. R. Calderbank and P. W. Shor, *Good quantum error-correcting codes exist*, Phys. Rev. A **54**, 1098 (1996).
- [7] M. A. Nielsen and I. L. Chuang, *Quantum Computation and Quantum Information* (Cambridge University Press, 2000).
- [8] D. Bruß and G. Leuchs, *Lectures on Quantum Information* (Wiley, 2007).
- [9] D. Deutsch and R. Jozsa, *Rapid Solution of Problems by Quantum Computation*, Proc. R. Soc. London, Ser. A **439**, 553 (1992).
- [10] J. I. Cirac and P. Zoller, *Quantum Computations with Cold Trapped Ions*, Phys. Rev. Lett. **74**, 4091 (1995).
- [11] H. J. Briegel, T. Calarco, D. Jaksch, J. I. Cirac and P. Zoller, *Quantum computing with neutral atoms*, J. Mod. Opt. **47**, 415 (2000).
- [12] I. H. Deutsch, G. K. Brennen and P. S. Jessen, *Quantum computing with neutral atoms in an optical lattice*, Fortschr. Phys. **48**, 925 (2000).
- [13] N. A. Gershenfeld and I. L. Chuang, *Bulk spin-resonance quantum computation*, Science **275**, 350 (1997).

- [14] L. M. K. Vandersypen and I. L. Chuang, *NMR techniques for quantum control and computation*, Rev. Mod. Phys. **76**, 1037 (2004).
- [15] P. Kok, W. J. Munro, K. Nemoto, T. C. Ralph, J. P. Dowling and G. J. Milburn, *Linear optical quantum computing with photonic qubits*, Rev. Mod. Phys. **79**, 135 (2007).
- [16] A. Imamoglu, *Quantum computation using quantum dot spins and microcavities*, Fortschr. Phys. **48**, 987 (2000).
- [17] Y. Makhlin, G. Schön and A. Shnirman, *Quantum-state engineering with Josephson-junction devices*, Rev. Mod. Phys. **73**, 357 (2001).
- [18] D. P. DiVincenzo, *The physical implementation of quantum computation*, Fortschr. Phys. **48**, 771 (2000).
- [19] R. Hughes and T. Heinrichs, *A Quantum Information Science and Technology Roadmap* (2004), [http : // qist.lanl.gov / qcomp_map.shtml](http://qist.lanl.gov/qcomp_map.shtml).
- [20] H. J. Briegel, W. Dür, J. I. Cirac and P. Zoller, *Quantum repeaters: The role of imperfect local operations in quantum communication*, Phys. Rev. Lett. **81**, 5932 (1998).
- [21] L. M. Duan, M. D. Lukin, J. I. Cirac and P. Zoller, *Long-distance quantum communication with atomic ensembles and linear optics*, Nature **414**, 413 (2001).
- [22] H. J. Kimble, *The quantum internet*, Nature **453**, 1023 (2008).
- [23] D. Jaksch, J. I. Cirac, P. Zoller, S. L. Rolston, R. Côté and M. D. Lukin, *Fast quantum gates for neutral atoms*, Phys. Rev. Lett. **85**, 2208 (2000).
- [24] M. D. Lukin, M. Fleischhauer, R. Cote, L. M. Duan, D. Jaksch, J. I. Cirac and P. Zoller, *Dipole Blockade and Quantum Information Processing in Mesoscopic Atomic Ensembles*, Phys. Rev. Lett. **87**, 037901 (2001).
- [25] M. Saffman and T. G. Walker, *Analysis of a quantum logic device based on dipole-dipole interactions of optically trapped Rydberg atoms*, Phys. Rev. A **72**, 022347 (2005).
- [26] M. Horodecki, P. Horodecki and R. Horodecki, *General teleportation channel, singlet fraction, and quasidistillation*, Phys. Rev. A **60**, 1888 (1999).
- [27] M. A. Nielsen, *A simple formula for the average gate fidelity of a quantum dynamical operation*, Phys. Lett. A **303**, 249 (2002).
- [28] M. D. Bowdrey, D. K. L. Oi, A. J. Short, K. Banaszek and J. A. Jones, *Fidelity of single qubit maps*, Phys. Lett. A **294**, 258 (2002).

-
- [29] E. Bagan, M. Baig and R. Muñoz Tapia, *Minimal measurements of the gate fidelity of a qudit map*, Phys. Rev. A **67**, 014303 (2003).
- [30] P. Zanardi and D. A. Lidar, *Purity and state fidelity of quantum channels*, Phys. Rev. A **70**, 012315 (2004).
- [31] C. Dankert, *Efficient simulation of random quantum states and operators*, Master thesis, University of Waterloo, arXiv:quant-ph/0512217 (2005).
- [32] A. Ambainis and J. Emerson, *Quantum t -designs: t -wise independence in the quantum world*, arXiv:quant-ph/0701126 (2007).
- [33] J. Emerson, R. Alicki and K. Życzkowski, *Scalable noise estimation with random unitary operators*, J. Opt. B **7**, S347 (2005).
- [34] H. Nakazato, Y. Hida, K. Yuasa, B. Militello, A. Napoli and A. Messina, *Solution of the Lindblad equation in the Kraus representation*, Phys. Rev. A **74**, 062113 (2006).
- [35] J. Dalibard, Y. Castin and K. Mølmer, *Wave-function approach to dissipative processes in quantum optics*, Phys. Rev. Lett. **68**, 580 (1992).
- [36] A. M. Steane, *Efficient fault-tolerant quantum computing*, Nature **399**, 124 (1999).
- [37] E. Knill, *Quantum computing with realistically noisy devices*, Nature **434**, 39 (2005).
- [38] J. von Neumann, *Distribution of the ratio of the mean square successive difference to the variance*, Ann. Math. Stat. **12**, 367 (1941).
- [39] J. Wesenberg and K. Mølmer, *Robust quantum gates and a bus architecture for quantum computing with rare-earth-ion-doped crystals*, Phys. Rev. A **68**, 012320 (2003).
- [40] I. Roos and K. Mølmer, *Quantum computing with an inhomogeneously broadened ensemble of ions: Suppression of errors from detuning variations by specially adapted pulses and coherent population trapping*, Phys. Rev. A **69**, 022321 (2004).
- [41] M. E. Muller, *A Note on a Method for Generating Points Uniformly on N -Dimensional Spheres*, Comm. Assoc. Comput. Mach. **2**, 19 (1959).
- [42] P. Zanardi and M. Rasetti, *Noiseless Quantum Codes*, Phys. Rev. Lett. **79**, 3306 (1997).
- [43] D. A. Lidar, I. L. Chuang and K. B. Whaley, *Decoherence-Free Subspaces for Quantum Computation*, Phys. Rev. Lett. **81**, 2594 (1998).

-
- [44] L. Viola, E. Knill and S. Lloyd, *Dynamical Decoupling of Open Quantum Systems*, Phys. Rev. Lett. **82**, 2417 (1999).
- [45] E. M. Fortunato, M. A. Pravia, N. Boulant, G. Teklemariam, T. F. Havel and D. G. Cory, *Design of strongly modulating pulses to implement precise effective Hamiltonians for quantum information processing*, J. Chem. Phys. **116**, 7599 (2002).
- [46] H. Ocampo, S. Paycha and A. Reyes, editors, *Geometric Methods for Quantum Field Theory* (World Scientific, 2001).
- [47] D. Jaksch, H. J. Briegel, J. I. Cirac, C. W. Gardiner and P. Zoller, *Entanglement of atoms via cold controlled collisions*, Phys. Rev. Lett. **82**, 1975 (1999).
- [48] J. M. Raimond, M. Brune and S. Haroche, *Colloquium: Manipulating quantum entanglement with atoms and photons in a cavity*, Rev. Mod. Phys. **73**, 565 (2001).
- [49] R. Grimm, M. Weidemüller and Y. B. Ovchinnikov, *Optical dipole traps for neutral atoms*, Adv. At. Mol. Opt. Phys. **42**, 95 (2000).
- [50] B. P. Masterson, C. Tanner, H. Patrick and C. E. Wieman, *High-Brightness, High-Purity Spin-Polarized Cesium Beam*, Phys. Rev. A **47**, 2139 (1993).
- [51] D. J. Wineland, J. C. Bergquist, W. M. Itano and R. E. Drullinger, *Double-Resonance and Optical-Pumping Experiments on Electromagnetically Confined, Laser-Cooled Ions*, Opt. Lett. **5**, 245 (1980).
- [52] M. Saffman and T. G. Walker, *Entangling single- and N-atom qubits for fast quantum state detection and transmission*, Phys. Rev. A **72**, 042302 (2005).
- [53] M. H. Levitt, *Composite Pulses*, Prog. Nucl. Magn. Reson. Spectrosc. **18**, 61 (1986).
- [54] H. K. Cummins, G. Llewellyn and J. A. Jones, *Tackling systematic errors in quantum logic gates with composite rotations*, Phys. Rev. A **67**, 042308 (2003).
- [55] S. Wimperis, *Broad-Band, Narrow-Band, and Passband Composite Pulses for Use in Advanced Nmr Experiments*, J. Magn. Reson. A **109**, 221 (1994).
- [56] M. S. Silver, R. I. Joseph and D. I. Hoult, *Selective Spin Inversion in Nuclear Magnetic-Resonance and Coherent Optics through an Exact Solution of the Bloch-Riccati Equation*, Phys. Rev. A **31**, 2753 (1985).
- [57] M. Saffman, private communication.

- [58] M. Cozzini, T. Calarco, A. Recati and P. Zoller, *Fast Rydberg gates without dipole blockade via quantum control*, *Opt. Commun.* **264**, 375 (2006).
- [59] T. F. Gallagher, *Rydberg atoms* (University Press, 1994).
- [60] T. G. Walker and M. Saffman, *Zeros of Rydberg-Rydberg Förster interactions*, *J. Phys. B* **38**, S309 (2005).
- [61] I. E. Protsenko, G. Reymond, N. Schlosser and P. Grangier, *Operation of a quantum phase gate using neutral atoms in microscopic dipole traps*, *Phys. Rev. A* **65**, 052301 (2002).
- [62] T. G. Walker and M. Saffman, *Consequences of Zeeman degeneracy for the van der Waals blockade between Rydberg atoms*, *Phys. Rev. A* **77**, 032723 (2008).
- [63] E. Brion, K. Mølmer and M. Saffman, *Quantum computing with collective ensembles of multilevel systems*, *Phys. Rev. Lett.* **99**, 260501 (2007).
- [64] I. Ryabtsev, D. B. Tretyakov and I. Beterov, *Applicability of Rydberg atoms to quantum computers*, *J. Phys. B* **38**, S421 (2005).
- [65] J. H. Wesenberg, *Quantum Information Processing in Rare-Earth-Ion Doped Crystals*, PhD thesis, University of Aarhus (2004).
- [66] A. Browayes, J. Beugnon, C. Tuchendler, H. Marion, A. Gaëtan, Y. Miroshnychenko, Y. R. P. Sortais, A. M. Lance, M. P. A. Jones, G. Messin and P. Grangier, *Recent progress on the manipulation of single atoms in optical tweezers for quantum computing*, arXiv:0708.3295 (2007).
- [67] N. Schlosser, G. Reymond and P. Grangier, *Collisional Blockade in Microscopic Optical Dipole Traps*, *Phys. Rev. Lett.* **89**, 023005 (2002).
- [68] M. P. A. Jones, J. Beugnon, A. Gaëtan, J. Zhang, G. Messin, A. Browaeys and P. Grangier, *Fast quantum state control of a single trapped neutral atom*, *Phys. Rev. A* **75**, 040301 (2007).
- [69] E. Urban, T. A. Johnson, T. Henage, L. Isenhower, D. D. Yavuz, T. G. Walker and M. Saffman, *Observation of Rydberg blockade between two atoms*, arXiv:0805.0758 (2008).
- [70] D. D. Yavuz, P. B. Kulatunga, E. Urban, T. A. Johnson, N. Proite, T. Henage, T. G. Walker and M. Saffman, *Fast ground state manipulation of neutral atoms in microscopic optical traps*, *Phys. Rev. Lett.* **96**, 063001 (2006).
- [71] T. A. Johnson, E. Urban, T. Henage, L. Isenhower, D. D. Yavuz, T. G. Walker and M. Saffman, *Rabi oscillations between ground and rydberg states with dipole-dipole atomic interactions*, *Phys. Rev. Lett.* **100**, 113003 (2008).

- [72] D. Tong, S. M. Farooqi, J. Stanojevic, S. Krishnan, Y. P. Zhang, R. Côté, E. E. Eyler and P. L. Gould, *Local blockade of Rydberg excitation in an ultracold gas*, Phys. Rev. Lett. **93**, 063001 (2004).
- [73] K. Singer, M. Reetz-Lamour, T. Amthor, L. G. Marcassa and M. Weidemüller, *Suppression of Excitation and Spectral Broadening Induced by Interactions in a Cold Gas of Rydberg Atoms*, Phys. Rev. Lett. **93**, 163001 (2004).
- [74] T. C. Liebisch, A. Reinhard, P. R. Berman and G. Raithel, *Atom counting statistics in ensembles of interacting Rydberg atoms*, Phys. Rev. Lett. **95**, 253002 (2005).
- [75] T. C. Liebisch, A. Reinhard, P. R. Berman and G. Raithel, *Erratum: Atom counting statistics in ensembles of interacting Rydberg atoms [Phys. Rev. Lett. 95, 253002 (2005)]*, Phys. Rev. Lett. **98**, 109903 (2007).
- [76] T. Vogt, M. Viteau, J. M. Zhao, A. Chotia, D. Comparat and P. Pillet, *Dipole blockade at Förster resonances in high resolution laser excitation of Rydberg states of cesium atoms*, Phys. Rev. Lett. **97**, 083003 (2006).
- [77] P. Bohlouli-Zanjani, J. A. Petrus and J. D. D. Martin, *Enhancement of Rydberg atom interactions using ac Stark shifts*, Phys. Rev. Lett. **98**, 203005 (2007).
- [78] R. Heidemann, U. Raitzsch, V. Bendkowsky, B. Butscher, R. Löw, L. Santos and T. Pfau, *Evidence for coherent collective Rydberg excitation in the strong blockade regime*, Phys. Rev. Lett. **99**, 163601 (2007).
- [79] M. Saffman and K. Mølmer, *Scaling the neutral atom Rydberg gate quantum computer by collective encoding in Holmium atoms*, arXiv:0805.0440 (2008).
- [80] G. M. Palma, K.-A. Suominen and A. K. Ekert, *Quantum computers and dissipation*, Proc. R. Soc. London, Ser. A **452**, 567 (1996).
- [81] L. M. Duan and G. C. Guo, *Preserving coherence in quantum computation by pairing quantum bits*, Phys. Rev. Lett. **79**, 1953 (1997).
- [82] D. A. Lidar, D. Bacon, J. Kempe and K. B. Whaley, *Decoherence-free subspaces for multiple-qubit errors. I. Characterization*, Phys. Rev. A **63**, 022306 (2001).
- [83] A. Shabani and D. A. Lidar, *Theory of initialization-free decoherence-free subspaces and subsystems*, Phys. Rev. A **72**, 042303 (2005).
- [84] P. G. Kwiat, A. J. Berglund, J. B. Altepeter and A. G. White, *Experimental verification of decoherence-free subspaces*, Science **290**, 498 (2000).

- [85] D. Kielpinski, V. Meyer, M. A. Rowe, C. A. Sackett, W. M. Itano, C. Monroe and D. J. Wineland, *A decoherence-free quantum memory using trapped ions*, *Science* **291**, 1013 (2001).
- [86] P. Xue and Y. F. Xiao, *Universal quantum computation in decoherence-free subspace with neutral atoms*, *Phys. Rev. Lett.* **97**, 140501 (2006).
- [87] J. E. Ollerenshaw, D. A. Lidar and L. E. Kay, *Magnetic resonance realization of decoherence-free quantum computation*, *Phys. Rev. Lett.* **91**, 217904 (2003).
- [88] D. Bacon, J. Kempe, D. A. Lidar and K. B. Whaley, *Universal fault-tolerant quantum computation on decoherence-free subspaces*, *Phys. Rev. Lett.* **85**, 1758 (2000).
- [89] J. Kempe, D. Bacon, D. A. Lidar and K. B. Whaley, *Theory of decoherence-free fault-tolerant universal quantum computation*, *Phys. Rev. A* **63**, 042307 (2001).
- [90] D. A. Lidar, D. Bacon, J. Kempe and K. B. Whaley, *Decoherence-free subspaces for multiple-qubit errors. II. Universal, fault-tolerant quantum computation*, *Phys. Rev. A* **63**, 022307 (2001).
- [91] L. Viola and E. Knill, *Robust dynamical decoupling of quantum systems with bounded controls*, *Phys. Rev. Lett.* **90**, 037901 (2003).
- [92] D. T. Gillespie, *The mathematics of Brownian motion and Johnson noise*, *Am. J. Phys.* **64**, 225 (1996).
- [93] D. Leibfried, E. Knill, S. Seidelin, J. Britton, R. B. Blakestad, J. Chiaverini, D. B. Hume, W. M. Itano, J. D. Jost, C. Langer, R. Ozeri, R. Reichle and D. J. Wineland, *Creation of a six-atom 'Schrödinger cat' state*, *Nature* **438**, 639 (2005).
- [94] H. Häffner, W. Hänsel, C. F. Roos, J. Benhelm, D. Chek-al kar, M. Chwalla, T. Körber, U. D. Rapol, M. Riebe, P. O. Schmidt, C. Becher, O. Gühne, W. Dür and R. Blatt, *Scalable multiparticle entanglement of trapped ions*, *Nature* **438**, 643 (2005).
- [95] L. M. K. Vandersypen, M. Steffen, G. Breyta, C. S. Yannoni, M. H. Sherwood and I. L. Chuang, *Experimental realization of Shor's quantum factoring algorithm using nuclear magnetic resonance*, *Nature* **414**, 883 (2001).
- [96] K. Tordrup and K. Mølmer, *Quantum computing with a single molecular ensemble and a Cooper-pair box*, *Phys. Rev. A* **77** (2008).
- [97] P. Treutlein, P. Hommelhoff, T. Steinmetz, T. W. Hänsch and J. Reichel, *Coherence in microchip traps*, *Phys. Rev. Lett.* **92** (2004).

- [98] C. Mewes and M. Fleischhauer, *Decoherence in collective quantum memories for photons*, Phys. Rev. A **72** (2005).
- [99] B. Julsgaard, J. Sherson, J. I. Cirac, J. Fiurasek and E. S. Polzik, *Experimental demonstration of quantum memory for light*, Nature **432**, 482 (2004).
- [100] R. H. Dicke, *Coherence in Spontaneous Radiation Processes*, Phys. Rev. **93**, 99 (1954).
- [101] M. O. Scully, E. S. Fry, C. H. R. Ooi and K. Wódkiewicz, *Directed spontaneous emission from an extended ensemble of N atoms: Timing is everything*, Phys. Rev. Lett. **96**, 010501 (2006).
- [102] M. Saffman and T. G. Walker, *Creating single-atom and single-photon sources from entangled atomic ensembles*, Phys. Rev. A **66**, 065403 (2002).
- [103] I. E. Mazets and G. Kurizki, *Multiatom cooperative emission following single-photon absorption: Dicke-state dynamics*, J. Phys. B **40**, F105 (2007).
- [104] L. Allen and J. H. Eberly, *Optical resonance and two-level atoms* (Dover Publications, 1987).
- [105] C. W. Chou, J. Laurat, H. Deng, K. S. Choi, H. de Riedmatten, D. Felinto and H. J. Kimble, *Functional quantum nodes for entanglement distribution over scalable quantum networks*, Science **316**, 1316 (2007).
- [106] T. Chaneliere, D. N. Matsukevich, S. D. Jenkins, S. Y. Lan, R. Zhao, T. A. B. Kennedy and A. Kuzmich, *Quantum interference of electromagnetic fields from remote quantum memories*, Phys. Rev. Lett. **98** (2007).
- [107] S. Chen, Y. A. Chen, B. Zhao, Z. S. Yuan, J. Schmiedmayer and J. W. Pan, *Demonstration of a stable atom-photon entanglement source for quantum repeaters*, Phys. Rev. Lett. **99** (2007).
- [108] N. Lindlein, R. Maiwald, H. Konermann, M. Sondermann, U. Peschel and G. Leuchs, *A new 4π geometry optimized for focusing on an atom with a dipole-like radiation pattern*, Laser Physics **17**, 927 (2007).
- [109] M. K. Tey, Z. Chen, S. A. Aljunid, B. Chng, F. Huber, G. Maslennikov and C. Kurtsiefer, *Strong interaction between light and a single trapped atom without a cavity*, arXiv:0802.3005 (2008).
- [110] D. N. Matsukevich, P. Maunz, D. L. Moehring, S. Olmschenk and C. Monroe, *Bell inequality violation with two remote atomic qubits*, Phys. Rev. Lett. **100** (2008).

-
- [111] L. Jiang, J. M. Taylor, A. S. Sørensen and M. D. Lukin, *Distributed quantum computation based on small quantum registers*, Phys. Rev. A **76**, 062323 (2007).
- [112] W. Dür, H. J. Briegel, J. I. Cirac and P. Zoller, *Quantum repeaters based on entanglement purification*, Phys. Rev. A **59**, 169 (1999).
- [113] L. Childress, J. M. Taylor, A. S. Sørensen and M. D. Lukin, *Fault-tolerant quantum repeaters with minimal physical resources and implementations based on single-photon emitters*, Phys. Rev. A **72**, 052330 (2005).
- [114] W. Dür and H. J. Briegel, *Entanglement purification for quantum computation*, Phys. Rev. Lett. **90** (2003).
- [115] I. I. Sobelman, *Atomic Spectra and Radiative Transitions* (Springer-Verlag, 1992).
- [116] F. H. M. Faisal, *Theory of Multiphoton Processes* (Plenum Press, 1987).
- [117] C. Cohen-Tannoudji, J. Dupont-Roc and G. Grynberg, *Atom-Photon Interactions* (Wiley, 1998).
- [118] K. Mølmer and Y. Castin, *Monte Carlo wavefunctions in quantum optics*, Quantum Semiclass. Opt. **8**, 49 (1996).